

# A Numerical Analysis of a Hydrogen Fueled Trapped Vortex Combustor for RQL Applications

using Large-Eddy Simulations

Bram Amant

# A Numerical Analysis of a Hydrogen Fueled Trapped Vortex Combustor for RQL Applications

## using Large-Eddy Simulations

by

Bram Amant

to obtain the degree of Master of Science at the Delft University of Technology,  
to be defended publicly on Friday March 21, 2025 at 09:00 AM.

Student number: 4672291  
Project duration: September 15, 2023 – March 21, 2025  
Thesis committee: Prof. dr. ir. S. Hickel TU Delft, Chair  
Dr. I. Langella, TU Delft, Supervisor  
Prof. dr. ir. S. Klein, TU Delft, External Examiner  
Dr. L. Mazzei, Ergon Research, Supervisor

An electronic version of this thesis is available at <http://repository.tudelft.nl/>.

# Preface

More than a year ago, I became deeply intrigued by combustion and the complex interplay of flow and flame dynamics. This fascination led me to pursue my MSc thesis in this field. Now, with this report and accompanied presentation, this research project has reached its conclusion. It has been a very intense, challenging, and immensely rewarding learning experience. Moreover, this moment also marks the end of my time as a student. Therefore, I would like to take this opportunity to express my gratitude to everyone who has supported me throughout the complete journey:

I would like to sincerely thank my daily supervisors, Ivan Langella and Lorenzo Mazzei for their constant support and guidance throughout the thesis project. Despite their demanding schedules, they were always available to discuss results, address challenges, and provide valuable insights. Their expertise in numerical simulations and combustion has been invaluable, significantly helping me progress in my research. Moreover, I am especially grateful for their patience and understanding, particularly during the more challenging moments of this project.

I would like to thank Thomas, my housemate for most of my student life, for the countless memorable moments we shared during that time. I am also very grateful to some of my closest friends: Léon, Tycho, Bram, Wouter, and Evert, who have been with me from the very beginning of the journey. A special thanks goes to my friends from Brakbrussel - Evert, Thomas, Léon, Stijn, Elliott, and Emile - for the many (un)forgettable days and nights in Delft. Many thanks as well to Niels, Kirsten, Aurelie for their incredible friendship and support. Finally, a deep appreciation for Oscar, Kato, Evert, Niels for all the thesis sessions in Echo. Thank you all for those amazing years!

*Bram Amant  
Delft, March 2025*

# Abstract

Within the context of hydrogen combustion, the trapped vortex combustor (TVC) combined with a Rich-Quench-Lean (RQL) combustion strategy holds great promise for achieving ultra-low emissions and advancing sustainable combustion technologies. However, ensuring thorough and sufficient fuel-air mixing before the completion of the chemical reactions, currently remain a critical challenge. This study focused on addressing this problem by exploring hydrogen's injection temperature as the potential solution. Therefore, a combination of 1D simulations and Large-Eddy simulations were conducted. Subsequently, the role of this temperature modification on the chemical reactivity was evaluated and the overall impact on the RQL effectiveness was assessed. The results indicated that lowering hydrogen injection temperature from 300 K to 150 K reduced chemical reactivity by 15% to 25%. However, this reduction was insufficient to significantly suppress or alter the combustion mode within the cavity. Nevertheless, the overall temperature reduction within the TVC led to a significant decrease in  $\text{NO}_x$  emissions of about 25%

# Contents

<b>List of Figures</b>	<b>vi</b>
<b>List of Tables</b>	<b>vii</b>
<b>List of Abbreviations</b>	<b>viii</b>
<b>List of Symbols</b>	<b>ix</b>
<b>1 Introduction</b>	<b>1</b>
<b>2 Background Information</b>	<b>3</b>
2.1 Hydrogen Energy . . . . .	3
2.1.1 Production Methods . . . . .	3
2.1.2 Storage Methods and Management . . . . .	4
2.1.3 Power Generation with Hydrogen . . . . .	4
2.1.4 Hydrogen's Climate Assessment . . . . .	5
2.2 Flame Dynamics . . . . .	7
2.2.1 Laminar Premixed Flame . . . . .	7
2.2.2 Laminar Non-premixed Flame . . . . .	8
2.2.3 Turbulent Flame . . . . .	8
2.2.4 Differential Diffusion . . . . .	11
2.3 Aero-Engine Combustors . . . . .	11
2.3.1 Combustor Design Criteria . . . . .	12
2.3.2 Conventional Combustor Design . . . . .	12
2.3.3 Lean Premixed vs. RQL Combustion Technology . . . . .	13
2.3.4 Hydrogen Combustor Concepts . . . . .	15
2.4 Trapped Vortex Combustor Systems . . . . .	16
2.4.1 Trapped Vortex Geometry . . . . .	17
2.4.2 Trapped Vortex Combustor Characteristics . . . . .	17
2.4.3 Trapped Vortex Combustion Technologies . . . . .	18
2.5 Theoretical Framework . . . . .	19
2.5.1 Governing Equations . . . . .	19
2.5.2 Large Eddy Simulation (LES) Approach . . . . .	20
2.5.3 Chemical Kinetics . . . . .	22
2.5.4 Diffusive Flux Modelling . . . . .	23
2.5.5 Turbulence Modelling . . . . .	24
2.5.6 Turbulence-Chemistry Modelling . . . . .	25
<b>3 Methodology</b>	<b>28</b>
3.1 1D Hydrogen Flame Analysis . . . . .	28
3.1.1 Case Description . . . . .	28
3.1.2 Chemical Time Scale . . . . .	29
3.1.3 Modelling Approach . . . . .	29
3.1.4 Numerical Setup . . . . .	30
3.2 Trapped Vortex Combustor Analysis . . . . .	30
3.2.1 Design Philosophy . . . . .	30
3.2.2 Design Specifications . . . . .	30
3.2.3 Final TVC Model . . . . .	33
3.2.4 Modelling Approach . . . . .	34

---

3.2.5	Numerical Setup . . . . .	35
3.2.6	Boundary Conditions . . . . .	36
3.2.7	Mesh Independence & Quality Assessment . . . . .	37
3.3	Numerical Validation Study . . . . .	39
3.3.1	Validation Case . . . . .	40
3.3.2	Modelling & Numerical Setup . . . . .	40
3.3.3	Mesh Independence & Quality Assessment . . . . .	41
<b>4</b>	<b>Results &amp; Discussion</b>	<b>43</b>
4.1	1D Hydrogen Flame Results . . . . .	43
4.1.1	Mixture Temperature . . . . .	43
4.1.2	Flame Characteristics . . . . .	44
4.1.3	Chemical Reactivity . . . . .	45
4.2	Results of the Numerical Validation Study . . . . .	46
4.2.1	Velocity field . . . . .	47
4.2.2	Temperature field . . . . .	48
4.2.3	Turbulence Intensity . . . . .	49
4.2.4	Turbulent Flame . . . . .	49
4.3	Trapped Vortex Combustor Results . . . . .	50
4.3.1	Cold Flow . . . . .	50
4.3.2	Fuel-Air Mixing Quality . . . . .	52
4.3.3	Reactive Flow . . . . .	56
4.3.4	Sensitivity Analysis of H <sub>2</sub> Injection Temperature . . . . .	60
<b>5</b>	<b>Conclusion &amp; Recommendations</b>	<b>64</b>
5.1	Recommendations: . . . . .	65
	<b>References</b>	<b>66</b>
<b>A</b>	<b>ESF_fBilgerFoam Solver</b>	<b>70</b>
A.1	Description of the Computational Method . . . . .	70
A.2	Code Modifications . . . . .	70
<b>B</b>	<b>Setup of the Validation Study</b>	<b>72</b>
B.1	Boundary Conditions . . . . .	72
B.2	Numerical Setup . . . . .	73

# List of Figures

2.1	Schematic representation of pathways involved in NO <sub>x</sub> formation for H <sub>2</sub> /air combustion.	6
2.2	Schematic representation of a freely propagating laminar premixed flame. [13]	7
2.3	Flame regime diagram for turbulent premixed combustion [15]	10
2.4	Flame regime diagram for turbulent non-premixed combustion [16]	10
2.5	Illustration of the thermo-diffusive instability and its effect on the flame front. [19]	11
2.6	Schematic representation of an conventional swirl-stabilised combustor. [20]	12
2.7	Schematic overview of the lean premixed & RQL combustion process. [22]	13
2.8	TAPS injection system and overall combustion process, adapted from [23]	14
2.9	Schematic Overview of the Combustion Process of a RQL Combustor [24]	15
2.10	Schematic overview of a swirl-stabilised combustor with axial injection [26]	15
2.11	Schematic overview of a multi-point LDI combustor, adopted from [27]	16
2.12	Schematic Overview of a Trapped Vortex Combustor (TVC) [28]	16
2.13	Representation of Current Trapped Vortex Combustors Designs [30] [31]	17
2.14	Schematic of a TVC equipped with Lean Premixed Combustion Technology [28]	18
2.15	Schematic of a TVC equipped with RQL Combustion Technology [28]	19
2.16	Detailed Reaction Mechanism for H <sub>2</sub> /O <sub>2</sub> /N <sub>2</sub> [31]	22
3.1	Schematic of a reactants-to-products counterflow configuration, adapted from [43]	29
3.2	Schematic 2D representation of the final TVC model (all dimensions in mm).	33
3.3	Schematic 3D representation of the final TVC model.	34
3.4	Initial mesh with about 4.5 M cells, and refinement in the critical regions.	37
3.5	Results of the mesh independence study for the TVC model, comparing meshes with 4.5M, 6.5M, and 8.8M cells.	38
3.6	Pope criterion for the TVC model, including the sections considered in the mesh independence study.	39
3.7	Schematic 2D representation of the validation model (all dimensions in mm).	40
3.8	Results of the mesh independence study for the validation model, comparing meshes with 1.2M, 2.1M, 3.38M, and 4.0M cells.	41
3.9	Pope criterion for the validation model, including the sections considered in the mesh independence study.	42
4.1	Mixture temperature of the reactants as a function of hydrogen's injection temperature for hydrogen flames with an equivalence ratio ranging from $\phi = 0.5$ to 5.0.	43
4.2	Adiabatic flame temperature for freely propagating hydrogen flames with an equivalence ratio ranging from $\phi = 0.5$ to 4.5 and reactant temperatures between 200 K and 625 K.	44
4.3	NO and NO <sub>2</sub> emission index for freely propagating hydrogen flames with an equivalence ratio ranging from $\phi = 0.5$ to 3.5 and reactant temperatures between 200 K and 625 K.	45
4.4	Variation of the chemical time scale with hydrogen's injection temperature in a reactants-to-products counterflow configuration at a strain rate of $a = 100 \text{ s}^{-1}$ .	46
4.5	Time-averaged axial velocity map for the validation model, comparing LES results with quasi-DNS data.	47
4.6	Comparison of time-averaged axial velocity profiles between the LES simulation and quasi-DNS data at axial locations B = 0.75 mm and C = 2.25 mm.	47
4.7	Time-averaged temperature field for the validation model, comparing LES simulation results with quasi-DNS data.	48
4.8	Comparison of time-averaged temperature profiles between the LES simulation and quasi-DNS data at axial locations B = 0.75 mm and C = 2.25 mm.	48

4.9	Turbulence intensity profile for the validation model, normalised by the main inlet velocity of 150 m/s, and taken at the centerline comparing LES simulation results with quasi-DNS data. . . . .	49
4.10	Time-averaged and instantaneous OH distribution for the validation model, comparing LES simulation results with quasi-DNS data. . . . .	50
4.11	Time-averaged velocity magnitude ( $\bar{u}$ ) map and streamlines of the cold flow established within the baseline TVC. . . . .	51
4.12	Turbulent velocity fluctuations (RMS) map of the cold flow established within the baseline TVC. . . . .	51
4.13	Streamlines and vortical structures formed within the cavity during cold flow conditions, for injection angles ranging from $\theta_{inj} = 30^\circ$ to $60^\circ$ . . . . .	52
4.14	Turbulence intensity of the cold flow established in the cavity, for injection angles ranging from $\theta_{inj} = 30^\circ$ to $60^\circ$ . . . . .	53
4.15	Vorticity of the cold flow established in the cavity, for injection angles ranging from $\theta_{inj} = 30^\circ$ to $60^\circ$ . . . . .	53
4.16	Time-averaged equivalence ratio, complemented with contour lines formed within the cavity during cold flow conditions, for injection angles ranging from $\theta_{inj} = 30^\circ$ to $60^\circ$ . . . . .	54
4.17	Histogram based on the equivalence ratios found in the cavity, for injection angles ranging from $\theta_{inj} = 30^\circ$ to $60^\circ$ . . . . .	55
4.18	Equivalence ratio profiles at the outlet of the TVC, for injection angles ranging from $\theta_{inj} = 30^\circ$ to $60^\circ$ . . . . .	55
4.19	Time-averaged velocity magnitude ( $\bar{u}$ ) map and streamlines of the reactive flow established in the TVC. . . . .	56
4.20	Time-averaged temperature ( $\bar{T}$ ) of the reactive flow established in the baseline TVC. The stoichiometric contour ( $Z = 0.028$ ) is highlighted in white, while contours near the lean ( $Z = 0.0042$ ) and rich ( $Z = 0.168$ ) flammability limits are shown in red. Zones 1–3 indicate characteristic regions used to describe the combustion process. . . . .	57
4.21	Time-averaged distribution of $H_2$ of the reactive flow established in the TVC. . . . .	58
4.22	Time-averaged distribution of $O_2$ of the reactive flow established in the baseline TVC. . . . .	58
4.23	Time-averaged distribution of $H_2O$ of the reactive flow established in the TVC. . . . .	58
4.24	Time-averaged distribution of OH of the reactive flow established in the TVC, , with the stoichiometric mixture fraction ( $\bar{Z} = 0.028$ ) highlighted in white. . . . .	59
4.25	Time-averaged Flame Index of the reactive flow established in the TVC, with the stoichiometric mixture fraction ( $\bar{Z} = 0.028$ ) highlighted in white. . . . .	60
4.26	Time-averaged distribution of OH within the cavity of the reactive flow, comparing results with hydrogen injection at 300 K and 150 K. The stoichiometric mixture fraction ( $Z = 0.028$ ) is highlighted in white. . . . .	61
4.27	Scatter plot of temperature in the cavity at the latest timestep for injection temperatures of 300 K and 150 K. The stoichiometric mixture fraction ( $Z = 0.028$ ) is shown as a dotted line, while the blue line represents the conditional mean. . . . .	61
4.28	Time-averaged $N_2O$ distribution within the cavity of the reactive flow, comparing results with hydrogen injection at 300 K and 150 K. The stoichiometric mixture fraction ( $Z = 0.028$ ) is highlighted in white. . . . .	62
4.29	Time-averaged NO distribution within the cavity of the reactive flow, comparing results with hydrogen injection at 300 K and 150 K. The stoichiometric mixture fraction ( $Z = 0.028$ ) is highlighted in white. . . . .	62

# List of Tables

3.1	Summary of the operating conditions adopted for the TVC model. . . . .	31
3.2	Summary of the thermodynamic characteristics adopted for the TVC model. . . . .	31
3.3	Summary of the flow characteristics adopted for the TVC model. . . . .	32
3.4	Summary of the numerical setup for the TVC model simulations. . . . .	35
3.5	Boundary conditions for the mass fractions involved in the TVC model simulations . . .	36
3.6	Boundary conditions for velocity, pressure, and temperature involved in the TVC model simulations . . . . .	36
3.7	Mesh quality parameters for the the selected mesh of the TVC model. . . . .	38
3.8	Mesh quality parameters for the the selected mesh of the validation model. . . . .	41
4.1	Emission index of NO (normalised to 15% O <sub>2</sub> ) for the reactive flow, comparing injection temperatures of 300 K and 150 K. Results are presented in units of g NO per kg of H <sub>2</sub> consumed. . . . .	63
B.1	Boundary conditions for the mass fractions involved in the validation model simulations	72
B.2	Boundary conditions for velocity, pressure, and temperature involved in the validation model simulations . . . . .	72
B.3	Summary of the numerical setup for the validation model simulations. . . . .	73

# List of Abbreviations

---

Abbreviation	Definition
BC	Boundary Condition
CFD	Computational Fluid Dynamics
CFL	Courant-Friedrichs-Lewy
DNS	Direct Numerical Simulation
EDM	Eddy Dissipation Model
EI	Emission Index
ERF	Effective Radiative Forcing
ESF	Eulerian Stochastic Field
FDF	Filtered Probability Density Function
FGM	Flamelet Generated Manifold
ICAO	International Civil Aviation Organisation
IEA	International Energy Agency
IEM	Interaction by Exchange Mean model
LES	Large Eddy Simulation
LTO	Landing & Take-Off Cycle
LHV	Lower Heating Value
MFR	Momentum Flux Ratio
PaSR	Partially Stirred Reactor
RANS	Reynolds-Averaged Navier-Stokes
RMS	Root Mean Square
RQL	Rich-burn, Quick-mix, Lean burn
SGS	Subgrid-Scale Stress
SMR	Steam Methane Reforming
TKE	Turbulent Kinetic Energy
TVC	Trapped Vortex Combustor
WALE	Wall-Adapting Local Eddy Viscosity
WGS	Water Gas Shift

---

# List of Symbols

Symbol	Definition	Unit
$Da$	Damköhler Number	[-]
$Ka$	Karlovitz Number	[-]
$Le$	Lewis Number	[-]
$Pr$	Prandtl Number	[-]
$Pr_t$	Turbulent Prandtl Number	[-]
$Re$	Reynolds Number	[-]
$Re_t$	Turbulent Reynolds Number	[-]
$Sc$	Schmidt Number	[-]
$Sc_t$	Turbulent Schmidt Number	[-]

Greek Symbol	Definition	Unit
$\alpha$	Thermal Diffusivity	$m^2/s$
$\alpha_t$	Turbulent Thermal Diffusivity	$m^2/s$
$\delta_L$	Laminar Flame Thickness	m
$\Delta$	LES Filter Width	m
$\theta_{inj}$	Injection Angle	deg
$\kappa$	Thermal Conductivity	W/m.K
$\kappa_2$	von Kármán constant	[-]
$\mu$	Dynamic Viscosity	N.s/m <sup>2</sup>
$\nu$	Kinematic Viscosity	$m^2/s$
$\nu_{SGS}$	Kinematic Eddy Viscosity	$m^2/s$
$\rho$	Fluid Density	kg/m <sup>3</sup>
$\tau_c$	Chemical Time Scale	s
$\tau_k$	Kolmogorov Time Scale	s
$\tau_{mix}$	Mixing Time Scale	s
$\tau_{res}$	Residence Time Scale	s
$\tau_{ij}$	Viscous Stress Tensor	$m^2/s^2$
$\tau_{SGS}$	Subgrid-Scale Stress Tensor	$m^2/s^2$
$\tau_t$	Time Scale of Turbulent Eddies	s
$\dot{\omega}_c$	Reaction Rate of species c	mol/s
$\phi$	Equivalence Ratio	[-]

Latin Symbol	Definition	Unit
$a$	Strain Rate	1/s
$C_p$	Specific Heat Capacity at Constant Pressure	J/kg.K
$C_\mu$	Empirical Wall Model Constant	[-]
$E$	Wall Roughness Parameter	[-]
$E_a$	Activation Energy	J
$h$	Sensible Enthalpy	J/kg
$I$	Turbulence Intensity	%
$J_c$	Diffusive Flux of Species c	mol/s <sup>2</sup> .s
$k_R$	Reaction Rate Constant	[-]
$k_{res}$	Resolved Turbulent Kinetic Energy	J/kg
$k_{SGS}$	Subgrid-Scale Turbulent Kinetic Energy	J/kg
$K$	Local Stretch Rate	1/s
$l_t$	Integral Length Scale of the Large Eddies	m
$L$	Characteristic Length	m
$\dot{m}$	Mass Flow Rate	kg/s
$p$	Pressure	Pa
$S_L$	Laminar Flame Speed	m/s
$t$	Time	[s]
$T$	Temperature	K
$T_r$	Reactant Temperature	K
$T_{ad}$	Adiabatic Flame Temperature	K
$u_i$	Fluid Velocity component in the $i$ -th direction	m/s
$u'$	Fluid Velocity Fluctuations	m/s
$U$	Characteristic Velocity	m/s
$V$	Injection Velocity	m/s
$V_{sys}$	Combustor Volume	kg/m <sup>3</sup>
$V_\infty$	Inlet Velocity	m/s
$\dot{V}$	Volumetric Flow Rate	m <sup>3</sup> /s
$W_{mech}$	Mechanical Power	W
$W_t$	Thermal Power	W
$y^+$	Wall-Normal Height	[-]
$Y_c$	Mass Fraction of species c	[-]
$Z$	Mixture Fraction	[-]

# 1

## Introduction

Addressing global warming and its harmful effects, caused by greenhouse gas emissions remains one of the most critical challenges for society. According to the International Energy Agency (IEA), the global energy demand is growing annually at approximately 0.7%. Currently, over 70% of this demand is met by fossil fuels, which are the leading contributors to greenhouse gas emissions. Although there is a notable increase in clean and renewable energy sources, it highlights the urgent need for innovative solutions and further developments in sustainable technologies. This also relates to the aviation industry, whose environmental impact may not be underestimated. The emissions produced through all aviation activities already account for about 5% of the global greenhouse gas emissions created. Moreover, with air transport growing at an annual rate of about 3.6%, as stated by the International Civil Aviation Organisation (ICAO), the industry's energy footprint is set to continue rising, which will also elevate the share towards global warming. Consequently, the sector's green path forward is of crucial concern and key to ensure a sustainable future.

Accordingly, the pollutant combustion products that must be addressed include, carbon monoxide (CO), carbon dioxide (CO<sub>2</sub>), nitrogen oxides (NO<sub>x</sub>), unburned hydro-carbons (UHC) and smoke. Among these, CO<sub>2</sub> and NO<sub>x</sub> are of primary concern due to their significant contribution to global warming as greenhouse gases. Additionally, emissions such as UHC and smoke degrade local air quality, while CO and NO<sub>x</sub> pose serious threats to human health and the environment. Fortunately, extensive research into lean premixed and RQL combustion techniques has already led to significant NO<sub>x</sub> reductions. However, the reliance on jet fuel inherently prevents the elimination of carbon-based emissions.

Within this context, hydrogen emerges as a highly promising solution. Hydrogen is a carbon-free and clean energy carrier when produced from renewable energy sources. Moreover, it is a particularly sustainable fuel. Its combustion does not produce any carbon-based pollutants, leaving water vapour and NO<sub>x</sub> as the only emissions to be considered. However, hydrogen's unique flame dynamics present substantial challenges for its integration into combustors, requiring a completely new design approach. Among the potential solutions, the trapped vortex combustor (TVC) in the context of RQL combustion has recently gained a lot of attention. This is mainly due to its innovative approach to flame stabilisation, which relies on geometric rather than aerodynamic features. This not only enhances flame stability but also results in a robust and versatile combustion system. Besides, the possibility to operate in a RQL mode ensures low NO<sub>x</sub> emissions, making it a highly sustainable combustor solution.

Currently, however, several critical challenges still persists, preventing the design from achieving its intended performance. This includes achieving thorough mixing before the completion of the chemical reactions, given that hydrogen has an extremely high reactivity. Namely, when the mixing timescale is longer than the chemical timescale, a diffusion flame rather than the desired premixed flame will be established, which undermines the efforts to minimise NO<sub>x</sub> emissions as intended by the RQL strategy.

Extensive research into this has already provided valuable insights and significantly advanced the development of this technology. However, many uncertainties and variables remain unresolved. Specifically, numerous studies on the cold flowfield have focused on enhancing mass exchange and mixing within the cavity and main region. While insightful, these studies are predominantly qualitative, making it challenging to compare and identify the optimal inlet and injection configurations. Next, regarding the reactive flow behaviour, critical aspects remain unexplored, such as the influence of the injection temperatures and equivalence ratio on the combustion process. Additionally, the flame dynamics are often oversimplified, resulting in a lack of accurate and quantitative descriptions of the flames observed.

Therefore, this research is conducted, which aims at further addressing the diffusion flame problem within the cavity by exploring hydrogen's injection temperature as the potential solution. Reducing the injection temperature namely slows down the chemical reactivity, which may help mitigate the imbalance between the mixing and chemical time scale. To assess this hypothesis, a combination of 1D simulations and Large-Eddy simulations are conducted to characterise the combustion process within a TVC, at various hydrogen injection temperatures. Subsequently, the role of this temperature modification on the chemical time scale is evaluated and the overall impact on the RQL effectiveness, measured through  $\text{NO}_x$  emissions, flame stability, and combustion efficiency is assessed.

The overarching objective of this study is thus to aid in the further advancement and deeper understanding of this technology, by providing quantitative results and address the following research question:

**"For a hydrogen-fueled TVC, how does hydrogen's injection temperature impact the effectiveness of the RQL combustion process, measured through flame mode and  $\text{NO}_x$  emissions?"**

This primary research question is further explored through the following sub-questions:

1. What is the effect of hydrogen's injection temperature on the chemical reactivity?
2. Which TVC configuration and accompanied design variables are selected for the LES analysis?
3. To maximise the temperature dependency, what is the highest fuel-air mixing quality achievable within the cavity of the adopted TVC configuration?

The structure of the thesis report is as follows: In chapter 2, the background and literature required to understand the research is elaborated upon. Next, in chapter 3 the design process of the adopted TVC is outlined and the numerical approach taken to perform the simulations is described. Furthermore, chapter 4 presents and discusses the numerical results in detail. Finally, in chapter 5 conclusions are drawn based on the findings, and some recommendations are provided for further research.

# 2

## Background Information

This chapter provides the necessary background information and fundamental physical principles relevant to this research. First, section 2.1, explores hydrogen's potential to act as a clean energy source. Next, in section 2.2, a qualitative description of hydrogen flame dynamics is provided. Following this, the working principles of conventional combustors are outlined in section 2.3. The focus then shifts to trapped vortex combustors (TVC) in section 2.4, where the current technological state is reviewed. Finally, the theoretical framework underlying this research is detailed in section 2.5.

### 2.1. Hydrogen Energy

Hydrogen is the lightest and most basic element in the periodic table and is increasingly seen as indispensable for the global energy transition. When produced from renewable energy sources, hydrogen has the capacity to serve as a clean and versatile energy carrier. Next, its chemical composition and electrochemical properties make it a more sustainable fuel for propulsion and power generation systems as compared to conventional hydrocarbons, offering a pathway towards a sustainable future.

#### 2.1.1. Production Methods

Nowadays, hydrogen is not yet produced on a large scale, mainly because its current applications are limited to the oil refinement industry and the chemical industry, where it is primarily used for ammonia synthesis in fertilizer production. Meanwhile, the valuation of hydrogen as an energy carrier remains very limited. [1] As a result, industries predominantly rely on on-site hydrogen production methods derived from fossil fuels, as they are efficient and remain the most cost-effective.

Among fossil fuel-based hydrogen production methods, the most widely used is Steam Methane Reforming (SMR), which produces so-called grey hydrogen. In this process, natural gas reacts with steam at high temperatures and pressures to produce synthesis gas, which consists of hydrogen, carbon monoxide, and a small amount of carbon dioxide. The carbon monoxide is then subjected to a water-gas shift (WGS) reaction, converting it into carbon dioxide and secondary hydrogen. Another common method for producing grey hydrogen is the partial oxidation of methane with pure oxygen, resulting in a synthesis gas, which is then further processed through a similar water-gas shift reaction, eventually completing the oxidation process of carbon monoxide. Finally, it is also common to conduct this gasification process with coal, though this method is much more carbon-intensive and is therefore referred to as black hydrogen. Overall, while all these methods can produce hydrogen relatively cheaply, they generate significant carbon dioxide emissions, contributing to global warming and undermining efforts for a sustainable energy transition.

In this context, water electrolysis offers a clean alternative for hydrogen production. Namely, the process utilizes an electrolyser that contains a water-based electrolyte and two electrodes, where electricity is applied to initiate an electrochemical reaction, eventually splitting water molecules into hydrogen and

oxygen. Moreover, if the electricity used for this process is generated from renewable sources like wind or solar power, the production method does not emit any pollutants and is referred to as green hydrogen. Furthermore, embedded in this technology lies the opportunity to assess hydrogen as a clean energy carrier and a form of energy storage. Thereby also providing a solution to the intermittency issue of renewable power production and ensuring a stable grid and security of supply. Nevertheless, due to the high capital expenditures and the variability in electricity prices, water electrolysis is currently 4 to 5 times more expensive than fossil-based methods. [2] As a result, it is not yet widely adopted as a preferred approach. The technology requires further development and optimization to advance along the learning curve such that it can become competitive with other hydrogen production methods.

Given the global challenges, transitioning to an economy that focuses on the large-scale production and deployment of green hydrogen appears essential for achieving energy transition towards a sustainable future. This shift would then supply a clean feedstock to industries while also providing a clean energy carrier for power generation, ultimately offering a sustainable solution to diverse energy needs.

### 2.1.2. Storage Methods and Management

While hydrogen exhibits some promising potential as a clean energy carrier, certain characteristics related to its storage, handling, and logistics pose significant challenges and safety concerns that need to be taken care of properly.

At first, the volumetric density of hydrogen at standard conditions is several orders of magnitude smaller than that of hydrocarbons. [3] To address this, various methods can be employed to enhance this value. The most common approach is by compressing hydrogen gas to high pressures, typically around 350 or 700 bar. However, this requires an energy input which is, on average, equal to 10% of hydrogen's energy content. [4] Furthermore, robust and thick cylinders are necessary to withstand these high pressures and prevent leakage. Alternatively, the most compact method for storing hydrogen is by liquefying it. This involves cooling hydrogen to cryogenic temperatures, as its boiling point at atmospheric pressure is 20.3 K. To achieve this a highly energy-intensive process, consuming about 30% of hydrogen's energy content is required. [4] In addition, maintaining these extremely low temperatures demands expensive, specialized tanks, and issues such as boil-off are unavoidable. Recently, methods in which hydrogen is stored in materials through chemical bonds have been explored as well. These include surface adsorption techniques and storage in metal hydrides.

With respect to hydrogen management, some caution is required due to various safety hazards. To begin with, hydrogen is highly diffusive and has a high permeability. Therefore, it can easily leak through seals, cracks and even pores. Fortunately, hydrogen is non-toxic, and because it is lighter than air, any spillage will quickly rise and disperse rather than accumulate at ground level. Nevertheless, mixtures with air should be avoided as the relatively simple chemistry makes hydrogen extremely flammable and reactive. Even at low concentrations, a hydrogen-air mixture can be explosive, and only a minimal ignition source, such as a weak spark, is required to ignite it. [3] Finally, hydrogen tends to deteriorate various metals by enlarging existing cracks and forming brittle compounds, which can ultimately lead to material failure. Due to these factors, hydrogen logistics and deployment are complex, requiring specialized training and strict regulations before large-scale utilization can be safely achieved.

### 2.1.3. Power Generation with Hydrogen

Hydrogen as a fuel contains a substantial amount of chemical energy, with a lower heating value (LHV) of 120 MJ per kilogram. For comparison, kerosene stores about 40 MJ/kg, making hydrogen significantly more energy-dense by weight. [5] For power generation. However, this energy must be converted into useful work. Usually this is done through the use of fuel cells or combustion engines.

**Hydrogen fuel cell:** This is an electrochemical device that performs the reverse reaction of an electrolyzer. In a fuel cell, hydrogen and oxygen (from the air) are supplied to the respective electrodes, where they react spontaneously to recombine into water, thereby generating electricity in the process. Essentially, the chemical energy stored in hydrogen is converted into electrical energy, with water as the only produced byproduct. The efficiency of this process varies with the specific configuration of

the fuel cell and its operating conditions, which can be evaluated using a polarization curve. However, state-of-the-art fuel cells operating at moderate power densities can achieve relatively high efficiencies of around 50%. [6]

In the future aviation industry, fuel cells could be used to power electric motors that drive propellers and fans, providing the necessary thrust for flight. In this context, all direct pollutant emissions would be eliminated and higher efficiencies would be obtained as compared to gas turbines, making it an extremely sustainable and promising concept. Nevertheless, the current technology still faces several limitations and challenges. For instance, the power density levels achievable with fuel cells are relatively limited, restricting their use to small and medium-sized aircraft. Additionally, issues related to thermal management, reliability, and safety must still be addressed. [7] Moreover, this technology requires entirely new aircraft design concepts and strategies, which will take considerable time to develop and integrate on a large scale within the aviation industry.

**Hydrogen combustion:** As mentioned earlier, hydrogen is highly reactive and can easily combust when mixed with air. As a result, a substantial amount of energy is realised, rapidly heating the combustion products, primarily water vapour, to high temperatures. In a gas turbine, this heat is then converted into useful mechanical work by generating a hot, high-pressure gas. Although the combustion efficiency in a gas turbine is generally above 99%, this cycle's overall thermal efficiency typically ranges from 30 - 40%, which is significantly lower compared to fuel cell technology. [3]

In the aviation industry, gas turbines have been extensively used to generate the required thrust by accelerating the incoming airflow. As a result, the technology is highly reliable and has proven its capabilities over time. However, substituting hydrogen for kerosene in the combustion chamber presents significant challenges. The unique flame dynamics of hydrogen, as will be discussed in section 2.2, necessitate a new approach to combustion chamber design. Moreover, while all carbon-based emissions are eliminated, the combustion process still leads to the formation of nitrogen oxides ( $\text{NO}_x$ ), a direct pollutant that remains of concern. Therefore, it is crucial to implement a combustion strategy that disrupts the formation pathways of nitrogen oxides ensuring that this technology can reach its full potential as a highly sustainable technology.

Advancing both technologies is crucial for driving the transition to a sustainable future. However, in the aviation industry, combustion technology enjoys the advantage of being developed and optimized for decades already. The depth of knowledge and understanding in this field is remarkable, and the proven performance and reliability of these systems are well-established. Consequently, focusing on the further development of hydrogen combustion technologies within this sector seems to offer the most feasible and rapid path forward.

#### 2.1.4. Hydrogen's Climate Assessment

Regardless of the technology used, employing hydrogen immediately eliminates all carbon-based pollutants. However, it still produces the by-product water vapour ( $\text{H}_2\text{O}$ ), and in the case of combustion, also nitrogen oxides ( $\text{NO}_x$ ). It is therefore crucial to analyse their formation and assess the environmental effects and impact of these emissions.

$\text{H}_2\text{O}$  is the primary product of the reaction between hydrogen and oxygen, with its production proportional to the amount of fuel consumed. Although often considered harmless, the release of  $\text{H}_2\text{O}$  into the stratosphere has both direct and indirect effects on the climate. Its effective radiative forcing (ERF) is positive and equal to  $2 \text{ mW}/\text{m}^2$ , indicating a minor warming effect. However, this value is so small that its contribution to climate change is generally considered negligible. [8] Indirectly, water vapour also plays a role in the formation of contrails, which are essentially clouds created when the water vapour plume mixes with the cold ambient air. This involves condensation and the nucleation of ice crystals on small particles, making the process highly complex and dependent on various factors such as latitude, altitude, atmospheric conditions, and particle characteristics. Similar to clouds, contrails reflect sunlight while also trapping infrared radiation emitted from the Earth's surface, resulting in a net warming effect. However, the uncertainty of the extent of climate warming as a result of contrails remains very high. [9]

Considering both technologies, hydrogen-fueled systems will emit twice the amount of  $\text{H}_2\text{O}$  as compared to conventional gas turbines, assuming a constant power level. This inevitably increases the probability of contrail formation. However, the by-products of hydrogen combustion do not produce any aerosol particles, which serve as nucleation sites for ice crystals, meaning that contrail formation depends solely on existing particles in the atmosphere. Taking this into account, some studies already predicted that switching to hydrogen would reduce contrail formation, by 40 to 50% for the same aircraft mission profile, compared to traditional gas turbines. [8] While contrail formation is not completely eliminated with hydrogen, the significant reduction represents a step towards more sustainable aviation.

In hydrogen combustion, a series of chemical reactions lead to the production of  $\text{NO}_x$ , a group of pollutants that includes nitric oxide (NO), nitrogen oxide ( $\text{NO}_2$ ), and nitrous oxide ( $\text{N}_2\text{O}$ ). As illustrated in Figure 2.1, several distinct pathways contribute to the production of these species. [10] The primary source and also major contributor is (1) thermal  $\text{NO}_x$ , which is governed by the Zeldovich mechanism. This involves the oxidation of nitrogen in air, which requires a significant amount of activation energy and thus predominantly occurs in high-temperature environments. The second pathway is (2) the NNH pathway, which comes into play when nitrogen is attacked by hydrogen radicals to form NNH. This intermediate species then reacts with atomic oxygen, eventually leading to the formation of NO or  $\text{N}_2\text{O}$ . This mechanism is typically favoured in fuel-rich conditions and regions with high concentrations of H radicals. Finally, the (3)  $\text{N}_2\text{O}$  pathway provides another important route for  $\text{NO}_x$  production. In this process, nitrogen and atomic oxygen undergo a third-body reaction to form  $\text{N}_2\text{O}$ , which is a precursor to NO. Unlike the NNH mechanism, this pathway is favoured in lean combustion regimes and is further enhanced by increased pressure.

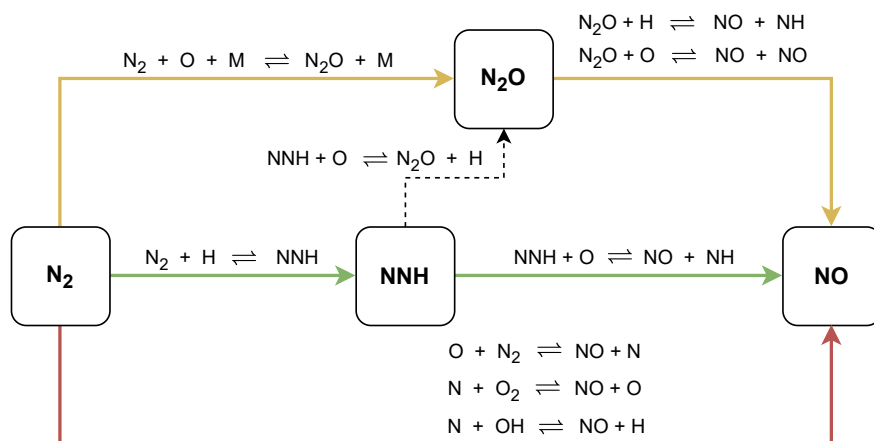


**Figure 2.1:** Schematic representation of pathways involved in  $\text{NO}_x$  formation for  $\text{H}_2/\text{air}$  combustion.

Near the ground, during the landing and take-off (LTO) cycle these  $\text{NO}_x$  emissions deteriorate the local air quality, negatively affecting human health, the environment, and biological systems. [11] In contrast, when emitted in the stratosphere, it primarily contributes to global warming. Specifically, it alters the concentrations of ozone ( $\text{O}_3$ ), methane ( $\text{CH}_4$ ), and water vapour ( $\text{H}_2\text{O}$ ), ultimately causing a substantial warming effect, with an associated radiative forcing of approximately  $14.3 \text{ mW}/\text{m}^2$ . [12] Therefore, its production should be minimised.

The pathways described above are primarily influenced by temperature, pressure, residence time, with less sensitivity to the specific fuel used. Consequently, the strategies developed to reduce  $\text{NO}_x$  formation in traditional gas turbines can be employed for hydrogen combustion as well. When implemented effectively,  $\text{NO}_x$  emissions from both technologies should be comparable. In addition, it is also important to note that hydrogen has a much higher energy density, meaning less fuel is required for the same power output, which naturally leads to a reduction of total  $\text{NO}_x$  emissions. In this context, studies suggest that this could result in an immediate reduction of around 50 - 60%. [8]

## 2.2. Flame Dynamics

Hydrogen combustion, as with combustion processes in general, is highly complex due to its multi-physics nature, including the flow dynamics of multi-component mixtures, heat and mass transfer, and chemical kinetics, all occurring across a wide range of temporal and spatial scales. Therefore, a qualitative description of flames, which encompass the reactive flow region, is essential for understanding and characterising the intricate dynamics of hydrogen combustion.

### 2.2.1. Laminar Premixed Flame

The nature of the flame front is primarily determined by the mixing process of the reactants. When the fuel and oxidizer are thoroughly mixed before entering the combustion region, a premixed flame is established. This type of flame is characterised by a well-defined spatial structure with distinct regions through which the flow propagates, as illustrated in Figure 2.2. Initially, the unburned reactants, set at a specific equivalence ratio, undergo preheating. Next, they enter the reaction zone, where the major chemical reactions and heat release occur. Hence, reactants are rapidly consumed, leading to a sharp temperature increase. Finally, the products move into the post-combustion region, where recombination takes place, and the flame temperature is reached, eventually completing combustion.

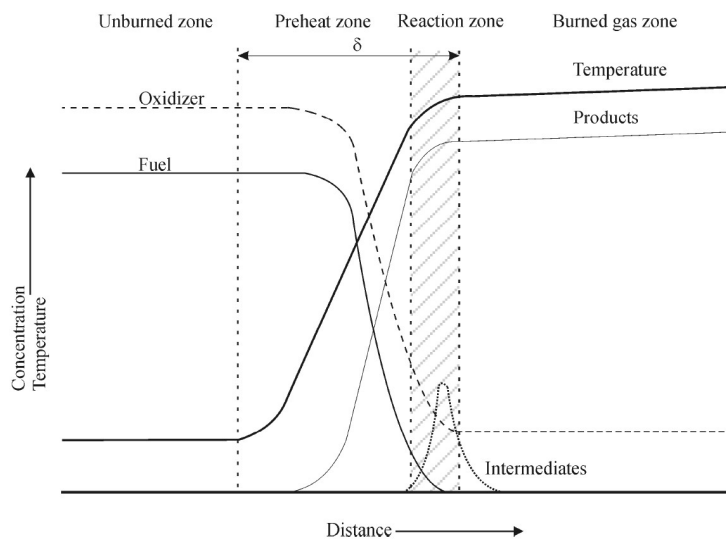


**Figure 2.2:** Schematic representation of a freely propagating laminar premixed flame. [13]

The laminar thickness of the flame ( $\delta_L$ ) is typically small, resulting in steep gradients of species concentration and temperature. Nevertheless, this is essential for the continuation of the combustion process, essentially enabling the flame to become self-sustaining once ignited. Moreover, due to the continuous presence of a flammable fuel-oxidizer mixture, the flame can propagate through the flow at a characteristic flame speed ( $S_L$ ). The interpretation of these flame properties are controlled by the balance between diffusion and the time needed to complete the combustion process, also known as the chemical time scale ( $\tau_c$ ). These in turn are primarily defined by the intrinsic properties of the fuel used and further influenced by factors such as temperature, pressure, and mixture composition, often expressed through the equivalence ratio ( $\phi$ ) at which premixed combustion is taking place.

Hydrogen exhibits exceptional flame dynamics due to its high mass diffusivity and high reactivity, leading to very short chemical time scales for combustion. Under standard conditions and across commonly used equivalence ratios, the flame thickness remains extremely small, typically between 0.03 and 0.05 cm. Additionally, flame speeds of around 3 m/s can be achieved, which is 4 - 5 times faster than that of kerosene. [5] As a result, hydrogen-premixed flames are notoriously difficult to stabilise and are prone to problems such as flashback, where the flame propagates upstream due to an imbalance between the flow velocity and flame speed. This uncontrolled combustion poses significant safety risks, including equipment damage, overheating, and system failure, making effective mitigation essential.

### 2.2.2. Laminar Non-premixed Flame

When the fuel and oxidizer are not properly mixed before entering the combustion region, a non-premixed flame forms. This flame is established at the interface between the fuel and oxidizer, where physical mixing and combustion occur simultaneously. As a result, the flame front is less structured and demonstrates a varying mixture composition, ranging from pure fuel to pure oxidizer. Therefore, to characterise this mixing state within the flame, the mixture fraction ( $Z$ ) is commonly employed. According to Bilger's formulation, which is based on the elemental mass fractions of the species, the mixture fraction for hydrogen combustion is defined as follows: [14]

$$Z = \frac{0.5 \cdot M_H^{-1} \cdot (Y_H - Y_H^O) - M_O^{-1} \cdot (Y_O - Y_O^O)}{0.5 \cdot M_H^{-1} \cdot (Y_H^F - Y_H^O) - M_O^{-1} \cdot (Y_O^F - Y_O^O)} \quad (2.1)$$

In this equation,  $Y_c$  denotes the elemental mass fraction of species  $c$  within the flow, while  $Y_c^O$  and  $Y_c^H$  represent the corresponding elemental mass fractions in the oxidiser and fuel streams, respectively. The term  $M_c$  refers to the molar mass of species  $c$ . Hence, by evaluating this parameter across the flame, valuable insights can be gained into the local mixture composition of the flame.

Depending on this local mixture composition ( $Z$ ) or corresponding equivalence ratio ( $\phi$ ), certain flame characteristics will thus be established. Inevitably, a major part of the flow also passes through the stoichiometric region ( $\phi \approx 1$ ), where combustion is the most intense, featuring large gradients and high temperatures. Furthermore, the progression and completion of the combustion process itself is largely controlled by the diffusion of the reactants rather than the chemical reaction rates, which is why this type of flame is also known as a diffusion flame.

Since mixing is the limiting factor in this type of combustion, it further influences the flame characteristics in several ways. First, the flame cannot propagate freely through the flow and remains confined to the narrow interface where the fuel and oxidizer meet. Additionally, incomplete mixing can result in combustion at suboptimal conditions, thereby producing unwanted by-products and lowering the combustion efficiency. Finally, strain rate, driven by the presence of a velocity gradient thins the flame, which in turn reduces the residence time within the flame locally, promoting incomplete combustion.

As previously noted, hydrogen's chemical time scale is extremely short. Therefore, the mixing time scale ( $\tau_{mix}$ ), determined by the flow dynamics, is often longer. As a result, when not accounted for through premixing systems, hydrogen combustion typically results in the formation of a non-premixed or a partially premixed flame. Although this flame is favoured for its safety and reduced susceptibility to instabilities as compared to premixed flames, it suffers from reduced efficiency and predominantly burns at stoichiometric conditions, resulting in elevated flame temperatures and high production rates of  $\text{NO}_x$ . Given the fact that the adiabatic flame temperature ( $T_{ad}$ ) of hydrogen at stoichiometric conditions is approximately 200 K higher than that of methane, this problem is even further intensified.

### 2.2.3. Turbulent Flame

The flow in a combustion chamber almost always exhibits turbulent behaviour, which is characterised by its chaotic and irregular nature by introducing random velocity and pressure fluctuations throughout the flow. Typically, the onset and intensity of this turbulence is indicated by the Reynolds number, as shown in Equation 2.2, which describes the relative influence between inertial and viscous forces.

$$Re = \frac{\rho UL}{\mu} \quad (2.2)$$

In this equation,  $\rho$  is the density,  $\mu$  is the dynamic viscosity, and  $U$  and  $L$  denote the characteristic velocity and length of the flow, respectively. Hence, significant turbulence will be generated for large Reynolds numbers as flow disturbances are no longer sufficiently damped by the viscous forces.

Overall turbulence can be beneficial as it enhances mass and heat transfer, improving fuel-air mixing. However, it also significantly affects chemical kinetics, influencing the behaviour of the flame front. This complex interaction between turbulence and chemical kinetics, also known as turbulence-chemistry interaction, further categorises the flame into various flame regimes. These regimes are typically defined using a diagram based on three key non-dimensional numbers.

At first, the turbulent Reynolds number is given through Equation 2.3 and characterises the intensity and scale of the turbulent flow. In this equation,  $u'(l_t)$  is equal to the root mean square value of all large-scale fluctuations,  $l_t$  is the integral length scale, and  $\nu$  is the kinematic viscosity.

$$Re_t = \frac{u'(l_t) l_t}{\nu} \quad (2.3)$$

Next, the relationship between the timescale of the largest turbulent eddies ( $\tau_t$ ) and the chemical timescale required for combustion plays a crucial role in characterising the flame regimes. This is defined through the Damköhler number, which is provided in Equation 2.4.

$$Da = \frac{\tau_t}{\tau_c} \quad (2.4)$$

Finally, the Karlovitz number, which outlines the significance between the smallest turbulent eddies, represented by the Kolmogorov timescale ( $\tau_k$ ) and the chemical timescale is also identified as being critical for assessing the different interactions. Its formal expression is given in Equation 2.5.

$$Ka = \frac{\tau_c}{\tau_k} \quad (2.5)$$

The flame diagrams for premixed and non-premixed combustion, visualising the distinct flame regimes based on these parameters, are shown in Figure 2.3 and Figure 2.4, respectively.

Analysis of this former diagram indicates that turbulent flames are observed when the turbulent Reynolds number exceeds 1. Here, the initial regime encountered is the flamelet regime, which is defined by  $Ka < 1$ . This means that the timescales of the smallest eddies are larger than the chemical timescales. The flame is thin and can be approximated by a distribution of laminar flames. In addition, this regime is further differentiated based on the turbulent fluctuations to laminar flame speed ratio ( $u'/S_L$ ). In the wrinkled flamelet regime, turbulent fluctuations are insufficient to significantly interact with the flame. Conversely, in the corrugated flamelet regime, turbulent motions are intense enough to substantially wrinkle the flame, leading to interactions at the flame front. This interaction leads to the creation of pockets containing mixtures of fresh and burnt gases.

The second flame regime, known as the thin reaction zones regime, occurs when Karlovitz numbers range from 1 to 100. In this regime, Kolmogorov time scales become smaller than the chemical time scales, enabling small eddies to influence the flame, thereby enhancing scalar mixing. However, in this regime, only the preheat zone is affected, while the inner reaction zone - where the most intense chemical reactions can be found - is still safeguarded from this effect. [14] As the Karlovitz number exceeds 100, this distinction collapses, and turbulence begins to significantly disrupt the inner reaction zone as well, leading to broken reaction zones, which is also referred to as the distributed flame regime.

In all these cases, the Damköhler number is much larger than 1. Chemical reactions are faster compared to turbulent mixing, hence the flow is defined by the mixing processes. When  $Da < 1$ , the chemical kinetics will dominate the reactions, leading to a well-stirred flame regime.

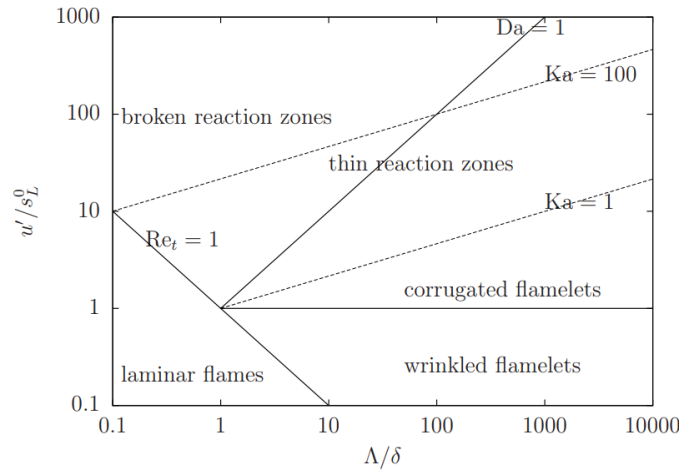


Figure 2.3: Flame regime diagram for turbulent premixed combustion [15]

An analysis of the non-premixed flame diagram, provided in Figure 2.4 reveals that turbulence is also indicated by a turbulent Reynolds greater than 1. Moreover, the further characterization relies solely on the Damköhler number. For large  $Da$  numbers, the chemical reactions are way faster compared to turbulent mixing, resulting in a flame with a laminar structure. Therefore, a flamelet approach is most suitable in this regime.

A reduction of the  $Da$  number implies that the transport of heat and species due to turbulent fluctuations becomes more pronounced than the heat transfer within the flame, leading to a deviation from the laminar flame structure. [16] A distorted flame front and unsteady effects start to occur when the order of the turbulent timescales becomes similar to the chemical timescales. [17] Finally, the flame gets extinguished when the turbulent time scale becomes way smaller than the chemical time scale.

The boundaries of these regimes are marked by two characteristic Damköhler numbers, which vary with the Reynolds number. Namely, increased turbulence leads to larger scalar dissipation rates, which weakens the flame. Therefore, unsteady effects or extinction will occur at higher  $Da$  numbers. [18]

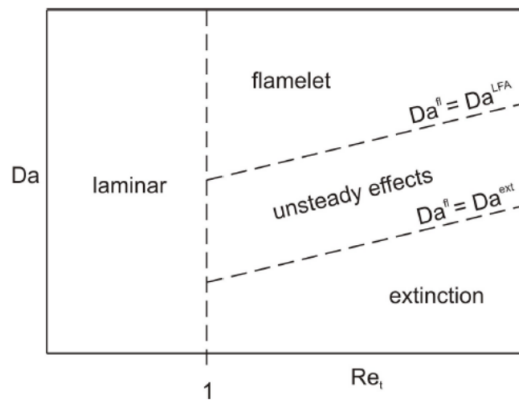


Figure 2.4: Flame regime diagram for turbulent non-premixed combustion [16]

The high Reynolds number, combined with the inherent instabilities present at the inlet of a gas turbine combustion chamber, leads to intense turbulence. As a result, high Damköhler numbers are seen in the flow, and despite the short chemical timescales for hydrogen, high Karlovitz numbers are observed as well. For premixed combustion, this results in a flame which aligns with the distributed flame regime. For non-premixed combustion, this leads to a flame front which falls within the flamelet regime. However, it is crucial to be cautious here as the structure of the reaction region is subjected to spatial and temporal evolution. Hence, it is likely that unsteadiness and extinctions are present in the flame as well.

### 2.2.4. Differential Diffusion

Heat transfer and molecular diffusion of the species available within the mixture tend to play a crucial role in the characterisation of the flame behaviour. Therefore, the flame dynamics can be further defined and differentiated by the non-dimensional Lewis number, presented in Equation 2.6, which captures the relative significance between these diffusive properties.

$$Le = \frac{\alpha}{D} = \frac{\kappa}{D_{im} \rho C_p} \quad (2.6)$$

In this expression,  $\alpha$  represents the thermal diffusivity, which is defined as the thermal conductivity  $\kappa$  divided by the product of the mixture's density  $\rho$  and its specific heat capacity at constant pressure  $C_p$ . In addition, the term  $D_{im}$  denotes the mixture-averaged molecular diffusion coefficient for species  $i$ .

For most hydrocarbon fuels and their combustion products, the Lewis number is typically close to one, indicating that the rates of thermal and mass diffusion are roughly equal. However, as previously noted, hydrogen exhibits significantly higher mass diffusivity. As a result, its Lewis number generally fluctuates around 0.3, indicating pronounced differential diffusion, which alters the flame behaviour. Specifically, hydrogen diffuses into the reaction zone much faster than heat can diffuse away, leading to higher local temperatures and faster chemical reaction rates, which in turn increase flame speed. Additionally, the variation in the Lewis numbers of different species creates localised concentration gradients, potentially resulting in uneven heat release and increased unsteadiness in the flame.

In a premixed flame, differential diffusion can also lead to a thermo-diffusive instability, as is visualised in Figure 2.5. Turbulence induces wrinkles in the flame front, which alters both the molecular concentration and temperature gradients, unbalancing the diffusion rates. When  $Le < 1$ , this imbalance is further amplified by the diffusion coefficients, resulting in increased burning velocities in convex regions and a corresponding decrease in concave regions. This reinforces the wrinkling and acts as a driver of instability. Conversely, when  $Le > 1$ , the diffusion coefficients mitigate the gradient imbalance, reducing flame wrinkling and exerting a stabilizing effect.

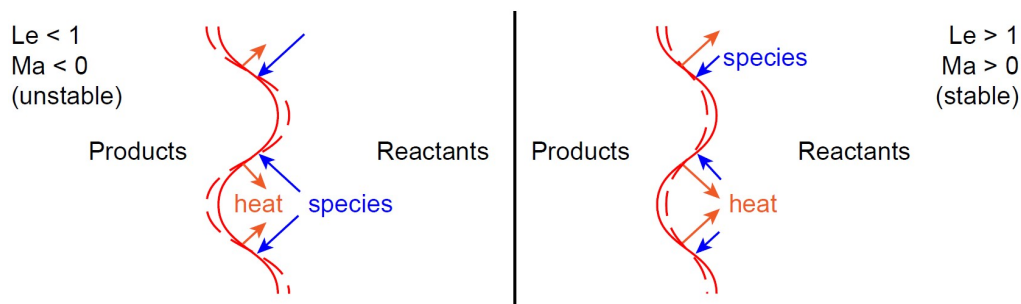


**Figure 2.5:** Illustration of the thermo-diffusive instability and its effect on the flame front. [19]

The significance of differential diffusion effects on the overall flame behaviour highly depends on the relative influence of the other flame dynamics affecting factors such as the operating conditions, mixing process, and turbulence intensity. Therefore, accurately accounting for and comparing these factors is essential for reliably predicting and analysing flame behaviour.

## 2.3. Aero-Engine Combustors

Integrating the challenging flame dynamics of hydrogen into a combustor can be approached from various design strategies, often rooted in the principles of conventional combustors. Therefore, this section reviews conventional kerosene combustion technologies to establish a solid understanding of the design criteria and working principles involved. This foundation then paves the way for exploring potential hydrogen combustor designs.

### 2.3.1. Combustor Design Criteria

Designing an aero-engine combustor involves meeting numerous requirements and constraints. Thereby, the reduction of pollutants is currently of primary concern, given the global challenges. However, several other criteria must also be considered. An overview of the most crucial factors is outlined below:

**Pollutant Emissions:** The negative and harmful effects of pollutants from combustion processes on air quality, human health and climate change are well-known. Therefore, their formation should be minimized or, if possible completely eliminated.

**Combustion Efficiency:** The combustion chamber needs to be designed such that it facilitates sufficient residence time to complete the combustion process. In addition, events such as incomplete mixing and local extinctions should be avoided. Furthermore, across the combustor, a minimal pressure drop is preferred for optimal performance.

**Flame Dynamics and Stability:** Ensuring a stable flame within the combustion chamber is critical for the safe and efficient operation of a gas turbine. Therefore, phenomena such as flashback, blowout, intrinsic instabilities, and combustion instabilities caused by the coupling of the gas dynamic fluctuations and unsteady heat release must be controlled or prevented.

**Lightweight & Compact:** The weight and size of aircraft components are directly linked to aerodynamic performance and, consequently fuel consumption. A lightweight and compact combustion chamber is therefore highly desirable, as it provides both economic and environmental advantages.

Developing a new safe, reliable, efficient, and sustainable aero-engine combustor thus requires carefully considering and balancing all design criteria simultaneously. This, however, often involves making critical trade-offs, as improvements in one area might adversely impact others.

### 2.3.2. Conventional Combustor Design

In Figure 2.6, a schematic illustration of a conventional aero-engine combustor is presented. At the snout, the incoming air is split such that only a small portion is directed straight into the primary zone while the remainder will flow alongside the liner and enters the combustion chamber gradually through several holes present in the secondary and dilution zones. In the primary zone, the air mixes with kerosene to form a partially premixed mixture which is then ignited. In other words, in this region, the flame can be found. Next, the mixture moves into the secondary zone, where the slower chemical reactions are completed, forming the final combustion products. Lastly, in the dilution zone, the temperature of the hot products is reduced to a suitable level by mixing with the remaining airflow, ultimately lowering the equivalence ratio to the desired lean condition.

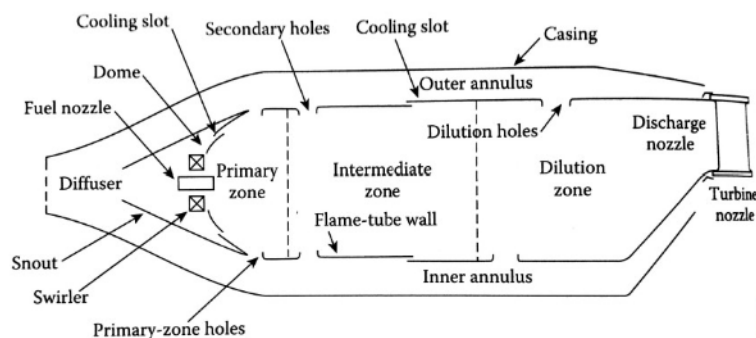


**Figure 2.6:** Schematic representation of an conventional swirl-stabilised combustor. [20]

To acquire flame stabilisation in the primary zone, swirl injectors are typically used. These introduce a vortex breakdown phenomenon which evolves into a central recirculating zone further downstream. Hence, in this zone, hot products are continuously mixed with fresh reactants which stabilises the combustion process. In addition, in the primary zone the flame dynamics of a partially premixed flame,

typically operating at an equivalence ratio of about one, applies, which further enhances the stability. Namely, flame propagation issues such as flashback are eliminated and due to intense combustion at stoichiometric conditions, there is a low sensitivity between flow oscillations and heat release which mitigates the growth of strong amplitude oscillations and thus combustion instabilities. [21]

The recirculating zone, combined with the strategic design of the air inlet holes, enables thorough mixing within the combustor. Additionally, the axial length provides enough residence time for complete combustion to take place. In other words, the conventional combustor is characterised by a high combustion efficiency. Another key advantage of this design is the large amount of air available, which can be used to cool the surrounding chamber and ensure effective acoustic damping.

However, in terms of pollutant emissions, the original technology is no longer acceptable. Namely, the combustion of kerosene results in large quantities of  $H_2O$  and  $CO_2$  emissions, along with smaller amounts of carbon monoxide (CO), unburned hydrocarbons (UHC), and soot. Next, the stoichiometric conditions in the primary zone lead to extremely high flame temperatures, which promotes the formation of thermal  $NO_x$ . From a chemical perspective, significantly reducing  $CO_2$  emissions is virtually not feasible without transitioning to alternative fuels. Nonetheless, research into reducing  $NO_x$  and the other minor pollutants has already led to the development of improved combustion technologies for conventional combustors, as will be discussed in the following section.

### 2.3.3. Lean Premixed vs. RQL Combustion Technology

To effectively reduce nitrogen oxide emissions, it is crucial to target and mitigate the various pathways responsible for their formation, as was discussed in subsection 2.1.4. In numerous instances, this primarily involves addressing thermal  $NO_x$ . Consequently, strategies have been and continue to be developed to control and lower the flame temperature in the combustion chamber. Generally, two viable approaches, schematically shown in Figure 2.7 and described below can be employed to achieve this.

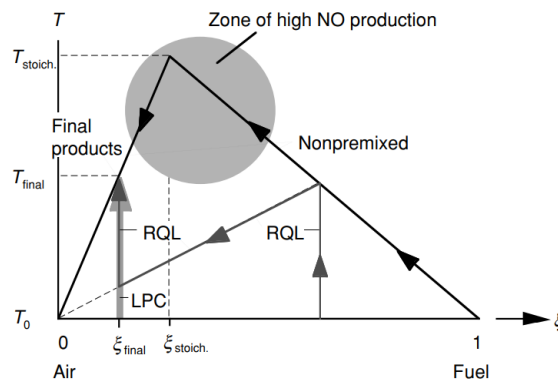


Figure 2.7: Schematic overview of the lean premixed & RQL combustion process. [22]

**Lean premixed technology:** This strategy relies on premixing air with fuel such that a lean mixture is created in the primary zone, prior to ignition. In this way, the released thermal energy is distributed across a large amount of air, preventing high flame temperatures to be reached. Hence, the production of  $NO_x$  is drastically reduced. Nevertheless, it is important to note that the effectiveness heavily depends on the quality of the mixing process. If premixing is not thorough and rapid, a diffusion flame may develop rather than a premixed flame, which would undermine the efforts to reduce  $NO_x$  emissions.

In terms of flame stabilisation, this technology faces significant challenges. At low equivalence ratios, the flame is weak, which increases the risk of localized extinctions or even complete flame-out. Moreover, the technology is vulnerable to instabilities. Since the reactants are premixed, the flame can propagate through the combustor, necessitating careful flashback control. Besides, small flow disturbances lead to substantial fluctuations in heat release. [21] These fluctuations, when interacting, may result in severe combustion instabilities, which complicates the combustion process even more.

As a result of these factors, the operating range of this technology is quite narrow. Therefore, fuel staging is often necessary to maintain operation at low power settings without having extinction problems. Furthermore, altitude relight and ignition capabilities are limited and require careful management.

In summary, the lean premixed approach presents significant opportunities for reducing pollutant emissions, but it comes with the trade-off of increased challenges in flame stability and safety. A notable and successful development and implementation of this technology, employing kerosene is the Twin Annular Premixed Swirler (TAPS) combustor, as illustrated in Figure 2.8.

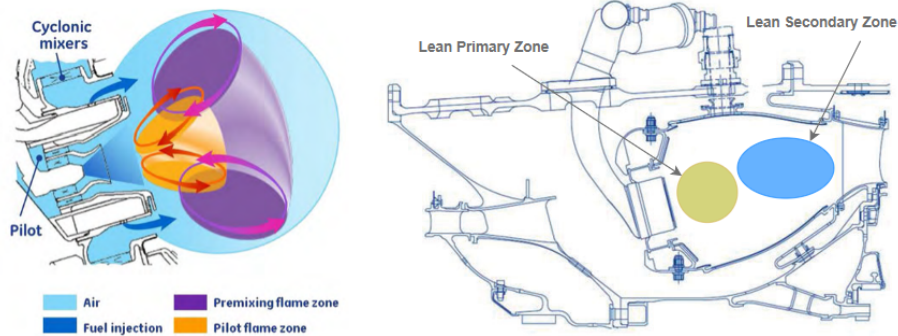


Figure 2.8: TAPS injection system and overall combustion process, adapted from [23]

**Rich burn, Quick mix, and Lean burn (RQL):** The second approach comprises three steps for emission control. Initially, in the primary zone, an excess of fuel is introduced to create a rich-burn condition. Following this, a substantial amount of air is injected into the hot products via multiple jets to create a quick-mixing zone. The reason for this is to quench the flame and rapidly shift the equivalence ratio to the lean side. In the final stage, this lean mixture is burned, facilitating the oxidation of CO and other pyrolyzed hydrocarbons, effectively completing the combustion process at the desired lean conditions.

This combustion technology ensures minimal  $\text{NO}_x$  production by avoiding regions of high flame temperatures. Namely, in optimal conditions, combustion occurs only in the rich primary zone and the final lean zone. The effectiveness of this RQL scheme, therefore, heavily depends on the quenching region as it involves transitioning through stoichiometric conditions, which are highly susceptible to  $\text{NO}_x$  production. Thus, the primary challenge of this technology is to swiftly integrate air into the rich-burn effluent, rapidly establishing lean-burn conditions, and ensuring low  $\text{NO}_x$  formation.

As compared to lean-premixed systems, the establishment of a rich combustion zone offers several advantages. First, the mixture is highly energetic and requires only minimal energy for ignition. Next, the flame exhibits good stability features since there is an abundance of fuel. Flow fluctuations do not significantly impact the ability of the mixture to sustain a flame, and no large heat fluctuations are generated, which reduces the risk of combustion instabilities. Hence, there is a low sensitivity towards the operating conditions. Moreover, due to the injection strategy and mixing process, the risk of flashback phenomena is non-existing.

Despite its advantages, this combustion technology has an inherent flaw. The rich combustion process generates a large amount of unburned hydrocarbons (UHC) and soot particles. Although most of these particles are burned off in the subsequent lean region, turbulence in combination with various local extinctions cause some of these particle concentrations to escape.

In conclusion, the RQL combustion technology successfully maintains low  $\text{NO}_x$  emissions without compromising flame stability. Nevertheless, obtaining rapid mixing in the quick-mixing region is a challenging and complex task. Additionally, high levels of UHC and SOOT have to be considered. A typical RQL combustor, utilising kerosene as fuel is presented in Figure 2.9

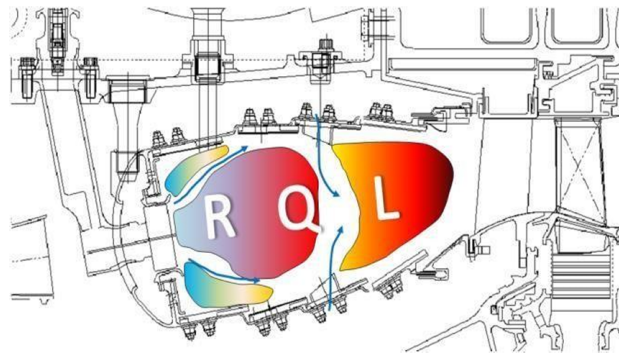


Figure 2.9: Schematic Overview of the Combustion Process of a RQL Combustor [24]

### 2.3.4. Hydrogen Combustor Concepts

The primary motivation for hydrogen combustors is the elimination of the primary product  $\text{CO}_2$  and all other carbon-based pollutants, thereby directly addressing all formation issues associated with these emissions. However, to facilitate the flame dynamics and meet the other design criteria, modifications to the combustion chamber are necessary, and a  $\text{NO}_x$  mitigation method remains essential. Consequently, researchers have proposed various designs, with the most viable ones briefly outlined below:

**Swirl-stabilised with axial injection:** For lean premixed combustion with hydrogen, a straightforward strategy involves the development of a high-swirl stabilised combustor combined with axial injection, as shown in Figure 2.10. Namely, due to hydrogen's high flame speed and reactivity, there is an enhanced risk for propagation issues like flashback or auto-ignition [25]. With this configuration, higher axial velocities along the axis of rotation are generated which pushes the recirculation zone further downstream. This effectively reduces these hazards, making it a practical approach for hydrogen combustors.

Nonetheless, achieving stable and efficient combustion involves more than just managing flashback. The high swirl number can destabilize the flow field, potentially disrupting the formation of the recirculation zone, leading to non-uniform mixing, suboptimal combustion, and increased unsteadiness [26]. Additionally, the intense shear layer and swirling flow contribute to a higher pressure drop. Next, while hydrogen's wide flammability limit offers flexibility, the other challenges inherent to lean premixed systems, as previously discussed, must still be carefully addressed.

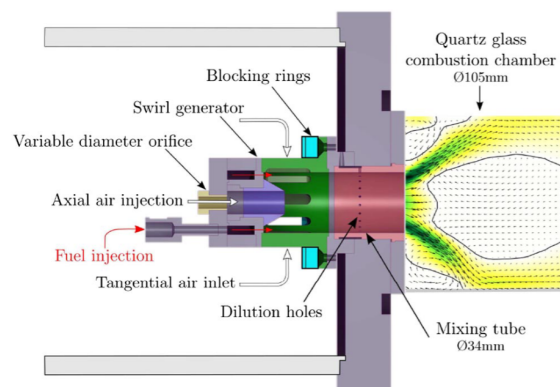


Figure 2.10: Schematic overview of a swirl-stabilised combustor with axial injection [26]

**Multi-point lean direct injection (LDI):** The concept of micro-mixing is an alternative approach for lean premixed combustion, which benefits from avoiding large-scale mixing. The combustor, as shown in Figure 2.11 consists of various tubes through which air is flowing axially, while hydrogen is injected perpendicularly through small, distributed ports in a cross-flow set-up. This leads to rapid and uniform mixing, as it is controlled at the micro-scale, followed by combustion in a multi-zone configuration.

Due to the intricate mixing process, the micro-scale flames, which are established in the shear layer of the recirculation zone behave like diffusion flames, which provides an inherent resistance to propagation [27]. Therefore, flashback is eliminated and moderate flame stability features are obtained. On the contrary, it requires a deep understanding of mixing patterns and residence time. Additionally, the major challenges include manufacturing complexity, sensitivity to fuel impurity, and increased costs.

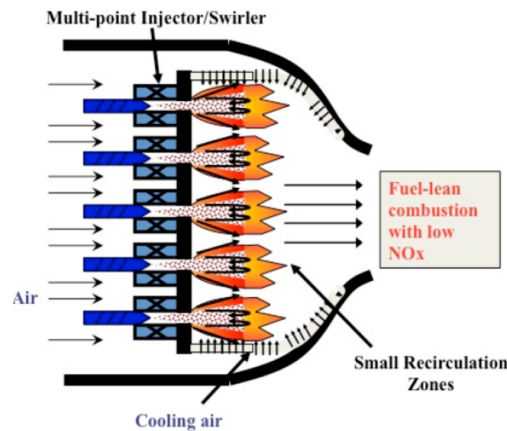


Figure 2.11: Schematic overview of a multi-point LDI combustor, adopted from [27]

**Trapped Vortex Combustor (TVC):** This concept, as illustrated in Figure 2.12 represents a fundamental departure from swirl-stabilised technology by introducing a novel method to flame stabilisation. Namely, specially designed cavities formed by bluff bodies are responsible for generating the necessary recirculation zones. Within these cavities, primary combustion then takes place, thereby anchoring the flame and serving as a stable and continuous ignition source.

The reliance on geometric features rather than aerodynamic phenomena significantly enhances the flame stability. Therefore, it offers great flexibility and robustness, allowing operation in both lean pre-mixed and RQL configurations [28]. However, challenges remain, particularly in achieving optimal mixing and efficient mass transport. Additionally, a more thorough understanding of the intricate flow dynamics remains essential for advancing this technology.

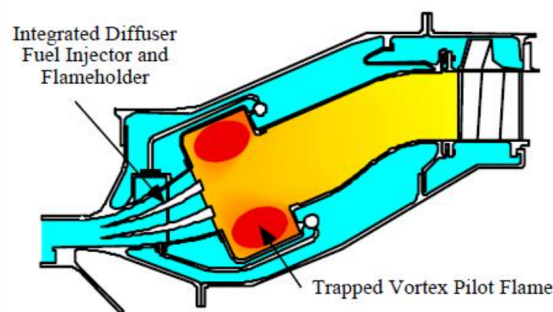


Figure 2.12: Schematic Overview of a Trapped Vortex Combustor (TVC) [28]

## 2.4. Trapped Vortex Combustor Systems

Recently, in the context of hydrogen combustion systems, the trapped vortex combustor (TVC) design has gained significant interest due to its robustness and the various advantages it offers. Consequently, this section provides a detailed overview of the flow and flame characteristics observed within this combustor. Additionally, the current state of the technology is examined, highlighting recent advancements and ongoing developments in the field.

### 2.4.1. Trapped Vortex Geometry

The phenomenon of trapping vortices in cavities was initially studied as a method to reduce drag behind bluff bodies. Namely, research showed that a large, stable vortex could be generated within the cavity if proper cavity dimensions were adopted. This would then allow the mainstream flow to move smoothly over the cavity without separation. It was not until 1995 that Hsu et al. started investigating this feature as a novel approach for flame stabilisation, which eventually led to the development of the first generation of trapped vortex combustors [29]. These early designs already demonstrated that the stable vortex minimized interaction between the mainstream flow and the cavity, prompting the addition of fuel and air injectors directly into the cavity, enabling direct supply of reactants.

Following these initial developments, numerous studies and new generations of TVC's have emerged, each focusing on either understanding or enhancing specific aspects of the technology. Despite this, the fundamental design elements have remained relatively unchanged. To illustrate this, Figure 2.13 shows two recently developed TVC designs. The left figure depicts an axisymmetric rectangular combustor with one cavity on the outer wall. Typically, this design is used for research purposes but it is also being considered for staged combustion applications. The figure on the right shows the more practical annular combustor with one cavity along its circumference, although designs with two cavities are also possible. Because of its space-efficient design, it is also known as an ultra-compact TVC.

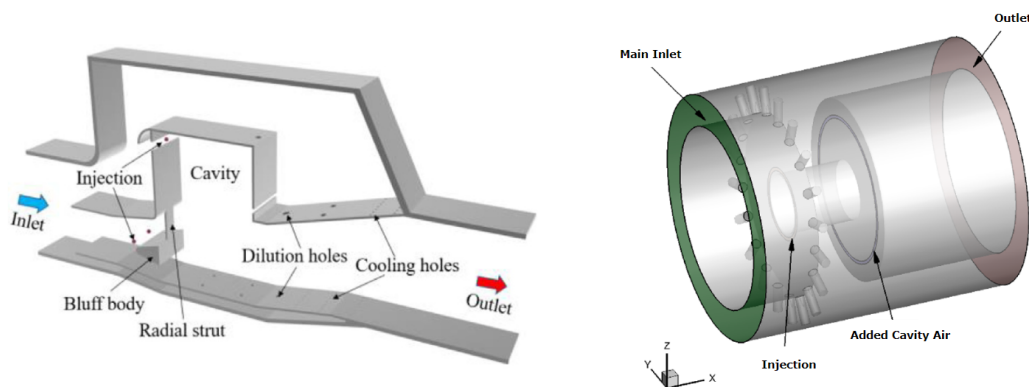


**Figure 2.13:** Representation of Current Trapped Vortex Combustors Designs [30] [31]

### 2.4.2. Trapped Vortex Combustor Characteristics

The unique shape or geometry of the design offers several key advantages. Firstly, it directs the air-flow partially in a radial direction, enabling the desired residence time and combustion efficiency to be achieved within a more compact combustor. This ultimately leads to a lighter system and reduced fuel consumption. Additionally, when properly designed, the streamlines of the developed main flow do not impinge on the cavity walls, which helps to minimize the pressure drop across the combustor

The cavity flow is isolated from the central region, allowing it to be nearly independent of the main flow. Inlet conditions, disturbances and fluctuations upstream only have a minimal impact on the cavity's aerodynamics and flame dynamics. This ensures stable combustion even at very high flow velocities which is particularly beneficial for preventing flashback with respect to premixed combustion. Combined with the strong recirculating flow within the cavity, these factors also provide a high resistance to combustion instabilities, and significantly improves both the lean and rich blow-out limits [28]. Moreover, the ability to ignite the mixture under severe conditions without difficulty also demonstrates the excellent altitude relight capabilities of the design [32].

Opposed to this, the feature of limited interaction between the main flow and the cavity also poses a significant challenge. Namely, the high velocity of the the mainstream flow hinders the transport of hot products from the cavity to the main region [33]. However, effective transport and mixing between these regions are essential for optimal performance and efficiency. Therefore, secondary structures, often referred to as flame-transfer devices needs to be installed in front of the cavity. These can include radial

struts, V-shaped flameholders, or multi-orifice plates, often used in combination with a bluff body. This is illustrated by two examples which are shown in Figure 2.13. While performance varies depending on the configuration, their primary function is to deflect the mainstream flow, creating a low-pressure, low-velocity region, which allows the cavity flow to travel toward the central region [28].

Other challenges associated with this technology include the need for a deeper understanding of the flame dynamics, which are extremely complex due to the combined interactions of boundary layers, shear layers, and vortex aerodynamics. Additionally, the presence of multiple walls may introduce thermoacoustic problems. Finally, the intense heat transfer to the cavity walls, resulting from the hot recirculation zone, shows the necessity of efficient and adequate cooling technologies in order to prevent any damage or failure.

### 2.4.3. Trapped Vortex Combustion Technologies

In addition to the overall characteristics, the performance in terms of flame stability and pollutant emissions is further influenced and defined by the chosen combustion technology. Thus, both approaches are outlined and defined separately below:

**Hydrogen-fueled TVC - Lean premixed technology:** Initially, a pilot flame is created within the cavity. This is done by injecting a lean mixture of hydrogen and air into the hot recirculation zone of the cavity. Subsequently, the hot combustion products from the pilot flame are conveyed to the main region of the combustor. Here, they get mixed with the lean-premixed main flow, eventually leading to the ignition and establishment of the main flame. A schematic overview of this process is presented in Figure 2.14

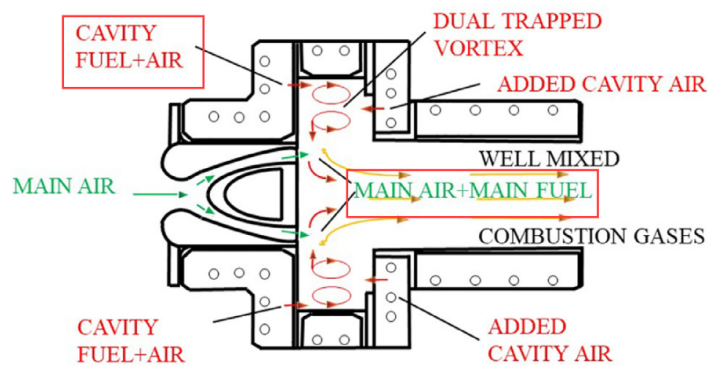


**Figure 2.14:** Schematic of a TVC equipped with Lean Premixed Combustion Technology [28]

This technology relies on the combustion of a lean premixed mixture of hydrogen and air, both in the cavity and the main combustion region. Thus, provided that thorough premixing is achieved, it ensures uniformly low flame temperatures throughout the combustor, which minimises  $\text{NO}_x$  production. Although the lean flames are inherently weak and present various challenges, the TVC technology benefits from its earlier described flow independence, offering at least some improved flame stability as compared to the swirl-stabilised hydrogen combustor concept. Additionally, high inlet velocities can be used to mitigate propagation issues such as flashback in the main combustion region.

**Hydrogen-fueled TVC - RQL technology:** The process begins by injecting hydrogen and air into the cavity under fuel-rich conditions, where thorough mixing and primary combustion occur. The resulting hot combustion products are then transferred to the mainstream flow, where they quickly mix with the incoming stream of air, lowering the equivalence ratio to the lean side. This interface between the fuel-rich cavity and the mainstream flow, therefore, forms the quick-mixing zone. Subsequently, lean combustion takes place, achieving the desired conditions and performance. A schematic of this process is shown in Figure 2.15.

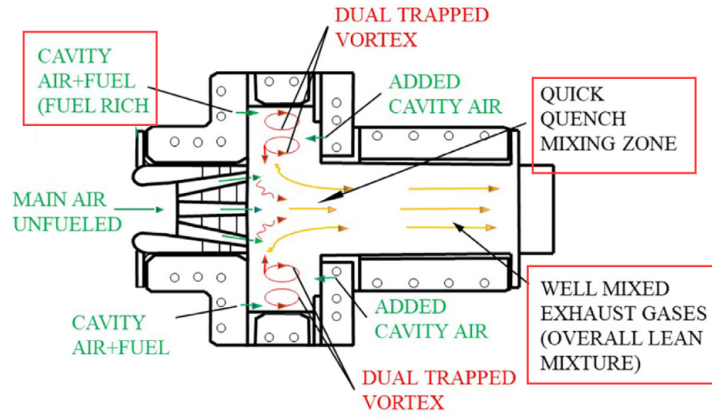


Figure 2.15: Schematic of a TVC equipped with RQL Combustion Technology [28]

The RQL configuration is intended to minimise  $\text{NO}_x$  production. However, this potential is undermined by two key mixing challenges. Firstly, in the cavity, the reactants are injected separately, causing mixing to occur simultaneously with combustion. Hence, to prevent the formation of a diffusion flame, the mixing timescale must be shorter than the chemical timescale, a particularly difficult task given hydrogen's high reactivity [34]. Secondly, the system's overall effectiveness relies heavily on the performance of the quench region. This comprises achieving adequate mass transport, which is already challenging, while also ensuring rapid mixing, further complicating the process. Namely, the hot products from the cavity must swiftly mix with the mainstream flow to prevent excessive  $\text{NO}_x$  formation as the system transitions through stoichiometric conditions.

Although this challenge may seem more complex as compared to the issues present for the lean pre-mixed configuration, the RQL setup offers superior flame stability due to the highly energetic mixture and flow independence [28]. It shows very low sensitivity to disturbances and combustion instabilities. In addition, the configuration is inherently safe, which is a critical advantage.

## 2.5. Theoretical Framework

The performance and characteristics of a combustor can be accurately assessed through experimental methods, providing highly reliable results. However, due to constraints related to cost, time, and safety, the number of experiments that can be conducted is often limited. Consequently, computational methods are often employed to evaluate the flow field and combustion dynamics. Furthermore, unlike experiments, a computational approach allows for flexible design iterations and detailed sensitivity analyses across various parameters, such as operating conditions. Therefore, this section reviews the theoretical framework and modeling elements required for performing accurate numerical simulations.

### 2.5.1. Governing Equations

The physics of a compressible, non-reacting flow with a single species is governed by the fundamental conservation equations for mass, momentum and energy. However, in combustion processes, which involve multiple species that are continuously produced and consumed, these basic laws are no longer sufficient. To fully capture the complex interplay between reactants and products, chemical reactions must be accounted for, along with a species mass transport equation for each chemical species involved. An overview of this set of equations, according to the Eulerian framework is provided below:

**Mass conservation equation:**

$$\frac{\partial \rho}{\partial t} + \frac{\partial \rho u_i}{\partial x_i} = 0 \quad (2.7)$$

As shown in the equation above, the conservation of mass is expressed through a temporal term, representing the rate of change of density over time, and a convective term, which accounts for the transport

of mass due to fluid motion. In this context,  $\rho$  represents the fluid density,  $u_i$  is the velocity component in the  $i$ -th direction,  $t$  denotes time, and  $x_i$  refers to the spatial coordinate.

**Momentum conservation equation:**

$$\frac{\partial \rho u_j}{\partial t} + \frac{\partial \rho u_i u_j}{\partial x_i} = -\frac{\partial p_j}{\partial x_j} + \frac{\partial \tau_{ij}}{\partial x_i} + \rho f_i \quad (2.8)$$

$$\tau_{ij} = \mu \left( \frac{\delta u_i}{\delta x_j} + \frac{\delta u_j}{\delta x_i} \right) - \frac{2}{3} \lambda \left( \frac{\delta u_k}{\delta x_k} \right) \delta_{ij} \quad (2.9)$$

The momentum equation expresses the rate of change of momentum as the sum of forces acting on the fluid element. This includes pressure forces ( $p$ ) arising from pressure gradients and viscous forces, which are accounted for through the viscous stress tensor  $\tau_{ij}$ . As for the body forces, such as gravity, they are generally negligible in combustors and are thus disregarded ( $f_i = 0$ ).

**Species Mass Transport equation:**

$$\frac{\partial \rho Y_c}{\partial t} + \frac{\partial \rho u_i Y_c}{\partial x_i} = -\frac{\partial J_{c,j}}{\partial x_j} + \rho S_c \quad (2.10)$$

Similar to mass conservation, a transport equation can be constructed for each species  $c$  based on its mass fraction  $Y_c$ . However, its formulation requires two additional terms: The first is a diffusion term, represented by the diffusive flux  $J_{c,j}$ , which captures species transport driven by concentration gradients. The second one is a source term, provided by  $\rho S_c$ , which accounts for the production or consumption rate for a given species  $c$ .

**Energy conservation equation:**

$$\frac{\partial \rho h}{\partial t} + \frac{\partial \rho u_i h}{\partial x_i} = \frac{Dp}{Dt} + \tau_{ij} \frac{\partial u_i}{\partial x_j} + \frac{\partial}{\partial x_i} \left( \kappa \frac{\partial T}{\partial x_i} \right) + \frac{\partial q_{id}}{\partial x_i} + S_e \quad (2.11)$$

The energy equation is expressed in terms of sensible enthalpy  $h$ , which is typically used for combustion analysis. The left-hand side includes the temporal and convective terms, capturing the rate of change and transport of enthalpy. On the right-hand side, the first two terms represent the mechanical work contributions from pressure and viscous dissipation. Next, heat diffusion, driven by temperature gradients is modeled using Fourier's law, which incorporates the thermal conductivity  $\kappa$ . Furthermore, the heat flux resulting from species diffusion is depicted by the interdiffusion term  $q_{id}$ . Lastly, the source term, given by  $S_e$ , accounts for the heat released by chemical reactions.

Within a combustor, the combination of high flow velocities and elevated flame temperatures typically results in a Mach number below 0.3. Furthermore, the pressure variation across the flame remains more or less constant. As a result, compressibility effects such as pressure work and viscous dissipation, are minimal and can be safely neglected.

## 2.5.2. Large Eddy Simulation (LES) Approach

The governing equations introduced above are too complex to be solved analytically. Therefore, they must be solved numerically using Computational Fluid Dynamics (CFD). However, when dealing with highly turbulent flows like those in a combustor, this poses an additional challenge. Specifically, performing a Direct Numerical Simulation (DNS) in which the full range of turbulent scales is resolved, demands an extremely fine grid and small time steps, leading to a prohibitively high computational cost.

To address this, two alternative approaches for handling turbulence can be employed. The first is Reynolds-Averaged Navier-Stokes (RANS), where the entire range of turbulent scales is modelled to capture the mean flow behaviour. The second approach is Large Eddy Simulation (LES), in which the

large turbulent scales are directly resolved while the smaller subgrid-scales are modelled. The reason for doing this is based on the energy cascade concept, which states that turbulent energy is generated at large scales and cascades down to the smaller scales, where it eventually dissipates as heat due to viscous effects. As a result, these smaller scales tend to be more uniform, isotropic, and universal which makes accurately modelling easier.

While RANS models are effective for certain analyses, they are generally less accurate, offering only an averaged representation of the mean flowfield and failing to capture unsteady phenomena. In contrast, with advancements in computational power, LES has gained prominence due to its ability to capture transient dynamics and provide more accurate, time-dependent results. Consequently LES is better suited for simulating and evaluating the flow and flame dynamics within a combustor.

The equations for LES are derived through a mathematical filtering operation. In this process, the filter width, denoted by  $\Delta$ , is typically chosen to match the size of a grid cell to maintain consistency with the numerical discretization. Hence, turbulent scales smaller than this cell size are modeled, while larger scales are resolved. In flows with varying density, this filtering operation introduces various unclosed terms. To address this, the Favre averaging method, as defined in Equation 2.12, is employed. This separates the effects of density fluctuations and helps to reduce the number of unclosed terms.

$$\tilde{f} = \frac{\overline{\rho f}}{\bar{\rho}} \quad (2.12)$$

Finally, an overview of the Favre-averaged and filtered LES equations, formulated for turbulent compressible flows, is provided below:

**LES Favre-Averaged Continuity equation:**

$$\frac{\partial \bar{\rho}}{\partial t} + \frac{\partial \bar{\rho} \tilde{u}_i}{\partial x_i} = 0 \quad (2.13)$$

**LES Favre-Averaged Momentum equation:**

$$\frac{\partial \bar{\rho} \tilde{u}_j}{\partial t} + \frac{\partial \bar{\rho} \tilde{u}_i \tilde{u}_j}{\partial x_i} = -\frac{\partial \bar{p}_j}{\partial x_j} + \frac{\partial \bar{\tau}_{ij}}{\partial x_i} + \frac{\partial \bar{\rho} \widetilde{u''_i u''_j}}{\partial x_i} \quad (2.14)$$

In the given equation,  $\widetilde{u''_i u''_j}$ , which denotes the subgrid-scale (SGS) stress tensor  $\tau^{SGS}$ , appears as an unclosed term, representing the influence of the unresolved turbulence scales on the flow field. Therefore, accurately modeling it with the use of a turbulence model is essential.

**LES Favre-Averaged Scalar Equations:**

$$\frac{\partial \bar{\rho} \tilde{\phi}_k}{\partial t} + \frac{\partial \bar{\rho} \tilde{u}_i \tilde{\phi}_k}{\partial x_i} = -\frac{\partial \bar{J}_{k,j}}{\partial x_j} + \left[ \bar{\rho} \tilde{S}_k - \frac{\partial \bar{\rho} \widetilde{u''_j \phi''_k}}{\partial x_j} \right] \quad (2.15)$$

This equation is written in a general form and applies to both the absolute enthalpy and species equations. Therefore,  $\phi_k$  represents the combined vector of the mass fractions and sensible enthalpy. Due to the filtering process, two unclosed terms arise. The first term, written as  $\widetilde{\phi''_k u''_j}$  is called the subgrid scalar flux and accounts for the diffusion caused by the unresolved turbulent scales. The second unclosed term, denoted as  $\bar{\rho} \tilde{S}_k$  is the filtered source term and comprises the reaction rate or heat released from the chemical reactions, which is affected by the resolved flow field as well as the unresolved, turbulent subgrid-scale fluctuations. Deriving a model to close this term, is therefore not trivial.

### 2.5.3. Chemical Kinetics

A combustion process is driven by chemical reactions in which reactants convert into combustion products, thereby continuously producing and consuming chemical species while liberating heat. This can be illustrated by a general reversible reaction with stoichiometric coefficients  $\nu$ :



To account for these chemical reactions, a source term was introduced in the aforementioned scalar equations. By using the principles from chemical kinetics, which studies the rates of reactions and factors influencing them, this source term can be interpreted. Particularly, for a single chemical reaction of a given species  $c$ , the following expression can be defined:

$$\rho S_c = M_c \dot{\omega}_c = M_c \cdot k_R \cdot [X_a]^{\nu_a} [X_b]^{\nu_b} \quad (2.17)$$

In other words, the source term for each reaction can be expressed as the product of the molar mass  $M_c$  and the corresponding reaction rate  $\dot{\omega}_c$ . Moreover, the reaction rate itself predominantly depends on the concentrations of the species involved and the reaction rate constant  $k_R$ , which is generally defined as a function of temperature, through the Arrhenius equation, given by:

$$k_R = A \cdot T^n \cdot e^{-\frac{E_a}{R \cdot T}} \quad (2.18)$$

Apart from temperature, the unknowns in this equation are the Arrhenius coefficients  $A$ ,  $n$ , and  $E_a$ . Here,  $A$  represents the pre-exponential factor,  $n$  denotes the power-law dependence on temperature, and  $E_a$  is equal to the activation energy, which defines the minimum energy required for the reactants to initiate the reaction. Typically, these coefficients are derived from experiments.

In this context, each combustion process is described by a reaction mechanism that provides a comprehensive overview of all species and elementary reactions involved. Additionally, it includes information like the Arrhenius coefficients. By supplying such a mechanism, a chemical solver can compute the detailed chemistry and determine the source terms, facilitating accurate numerical simulations. Depending on the desired accuracy and focus, more detailed mechanisms involving additional species can be employed. For example, a detailed mechanism for hydrogen/air, is provided in Figure 2.16.

No.	Reaction	A	n	$E_a$
1	$\text{H}_2 + \text{O}_2 = 2\text{OH}$	1.70E+13	0.00	47,780
2	$\text{OH} + \text{H}_2 = \text{H}_2\text{O} + \text{H}$	2.16E+08	1.51	3430
3	$\text{O} + \text{OH} = \text{O}_2 + \text{H}$	1.04E+14	0.00	15,310
4	$\text{O} + \text{H}_2 = \text{OH} + \text{H}$	3.82E+012	0.00	7948
5	$\text{H} + \text{O}_2 + \text{M} = \text{HO}_2 + \text{M}$ $\text{H}_2\text{O}/0.0/\text{H}_2/1.5/\text{N}_2/1.26$	5.70E+19	-1.4	0
6	$\text{OH} + \text{HO}_2 = \text{H}_2\text{O} + \text{O}_2$	2.89E+13	0.00	-497
7	$\text{H} + \text{HO}_2 = 2\text{OH}$	7.08E+13	0.00	295
8	$\text{O} + \text{HO}_2 = \text{O}_2 + \text{OH}$	2.85E+10	1.00	-723.9
9	$\text{OH} + \text{OH} = \text{O} + \text{H}_2\text{O}$	3.34E+04	2.42	-1930
10	$\text{H} + \text{H} + \text{M} = \text{H}_2 + \text{M}$ $\text{H}_2\text{O}/12.00/\text{H}_2/2.50$	4.58E+19	-1.40	104,000
11	$\text{H} + \text{H} + \text{H}_2 = \text{H}_2 + \text{H}_2$	1.0E+17	-0.6	0
12	$\text{H} + \text{H} + \text{H}_2\text{O} = \text{H}_2 + \text{H}_2\text{O}$	6.00E+19	-1.25	0
13	$\text{H} + \text{OH} + \text{M} = \text{H}_2\text{O} + \text{M}$ $\text{H}_2\text{O}/0.00/\text{H}_2/3.00$	6.06E+27	-3.32	120,800
14	$\text{H} + \text{O} + \text{M} = \text{OH} + \text{M}$ $\text{H}_2\text{O}/12.00/\text{H}_2/2.50$	4.71E+18	-1.00	0
15	$\text{O} + \text{O} + \text{M} = \text{O}_2 + \text{M}$	6.16E+15	-0.50	0
16	$\text{H} + \text{HO}_2 = \text{H}_2 + \text{O}_2$	2.75E+06	2.09	-1451
17	$\text{HO}_2 + \text{HO}_2 = \text{H}_2\text{O}_2 + \text{O}_2$	4.20E+14	0.00	12,000
18	$\text{H}_2\text{O}_2 + \text{M} = \text{OH} + \text{OH} + \text{M}$	2.38E+19	-0.80	0
19	$\text{H}_2\text{O}_2 + \text{H} = \text{HO}_2 + \text{H}_2$	4.82E+13	0.00	7950
20	$\text{H}_2\text{O}_2 + \text{OH} = \text{HO}_2 + \text{H}_2\text{O}$	1.74E+12	0.00	318
21	$\text{O} + \text{N}_2 = \text{NO} + \text{N}$	1.80E+14	0.00	76,300
22	$\text{N} + \text{O}_2 = \text{NO} + \text{O}$	5.85E+09	1.01	6200
23	$\text{OH} + \text{N} = \text{NO} + \text{H}$	2.80E+13	0.00	0

Figure 2.16: Detailed Reaction Mechanism for  $\text{H}_2/\text{O}_2/\text{N}_2$  [31]

### 2.5.4. Diffusive Flux Modelling

At this point, species diffusion driven by concentration gradients, which is denoted by  $J_{c,j}$  in the species transport equation, is still undefined. To resolve this, Fick's law is commonly employed, which states that the flux is proportional to, but opposite in direction to, the diffusion quantity considered. Hence, for molecular diffusion, this results in the following expression:

$$J_{c,j} = \rho Y_c \vec{V}_c = -\rho D_c \cdot \vec{\nabla} Y_c \quad (2.19)$$

In other words, the diffusive flux of a given species  $c$ , which is provided by the product of the partial density  $\rho_c = \rho Y_c$ , and the diffusion velocity  $\vec{V}_c$ , can be rewritten in terms of the spatial gradient of the species mass fraction along with an associated diffusion coefficient  $D_c$ . The problem, therefore, reduces to determining an appropriate expression for this coefficient.

For a two-species mixture, the diffusion coefficient is a well-defined material property determined by thermodynamic conditions such as pressure and temperature, and can be derived from tables, obtained through experiments. However, when considering a multi-component mixture, the description becomes more complex as the behaviour of each species is influenced by interactions with other species present. Therefore, various approaches can be employed, of which the most common one is the mixture-averaged approximation, which defines the diffusion coefficient as follows:

$$D_{c,m} = \frac{1 - Y_c}{\sum_{c \neq j} X_j / D_{cj}} \quad (2.20)$$

Hence, the diffusion coefficient for a species  $c$  is approximated through a weighted average of the binary diffusion coefficients  $D_{c,j}$  between species  $c$  and each other species  $j$  in the mixture. Thereby, basing the weight on the mole fraction  $X_j$  of these species, which reflects their relative significance.

This approach requires updating the individual diffusion coefficients continuously based on the mole fractions within the mixture, which can be computationally intense. Alternatively, a simpler method is to assume a constant Lewis number for each species. Namely, the Lewis number relates the diffusion coefficient directly to the thermal properties of the mixture, allowing it to be calculated as follows:

$$D_c = \frac{1}{Le_c} \cdot \frac{\kappa}{\rho C_p} \quad (2.21)$$

Using this approach significantly reduces computational complexity, as it only requires a Lewis number for each species. However, it is important to note that this method assumes that mass and thermal diffusion remain proportional, which may introduce inaccuracies in cases where this does not hold.

In the scalar equations formulated for LES, the subgrid-scalar flux term was introduced, which describes the additional interaction or diffusion of the turbulent subgrid-scale fluctuations. To model these terms, a generalised gradient diffusion model is typically used, which results in the following expression:

$$\widetilde{\rho u_j'' \phi_k''} = \Gamma_t \frac{\partial \tilde{\phi}_k}{\partial x_j} \quad (2.22)$$

In this equation,  $\Gamma_t$  represents the turbulent diffusion constant, which corresponds to the turbulent thermal diffusivity,  $\alpha_t$  in the energy equation used in LES, and the turbulent species diffusivity,  $D_t$  in the corresponding species transport equation. Unlike laminar diffusion coefficients,  $\Gamma_t$  is a flow-dependent property governed by the subgrid-scale fluctuations. Therefore, it can be expressed in terms of the eddy-viscosity  $\nu_{sgs}$ , using the turbulent Prandtl and Schmidt number, as shown below:

$$Pr_t = \frac{\nu_{SGS}}{\alpha_t} \quad Sc_t = \frac{\nu_{SGS}}{D_t} \quad (2.23)$$

Typical values for these non-dimensional parameters range from 0.7 - 0.8. [35] However, these may vary slightly depending on the specific application.

### 2.5.5. Turbulence Modelling

In the momentum equation derived for LES, the influence of the unresolved scales on the flowfield is represented by the subgrid-scale (SGS) stress tensor,  $\tau^{SGS}$ . Since this term has a significant effect on the flow dynamics, it requires accurate modelling through a turbulence model.

Assuming that the turbulent stresses behave similarly to viscous stresses in laminar flows, the subgrid-scale tensor can be expressed in a form analogous to the viscous stress tensor, thereby greatly simplifying it and confining all the subgrid-scale effects into a single term. These models, known as eddy-viscosity models, are widely used in practical applications due to their robustness and compatibility with the dissipative nature of subgrid-scale turbulence. An expression of this model is provided below:

$$\begin{aligned}\tau^{SGS} &= \frac{1}{3} \tau_{ij} \delta_{ij} - 2\nu_{SGS} S_{ij} \\ S_{ij} &= \frac{1}{2} \left( \frac{\partial \bar{u}_i}{\partial x_j} + \frac{\partial \bar{u}_j}{\partial x_i} \right)\end{aligned}\quad (2.24)$$

In this equation, the remaining variable to be determined is the turbulent viscosity, or eddy viscosity, denoted by  $\nu_{SGS}$ . Generally, an expression for this term is obtained either through an algebraic relationship, known as a zero-equation model, or by solving an additional transport equation for a variable such as the subgrid-scale kinetic energy ( $k_{SGS}$ ), which is referred to as a one-equation closure.

As previously mentioned, these smaller, unresolved scales tend to be uniform and isotropic. Therefore, zero-equation models are often sufficient to achieve accurate results. Within this context, a simple and efficient approach is the Smagarinsky model, expressed as:

$$\nu_{SGS} = (C_s \Delta)^2 \cdot \sqrt{2\bar{S}_{ij}\bar{S}_{ij}} \quad (2.25)$$

Here, the eddy-viscosity is influenced by the Smagarinsky constant  $C_s$ , the filter width  $\Delta$ , and scales proportionally with the magnitude of the filtered strain-rate tensor  $\bar{S}_{ij}$ . However, this model tends to perform poorly near walls, where turbulence naturally dampens to zero. To address this, additional wall-damping functions, such as van Driest damping, are often applied. Alternatively, a dynamic procedure can be employed, in which the Smagarinsky constant is dynamically adjusted based on the resolved flow scales, improving model accuracy in varying flow regions.

Besides, the applicability of the Smagarinsky model is limited due to its sole reliance on local strain rate, without accounting for rotational strain. Consequently, in flows which exhibit strong rotational effects, this model may yield inaccurate results. To address this, the Wall-Adapting Local Eddy Viscosity (WALE) model can be adopted, in which rotational effects are directly incorporated. [36] Moreover, in this model, the subgrid-scale fluctuations naturally dampens to zero in the vicinity of the wall, which represents another significant improvement and eliminates the need for damping functions or dynamic adjustments. The expression for determining the eddy-viscosity of the WALE model is provided by:

$$\nu_{SGS} = (C_w \Delta)^2 \frac{(s_{ij}^d s_{ij}^d)^{2/3}}{(\bar{S}_{ij}\bar{S}_{ij})^{5/2} + (s_{ij}^d s_{ij}^d)^{5/4}} \quad (2.26)$$

Here, the primary difference as compared to the original Smagarinsky model is the inclusion of the symmetric part of the square of the velocity gradient tensor,  $s_{ij}^d$ , which accounts for both the rotation and strain rates. Additionally, the constant  $C_w$  represent the WALE model coefficient.

Apart from the models outlined above, many others have been developed, each with varying levels of accuracy and focus. Therefore, selecting a suitable model depends on the complexity and specific requirements of the application, with certain models likely to perform better than others.

### 2.5.6. Turbulence-Chemistry Modelling

Based on the flame dynamics, outlined in section 2.2, it is clear that turbulence significantly affects the behaviour of the flame front. In particular, smaller eddies play a major role in modifying the chemical reactions by interacting with the flame at the fine scales. To account for these effects, the filtered source term  $\bar{\rho}\tilde{S}_c$ , introduced in the scalar equations formulated for LES encapsulates both the contribution of the resolved flow field and the turbulence-chemistry interactions from the unresolved scales. Accurate modelling of this coupled term is thus essential for determining precise reaction and heat release rates.

Within this context, various methods are developed to achieve this objective, each with distinct levels of accuracy, complexity, and computation cost. Generally, most of these methods can be categorised in two main groups. The first category assumes that reaction rates are primarily governed by turbulent mixing, with mixing acting as the limiting factor rather than chemical kinetics. Examples include the Eddy-Dissipation Model (EDM) and Partially Stirred Reactor (PaSR). The second and more accurate group of models focuses directly on the chemical kinetics, where uncertainties arising from turbulence-chemistry interactions at the subgrid level are approached from a statistical perspective, through employing filtered probability density functions (PDF). Thereby, this PDF can be determined using a presumed approach, where a predefined shape is imposed, such as in the Flamelet Generated Manifold (FGM) method. Alternatively, a transported approach, where the function is explicitly solved can be taken, such as in the Eulerian Stochastic Field (ESF) method.

An extensive overview of all these models can be found in the literature, such as the turbulent combustion modelling review by Veyante and Vervisch (2002) [37]. Nevertheless, to achieve both robustness and high accuracy, filtered density function methods should be considered. Therefore, these models are concisely presented below:

#### Presumed PDF: Flamelet Generated Manifold (FGM) Method

In this model, a workaround is employed to avoid the calculation of the filtered source term in its original form. Namely, the flamelet approach is based on the idea that in turbulent flames, the local structure or state of the flame can be approximated by a series of laminar flames. In addition, this state can be fully represented using only a few control variables. For partially premixed flames, the mixture fraction ( $z$ ), denoting the mixing state, and a progress variable ( $c$ ), indicating the completeness of the chemical reactions are typically sufficient. In other words, rather than solving the original scalar equations derived for LES, the model substitutes transport equations for these control variables.

The focus thus shifts to modelling the effect of the unresolved scales on both the mixture fraction and the progress variable. By relying on the statistical method, this can be done through an PDF centred around the resolved flowfield values. Hence, the filtered variables, can be determined by integrating the joint probability density function  $\tilde{P}(Z, c)$ , over the control variable itself, as shown below:

$$\tilde{Z} = \int_0^1 \int_0^1 Z(Z, c) \tilde{P}(Z, c) dZdc \quad \tilde{c} = \int_0^1 \int_0^1 c(Z, c) \tilde{P}(Z, c) dZdc \quad (2.27)$$

To simplify the joint PDF, it is generally assumed that the mixture fraction and progress variable are statistically independent. An assumption which allows the joint PDF to be approximated as a product of two separate PDFs: one in the  $Z$ -space and the other in the  $c$ -space. Furthermore, in this framework, each individual PDF is typically presumed to have a  $\beta$ -function distribution. [38] For the mixture fraction this results in the following relation:

$$\tilde{P}(Z) = Z^{a-1} (1 - Z)^{b-1} \frac{\Gamma(a+b)}{\Gamma(a)\Gamma(b)}, \quad a = \tilde{Z}c, \quad b = (1 - \tilde{Z})c, \quad c = \frac{\tilde{Z}(1 - \tilde{Z})}{\tilde{Z}''^2} \quad (2.28)$$

In this equation,  $\Gamma(\cdot)$  denotes the gamma function. Hence, the remaining parameter to be determined is the variance of the control variable, which can easily be obtained by solving an additional transport equation. Eventually, this step completes the modelling work.

In other words, by solving the governing transport equations, the distributions, or FDFs, of the mixture fraction and progress variable can be derived. Next, with these distributions, pre-tabulated databases of laminar flamelets can be accessed to determine the precise values of species mass fractions and the temperature within the turbulent flame, ultimately resolving the flame dynamics. Notably, using these pre-computed chemical states significantly reduces computational costs, enhancing efficiency. [39]

### Transported FDF: Eulerian Stochastic Field (ESF) Method

When directly quantifying the influence of the unresolved subgrid-scales on the reaction rate through the statistical model described above, the filtered source term can be precisely defined as an integral over the joint filtered probability density function (FDF) of all scalar variables involved in the thermophysical state. This relationship is expressed as:

$$\bar{\rho}\tilde{S}_c = \bar{\rho} \int S_c(\Psi; x_i, t) \tilde{P}_{sgs}(\Psi; x_i, t) \quad (2.29)$$

In this equation,  $\Psi$  denotes the sample that encompasses all scalar variables, indicated by  $[\phi_1, \phi_2, \dots, \phi_n]$ . The FDF, however, is an instantaneous statistical quantity that effectively describes the probable states within each computational cell and, as such, requires additional modelling. Instead of presuming a FDF, as is done in the FGM method, a transport equation can be adopted to describe the evolution of the FDF over time. According to Breda et al. (2021) [40] this can be defined as follows:

$$\frac{\partial \bar{\rho}\tilde{P}_{sgs}}{\partial t} + \frac{\partial \bar{\rho}\tilde{u}_j\tilde{P}_{sgs}}{\partial x_j} + \sum_{\alpha=1}^{N_\alpha} \frac{\partial}{\partial \psi_\alpha} (\dot{\omega}_\alpha \tilde{P}_{sgs}) = \frac{\partial}{\partial x_j} \left[ \left( \bar{\rho}D + \frac{\nu_{sgs}}{Sc} \right) \frac{\partial \tilde{P}_{sgs}}{\partial x_j} \right] + \text{micro-mixing} \quad (2.30)$$

Some distinct terms can be identified in this equation: a temporal term, a convective term, and a diffusion term. Next, the chemical source term is expressed in a closed form, providing a clear representation of reaction effects. The micro-mixing term, which accounts for turbulent mixing at the subgrid level, is represented in a general form, as various standard closure models exist in the literature. [41]

Nevertheless, due to the high-dimensional nature of this equation, solving it deterministically on numerical grids is practically infeasible. Instead, an Eulerian stochastic field approach can be employed. This method represents each scalar variable through a finite set of stochastic fields, enabling the computation of averages and fluctuations of that particular scalar considered. These stochastic fields, denoted as  $\zeta_\alpha^n$ , are governed by a transport equation, provided below:

$$d\bar{\rho}\zeta_\alpha^n + \frac{\partial (\bar{\rho}\tilde{u}_j\zeta_\alpha^n)}{\partial x_j} dt + \dot{\omega}_\alpha^n (\zeta_\alpha^n) dt + \frac{\partial}{\partial x_j} \left( \left( \bar{\rho}D + \frac{\nu_{sgs}}{Sc} \right) \frac{\partial \zeta_\alpha^n}{\partial x_j} \right) dt = \bar{\rho} \left( \frac{2\nu_{sgs}}{\bar{\rho}Sc} \right)^{0.5} \frac{\partial \zeta_\alpha^n}{\partial x_j} dW_j^n - \frac{\bar{\rho}}{2\tau_{sgs}} (\zeta_\alpha^n - \tilde{\phi}_\alpha) dt \quad (2.31)$$

In this equation, the first term on the right-hand side represents stochastic micro-mixing, which depends on the diffusion level, the spatial gradient of the field, and is further influenced by a Wiener process. In contrast, the second term on the right-hand side corresponds to the deterministic micro-mixing model, which drives the field toward its filtered mean value. In here, the Interaction by Exchange with the Mean (IEM) model is employed, as is generally done [42]. However, in hydrogen combustion, which is characterised by high diffusivity and strong preferential diffusion effects, this standard micro-mixing model may be insufficient. To improve accuracy, it is often necessary to incorporate species-dependent diffusion coefficients, ensuring a more complete representation.

Subsequently, the results obtained from resolving the Eulerian Stochastic Fields can be integrated statistically to reconstruct the FDF of each scalar variable. Hence, an accurate and comprehensive description of the reactive turbulent flow is now acquired, allowing for the precise determination of the filtered source term. Although this method stands out for its high accuracy in capturing the dynamics of turbulence within the flame, it is important to acknowledge its substantial computational cost. [35] [40]

In conclusion, while both methods are proven to be effectively in capturing turbulence-chemistry interactions, the transported FDF offers an even more robust approach due to its reliance on fewer assumptions about the flame structure and local turbulence effects. It provides a more accurate representation of strong species-dependent diffusion, local extinction, heat losses near the combustor walls, and unsteady mixing dynamics. Therefore, given these advantages, the ESF transported approach is selected in this study to ensure a physically accurate description of the turbulent reacting flow.

# 3

## Methodology

This chapter elaborates on the methodology employed to conduct the numerical simulations, aimed at addressing the research questions. More specifically, in section 3.1 the setup and execution of the one-dimensional (1D) simulations is outlined, which were performed to provide fundamental insights and establish preliminary conclusions. Subsequently, section 3.2 discusses the TVC design that was adopted and details the computational and modelling setup for the series of Large-Eddy Simulations. Finally, section 3.3 outlines the numerical validation strategy implemented, given the absence of publicly available experimental data, to evaluate the reliability and robustness of the adopted methodology.

### 3.1. 1D Hydrogen Flame Analysis

At first, one-dimensional simulations were conducted to evaluate the impact of reducing hydrogen's inlet temperature on the chemical reactivity and flame characteristics. To facilitate this, a series of hydrogen flames relevant to this study were defined, followed by a thorough analysis of the reactive flowfields. Thereby, focussing on deriving key insights into the flame behaviour and the sensitivity to temperature variations, particularly in the most critical and relevant regions linked to NO<sub>x</sub> emissions. For this purpose, CHEM1D, a widely validated CFD tool for 1D laminar flame simulations, was utilised.

#### 3.1.1. Case Description

Initially, the simulation adopted a planar, freely propagating configuration, representing a premixed, unstrained hydrogen flame. Regarding the inputs, the pressure was maintained at atmospheric conditions, while the equivalence ratio ( $\phi$ ) and reactant temperature ( $T_r$ ) were varied. Specifically, equivalence ratios ranging from 0.4 to 5.0 were explored. For the reactant temperature, in which the effect of reducing hydrogen's inlet temperature was the main interest, two scenarios were considered:

1. Cold hydrogen (150–300 K) mixed with air at a typical combustor inlet temperature of 700 K.
2. A scenario designed to achieve and evaluate extremely low temperatures by mixing the same cold hydrogen with air cooled to approximately 300 K.

Consequently, the temperature range of the reactants, determined by the varying hydrogen inlet temperature, was uniquely defined for each equivalence ratio and scenario considered.

The combustion process within the TVC, however, exhibit different characteristics as the fresh reactants continuously impinge on and interact with the hot products available in the cavity. Hence, to capture this, a second series of simulations was performed with a reactants-to-products counterflow configuration, as shown in Figure 3.1. In addition to the original parameters, strain rate ( $a$ ) induced by the velocity gradient had to be specified. However, since this was not the primary focus of the study, a low value of 100 s<sup>-1</sup> was adopted. Furthermore, for the description of the hot products, the design conditions corresponding to an equivalence ratio of 3.5 were chosen as reference.

Both simulations were conducted under premixed conditions, as premixed flames offer a well-defined structure and are straightforward to quantify. While this approach may not fully capture the complexity of the actual combustion process within the TVC, where reactants are injected separately, potentially resulting in a non-premixed flame. The behaviour could be approximated by modelling a series of premixed flames in which the varying equivalence ratio was considered.

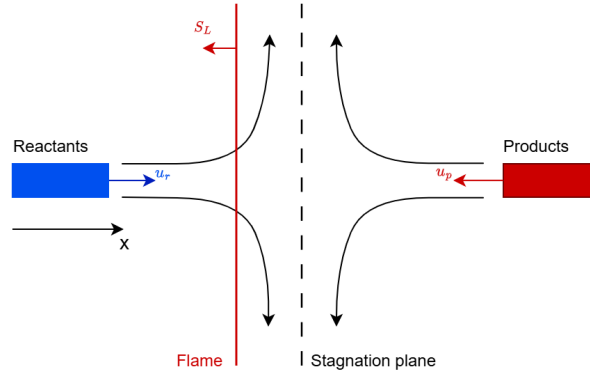


**Figure 3.1:** Schematic of a reactants-to-products counterflow configuration, adapted from [43]

### 3.1.2. Chemical Time Scale

For the flame analysis, the characteristic chemical time scale ( $\tau_c$ ), which is defined as the time required to complete the combustion process, had to be determined. Having the flame results for each simulation case available, this could be achieved in two different ways, as is described below:

$$\text{Method 1: } \tau_c = \frac{\delta_L}{S_L} \quad \text{Method 2: } \tau_c = \frac{\rho Y_{H_2O}}{\dot{\omega}_{H_2O}^{max}} \quad (3.1)$$

As shown in Equation 3.1, the first method calculates the chemical time scale by dividing the laminar flame thickness ( $\delta_L$ ) by the laminar flame speed ( $S_L$ ). In the second method, the chemical time scale is determined by taking the density of the primary combustion product – water vapour, in the case of hydrogen combustion – and dividing it by the maximum reaction rate ( $\dot{\omega}$ ) across the flame.

Both methods were employed in this analysis to ensure a comprehensive and reliable estimation of the chemical time scale. Subsequently, these results could be used to quantify the impact of reducing hydrogen's inlet temperature on the chemical reactivity.

### 3.1.3. Modelling Approach

The set of conservation equations solved by CHEM1D can be derived directly from the governing equations outlined in subsection 2.5.1. Namely, for the freely propagating configuration, they can be obtained by only retaining the x-component terms, reducing the system to a one-dimensional model. For the counter-flow configuration, however, the equations also require the partial inclusion of the tangential y-component, through a local stretch rate ( $K$ ), resulting in a quasi-1D model.

To effectively close the simulation problem, specific models had to be selected first. These included two thermodynamic models: the ideal gas law and the caloric equation of state. Next, viscosity and conductivity were determined using empirical, temperature-dependent laws, while heat capacity and enthalpy were calculated using JANAF polynomials. However, as these polynomials are typically limited to temperatures of 300 K and above, a specialised and validated dataset, provided by Konnov [44], and covering temperatures down to 100 K, was employed in the low-temperature range. For the chemical mechanism, Connaire [45] was selected, which comprises 24 species and details 111 individual chemical reactions. Finally, species diffusion was modelled using a mixture-averaged approach, which utilized the binary diffusion coefficients provided in the mechanism file.

### 3.1.4. Numerical Setup

Regarding the numerical setup, the computational domain was defined with a length of 20 cm and discretised into an uniform mesh of 200 cells. Then, during the simulation, the solver's adaptive mesh refinement algorithm dynamically increased resolution in regions with steep gradients, ensuring high accuracy within the flame. For the numerical schemes, a second-order time integration method was employed, while an exponential scheme was used for spatial discretisation.

The boundary conditions at the left and right ends of the computational domain included the mass fractions, pressure, and temperature of the species. As these values are already clearly described and specified in section 3.1, they are not repeated here. Furthermore, for these simulations, velocity was not explicitly prescribed but was instead calculated by the solver itself. Thereby, the algorithm aimed to stabilize the flame in the central region of the domain and, in the case of the counter-flow configuration, also at the predefined strain rate.

## 3.2. Trapped Vortex Combustor Analysis

To address the other parts of the research questions, detailed simulations were essential. Therefore, a full-scale Trapped Vortex Combustor with a RQL combustion strategy was designed, and its performance was analysed using Large-Eddy Simulations (LES). Thereby, the primary focus was to first assess and enhance the fuel-air mixing quality as much as possible, followed by an evaluation of the injection temperature's influence on the reactive flowfield. Hence, effectively conducting sensitivity analyses. To carry out these simulations, the software package OpenFOAM was utilised.

### 3.2.1. Design Philosophy

Several combustor design parameters were derived from the overall framework of Triathlon, an ongoing research project funded by the European Union's Horizon Europe Research and Innovation Action (RIA) programme and coordinated by TU Delft. The ambition of Triathlon is to develop a disruptive approach towards a low-emission, low-maintenance, and highly responsive hydrogen-electric powertrain for megawatt-class aircraft. Thereby, a crucial aspect of this project is reserved for the development of a turboprop engine featuring a hydrogen-fueled trapped vortex combustor.

For the design of the TVC, Triathlon uses the operating conditions of the PT6A-67D engine as a reference. Specifically, the design is intended for a 19-passenger aircraft, similar to the Beechcraft 1900F, which is currently equipped with this particular engine. To align with this approach, simplify the design process and ensure consistency, the overall geometric characteristics and operating conditions of the TVC considered in this study were also based on the specifications of the PT6A-67D engine. [46]

For the internal configuration of the TVC, including the flame-transfer structure, injection configuration within the cavity, and aerodynamic properties, design choices were primarily based on literature and findings of previous studies. These considerations aimed to maximise the performance and effectiveness of the RQL configuration. Additionally, thermodynamic and combustion characteristics were guided by the CHEM1D results obtained earlier. Finally, some assumptions were made to address uncertainties and close the design problem effectively.

### 3.2.2. Design Specifications

An overview of the design parameters, along with their numerical values, which were adopted for the annular trapped vortex combustor (TVC) is presented below:

**Operating conditions:** It was found that the PT6A-67D reference engine delivers a mechanical power output of 1 MW, at an anticipated cycle efficiency of about 30%, based on the proposed redesign phase and its implications. Furthermore, it operates at a pressure of about 15 bar and it features a combustor inlet temperature of approximately 700 K. Consequently, since these parameters have been integrated directly into the current TVC model, the operating conditions can be summarized as follows:

**Table 3.1:** Summary of the operating conditions adopted for the TVC model.

Parameter	Symbol	Value
Mechanical Power	$W_{mech}$	1.0 MW
Thermal Power	$W_t$	3.3 MW
Operating Pressure	$P$	15 bar
Inlet Temperature (Air)	$T_{Air}$	700 K
Injection Temperature (H <sub>2</sub> )	$T_{H_2}$	150–300 K

The injection temperature of hydrogen was the key design variable considered and used in the sensitivity analysis. Thereby, employing lower values would reduce chemical reactivity, which would lengthen the chemical time scale, potentially improving the effectiveness of the RQL combustion strategy. However, prior studies also indicated that maintaining a minimum temperature of approximately 150 - 200 K is critical to avoid significant density and viscosity fluctuations as well as partial liquefaction during expansion [47]. Therefore, a temperature reduction from 300 K to 150 K was considered in this study.

**Thermodynamic characteristics:** High combustion temperatures are advantageous for improving thermal efficiency but also inherently result in elevated NO<sub>x</sub> production. Moreover, higher flame temperatures reduce the chemical time scale, complicating effective RQL combustion, given hydrogen's high reactivity. Hence, to balance these competing factors, the adiabatic flame temperature within the TVC was carefully limited to 1800 K. With the use of the results from the CHEM1D simulations, discussed in section 4.1, the following thermodynamic characteristics could be determined:

**Table 3.2:** Summary of the thermodynamic characteristics adopted for the TVC model.

Parameter	Symbol	Value
Adiabatic Flame Temperature	$T_{ad}$	1800 K
Equivalence Ratio (Rich)	$\phi_{Rich}$	3.50
Equivalence Ratio (Lean)	$\phi_{Lean}$	0.40
Hydrogen Flow Rate	$\dot{m}_{H_2}$	2.78 g/s
Total Air Flow Rate	$\dot{m}_{Air}$	2.37 kg/s

**Injection configuration:** While various injection strategies have been proposed and analysed in the literature, a quantitative comparison to determine the optimal configuration remains lacking. However, two key features are generally considered. First, the impingement of reactants, which enhances the mixing rate. Second, the promotion of vortical structures, which improves mixing uniformity. Thereby, these individual features can be maximised with an inlet guide vane configuration and an aligned configuration, respectively, as was found in previous studies [31] [48].

To integrate both elements effectively, an aligned configuration was adopted, where both hydrogen and air were introduced from the fore-wall of the cavity, in combination with angled injection. Specifically, angling the air injection toward the fuel facilitated reactant impingement while simultaneously further reinforcing the vortex dynamics. However, to identify the optimal performance, a sensitivity analysis on the injection angle ( $\theta_{inj}$ ) was necessary. Consequently, an additional design variable was introduced, exploring angles from 30° to 60°, with 45° as baseline. Besides, hydrogen was supplied through a row of jets to promote three-dimensional mixing, while air was introduced via a slot for simplicity.

Regardless of the primary injection strategy, a secondary air injection slot was integrated at the aft-wall to establish and reinforce the dual vortex flow pattern. Namely, studies have shown that this further enhances the transport and mixing between the cavity and the main flow region while improving the stability of the primary vortex. Additionally, research indicates that implementing a secondary air slot significantly reduces flow spillage, thereby enhancing overall combustor performance [34].

**Flame-transfer structure:** The inlet configuration of the TVC was designed as a simplified structure featuring a single bluff-body, positioned at the center. This choice was aimed at promoting mass exchange and mixing between the cavity and the main flow region through the recirculation zone that is created due to the sudden expansion and accompanied flow separation downstream of the bluff-body.

Although literature highlighted more advanced configurations, such as bluff-bodies equipped with radial struts, radial flameholders, and multi-orifice plates, this approach was chosen for two key reasons. First, the objective of this study is to analyse the behaviour within the cavity, which does not require the inclusion of 3D inlet structures, further complicating the flowfield. Second, as will be outlined in section 3.3, this approach ensures consistency between the validation model and the current design.

**Flow characteristics:** Flow values had to be specified for both the combustor inlet as well as the cavity injections. Thereby for the inlet velocity, the PT6A-67D reference engine indicated typical values ranging between 50 and 80 m/s. While higher velocities enhance turbulence intensity and mixing efficiency, they also require a larger combustion chamber to maintain sufficient residence time. Therefore, an average inlet velocity of 60 m/s was selected for the TVC under consideration.

With respect to the injection velocities within the cavity, these values were derived and determined based on the momentum flux ratio (MFR), which is defined as:

$$MFR = \frac{\rho_{jet} V_{jet}^2}{\rho_{\infty} V_{\infty}^2} \quad (3.2)$$

Namely, this dimensionless parameter quantifies the relative influence and dominance between two interacting flows. Therefore, this ratio provides valuable insight into the extent of mass exchange and mixing occurring between each two flows considered. Following this, previous studies were consulted to identify optimal ratios in which mixing was maximised [48]. Next, these findings were ultimately used to determine the individual injection velocities of the TVC considered.

For the aerodynamic features, a turbulence intensity of 7% was deemed appropriate for the combustor inlet. Moreover, through incorporating these conditions along with the dimensions, a Reynolds number ( $Re_D$ ) of approximately 162 000 was obtained, indicating moderate to high turbulence across the combustor. A summary of the resulting flow characteristics, as described above, is provided below:

**Table 3.3:** Summary of the flow characteristics adopted for the TVC model.

Parameter	Symbol	Value
Reynolds Number	$Re_D$	162 000
Turbulence Intensity	$I$	7%
Inlet Velocity	$V_{\infty}$	60 m/s
Injection Velocity ( $H_2$ )	$V_{H_2}$	54 m/s
Injection Velocity (Air <sub>primary</sub> )	$V_{air1}$	40 m/s
Injection Velocity (Air <sub>secondary</sub> )	$V_{air2}$	50 m/s

**Geometric characteristics:** To determine the overall scale of the annular TVC, a reference length first needed to be defined. This was achieved by analysing the design philosophy and referencing the PT6A-67D engine. Specifically, this engine's shaft diameter (48 mm) was selected as baseline parameter to define a feasible TVC diameter of 70 mm and a corresponding circumference of 37.07 cm. Next, along with the mass flow rate, this result allowed to determine the inlet height of the TVC.

With respect to the cavities, an aspect ratio ( $L/D$ ) of approximately 1.2 was selected as starting point of the geometric design. This choice was informed by findings in the literature, which indicated that such a ratio enhanced both the stability of the vortices and the mixing efficiency within the cavity [49].

For the dimensions that were still unspecified, a relationship between the combustor volume and the flowfield was employed. Specifically, the volume cannot be arbitrarily chosen but is dictated by the flow to ensure adequate residence time under all operating conditions, ultimately enabling complete combustion. For a reactor without stagnant zones, this is expressed as follows [50]:

$$V_{sys} \geq \dot{V}_r \cdot \tau_{res} \quad (3.3)$$

Accordingly, the minimum required volume ( $V_{sys}$ ) could be determined by calculating the product of the volumetric flow rate of the reactants ( $\dot{V}_r$ ) and the demanded residence time ( $\tau_{res}$ ) based on the conditions present within the cavity and the mean flow region, respectively. To estimate this characteristic time scale, a first-order approximation was assumed by incorporating the most identifiable contributors:

$$\tau_{res} = \tau_{flow} + \tau_{mix} + \tau_c \quad (3.4)$$

In this simplified approach, the residence time was thus taken equal to the sum of the following timescales: First, the flow time ( $\tau_{flow}$ ), representing the time required to bring the reactants together. Secondly, the mixing time scale to reach the combustible mixing state ( $\tau_{mix}$ ). Finally, the aforementioned chemical time scale ( $\tau_c$ ) in order to achieve complete combustion. Following this description, it was eventually possible to determine the individual volumes required, allowing to define all remaining geometric dimensions, essential to the TVC design. To illustrate this, subsection 3.2.3 provides an overview of the final geometric dimensions of the designed combustor.

### 3.2.3. Final TVC Model

With all the design specifications being defined, the annular trapped vortex combustor (TVC) was ready for construction. In Figure 3.2 a schematic 2D representation of the final TVC configuration along with its geometric dimensions is presented.

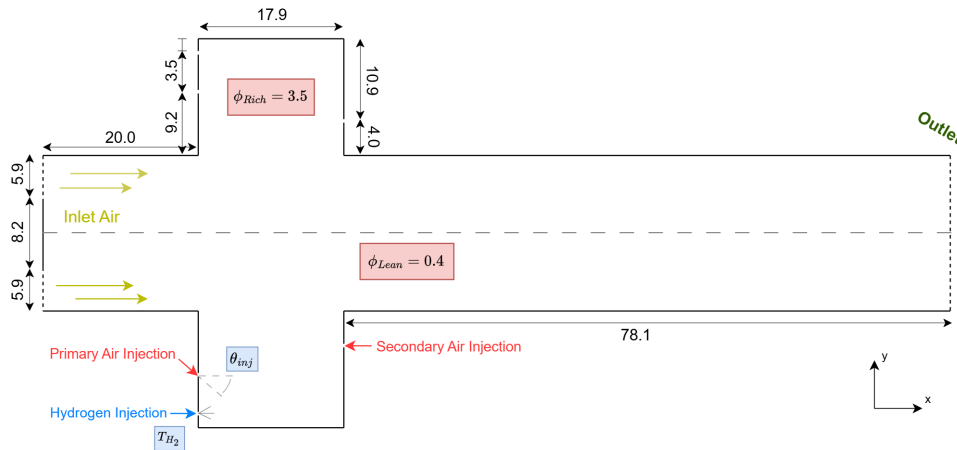


**Figure 3.2:** Schematic 2D representation of the final TVC model (all dimensions in mm).

In the figure above, the two design variables which were evaluated in this study are highlighted. The first is the injection angle ( $\theta_{inj}$ ), investigated to identify the configuration with the best mixing performance. The second is the injection temperature of hydrogen ( $T_{H_2}$ ), studied to assess its sensitivity to the reactive behaviour and its influence on the overall RQL effectiveness within the cavity.

Moreover, to complement the 2D schematic, Figure 3.3 illustrates the 3D segment of the annular TVC geometry which was used in the LES simulations. It is important to note that the annular segment is approximated by considering a constant mean radius throughout the design, resulting in a straight

3D geometry. This simplification was chosen to streamline the CFD geometry construction and ensure identical cavity structures. Furthermore, the distinct boundary patches are clearly highlighted and described, which provides further insight into the three-dimensional nature of the model.

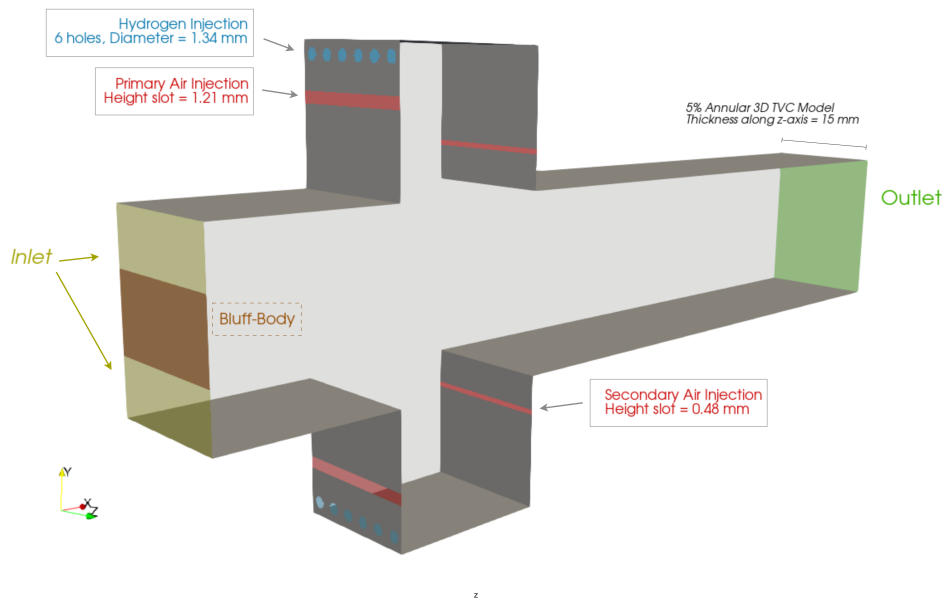


**Figure 3.3:** Schematic 3D representation of the final TVC model.

As shown in the 3D schematic, the segment represents 5% of the total annular circumference, equivalent to 15 mm. This selection was initially based on the ratio of inlet height to domain depth (z-axis) used in the validation model, as described in section 3.3. Subsequently, the chosen depth was evaluated against a preliminary domain size criterion, which requires that at least 1–2 integral length scales should fit within the z-direction. Namely, as established in the literature, satisfying this requirement prevents the artificial suppression of turbulence and ensures resolved flow dynamics [51].

### 3.2.4. Modelling Approach

The flowfields and flame dynamics within the TVC were resolved and evaluated using Large-Eddy simulations. This was accomplished by solving the Favre-averaged and filtered LES equations, as described in subsection 2.5.2, using the open-source software package OpenFOAM.

However, to address the undetermined terms and variables within these equations, appropriate models had to be selected first. This included the adoption of two thermodynamic models: the ideal gas law and the caloric equation of state. Next, Sutherland's law was employed to determine the viscosity and conductivity of the individual species. Additionally, the JANAF polynomials by Konnov [44] were utilized once more to determine the heat capacity and enthalpy, thereby ensuring accurate results in the low-temperature region as well. Finally, species diffusion was accounted for by assuming a constant Lewis number for each species, with these values obtained through CHEM1D simulations.

Moreover, for turbulence modelling, the WALE model was selected to describe the subgrid-scale eddies in the momentum equation. This choice was motivated because of its ability to accurately capture turbulence near walls, a critical feature given the presence of wall-bounded flows in the TVC. Additionally, the subgrid-scale flux terms, representing turbulent species and heat diffusion, were modelled by assuming a constant value for the turbulent Schmidt and Prandtl number ( $Sc_t = Pr_t = 0.7$ ).

For the chemical mechanism, a reduced Connaire [45] scheme comprising 9 species and 20 reactions was used for the cold flow to balance computational efficiency with the need for multiple simulations. However, since this scheme did not include  $NO_x$  species, which were essential for assessing the ef-

fectiveness of the RQL operation in the reactive flow, the well-established NO<sub>x</sub> mechanism for H<sub>2</sub>/air flames described by Capurso [52] was adopted for the reactive flow simulations.

Finally, to accurately represent the turbulent flame dynamics, the interactions between the subgrid-scales and the chemical reactions had to be properly modelled as well. This was accomplished by employing a transported filtered density function (FDF) approach, which was reconstructed using a set of 4 Eulerian Stochastic Fields (ESF) [40].

### 3.2.5. Numerical Setup

Various solvers in OpenFOAM can be used to simulate combustion processes. However, none of them support the ESF method for modelling turbulence-chemistry interactions. Therefore, this study employed a custom solver, *ESF\_fBilgerFoam*, developed and validated by Hansinger et al. (2020) [35], which integrated this advanced modelling capability.

Upon evaluating this solver, although, it was observed that species diffusion could only be modelled under the assumption of a Lewis number equal to one. Therefore, the source code was first modified to incorporate differential diffusion, by allowing to describe a Lewis number for each species involved. In Appendix A, the modifications that were made to the original source code can be retrieved.

As for the discretisation, the details on the meshing of the domain and its assessment are provided in subsection 3.2.7. Next, the initial timestep was set to  $1 \times 10^{-7}$  s, with adaptive adjustments made during the simulation, governed by the Courant-Friedrichs-Lewy condition, defined as [51]:

$$CFL = \frac{V \Delta t}{\Delta x} < C_{max} \quad (3.5)$$

To accurately capture the turbulent macroscopic timescale and minimise numerical damping, the time step must be sufficiently small. Accordingly, based on insights from previous studies within the research group, a CFL value of 0.5 was chosen for the cold flow simulations. In contrast, for the reactive simulations, where chemical reactions significantly accelerated the flow dynamics, a more conservative value of 0.3 was adopted to ensure precise resolution.

Further details on the numerical setup and the applied schemes for both the cold flowfield and the reactive simulations are summarised in Table 3.4:

**Table 3.4:** Summary of the numerical setup for the TVC model simulations.

<b>Numerical Schemes/ Setup:</b>	<b>Cold Flow</b>	<b>Reactive Flow</b>
Temporal Scheme	Implicit Euler, 1st-Order	Implicit Euler, 1st-Order
Momentum Divergence	2nd-Order, limited	2nd-Order, limited
Species Divergence	2nd-Order, limited	2nd-Order, limited
Enthalpy Divergence	2nd-Order, limited	2nd-Order, limited
Chemistry Integration	-	Implicit Euler, 1st-Order
Pressure-Velocity Coupling	PISO + SIMPLE	PISO + SIMPLE
Convergence Rate	$10^{-9}$	$10^{-9}$

To address stability and computational efficiency, a first-order temporal scheme was employed in these simulations. While this approach introduces some numerical dissipation, its impact on accuracy was considered minimal due to the use of a relatively small timestep. Besides, during the ignition phase of the simulation, the chemical time discretisation was replaced with the fourth-order Runge-Kutta scheme, coupled with a CFL value of 0.1, to prevent overflow issues and ensure numerical stability.

### 3.2.6. Boundary Conditions

Various boundary conditions (BC's) had to be specified to accurately capture the physical behaviour and interactions at each boundary patch of the computational domain, thereby ensuring a well-posed mathematical problem. These conditions included specifying the mass fractions of the species involved, of which a detailed summary is provided in Table 3.5.

**Table 3.5:** Boundary conditions for the mass fractions involved in the TVC model simulations

Boundary Patch:	$Y_{H_2}$	$Y_{N_2}$	$Y_{O_2}$
Inlet	0.0	0.767	0.233
Outlet	zeroGradient	zeroGradient	zeroGradient
Hydrogen	1.0	0.0	0.0
Primary Air	0.0	0.767	0.233
Secondary Air	0.0	0.767	0.233
Wall	zeroGradient	zeroGradient	zeroGradient

All other species initialised by the chemical mechanism (e.g., OH, H<sub>2</sub>O, HO<sub>2</sub>) were absent at the start of the simulation. Consequently, their mass fractions were set to 0.0 at the inlets, together with a corresponding *zeroGradient* condition imposed at the outlet and the walls.

Furthermore, an appropriate set of boundary conditions had to be specified for the coupled flow variables, velocity and pressure, along with BC's for the variable, temperature. A detailed overview of these specific conditions can be found in Table 3.6

**Table 3.6:** Boundary conditions for velocity, pressure, and temperature involved in the TVC model simulations

Boundary Patch:	Velocity	Pressure	Temperature
Inlet	60 m/s, $I=7\%$	zeroGradient	700 K
Outlet	zeroGradient	waveTransmissive, 15 bar	zeroGradient
Hydrogen	54 m/s	zeroGradient	150 - 300 K
Primary Air	40 m/s	zeroGradient	700 K
Secondary Air	50 m/s	zeroGradient	700 K
Wall	0 m/s	zeroGradient	zeroGradient

Two key aspects should be highlighted here. At first, at the inlet, the BC for velocity was defined using the *decayingTurbulence* generator, allowing for the specification of an initial turbulence level within the flow. Second, at the outlet, the pressure boundary condition was set to *waveTransmissive* to mitigate artificial reflections of pressure waves caused by compressibility effects.

Based on the mesh assessment study, detailed in the following subsection, the near-wall resolution was found to be insufficient for accurately resolving flow structures in these regions. To address this, a wall model based on the subgrid-scale turbulent kinetic energy was implemented, as described below:

$$\frac{\nu_{SGS}}{\nu} = \left( \frac{\kappa_2 y^+}{\ln(Ey^+)} - 1 \right) \quad (3.6)$$

$$y^+ = C_\mu^{1/4} \cdot y \frac{\sqrt{k_{SGS}}}{\nu} \quad (3.7)$$

In this equation,  $\nu$  represents the kinematic viscosity,  $\kappa_2$  is the von Kármán constant, and  $E$  denotes the wall roughness parameter. Moreover, the wall-normal height  $y^+$  is determined using the subgrid-scale turbulent kinetic energy  $k_{SGS}$ . A more detailed explanation of this model, along with the associated implementation in OpenFOAM, can be found in literature [53].

### 3.2.7. Mesh Independence & Quality Assessment

Constructing and selecting a high-quality mesh with an appropriate cell size is of crucial importance to resolve all relevant flow and flame phenomena and achieve accurate simulation results. Consequently, with respect to this specific configuration, the following considerations were carefully evaluated:

- **Inlet/Injection:** An adequate resolution is essential in these regions to resolve the flow behaviour at the boundaries, and minimise numerical dissipation. Eventually, ensuring that the inflow conditions are accurately represented.
- **Flow dynamics:** The mesh must be sufficiently fine to resolve key flow structures, including the vortical structures within the cavity, vortex shedding at the bluff body, and potential Kelvin-Helmholtz instabilities at the fluid interfaces within the domain.
- **Turbulence:** For accurate turbulence representation, the mesh must resolve a sufficient range of turbulent eddies and their effects on the flow field. In Large Eddy Simulations (LES), the commonly adopted Pope criterion can be employed, which states that at least 80% of the turbulent kinetic energy within the domain should be resolved to achieve reliable results.
- **Flame dynamics:** To accurately resolve the flame and the accompanying steep gradients, the cell size must be smaller than the laminar flame thickness. This ensures that multiple cells lie within the turbulent flame brush, capturing the interactions effectively.
- **Wall region:** Proper resolution near walls is critical to capture the steep gradients. Therefore, the first grid point should be located sufficiently close to the wall, as calculated and evaluated by the wall-normal height,  $y^+$ , which was described earlier. If this is not feasible, wall models must be employed to ensure the accuracy of the simulation in these regions.

Taking into account these factors, along with some first-order estimates of the relevant physical scales, it was considered that a structured mesh with about 4.5 M cells should be appropriate, provided that additional mesh refinement was applied in the most critical regions. These include the cavity as well as the upper and lower wall regions. A visualisation of the initial mesh is provided in Figure 3.4.

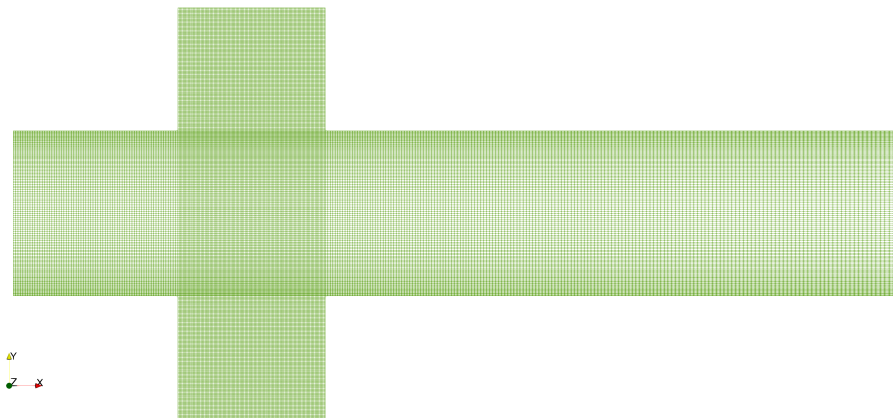


**Figure 3.4:** Initial mesh with about 4.5 M cells, and refinement in the critical regions.

However, to validate that the initial mesh provided accurate and reliable results, a mesh independence study was conducted to assess its performance and verify that it remained unaffected by mesh resolution. For this purpose, two additional structured meshes were generated, comprising approximately 6.5 M and 8.8 M cells. For the analysis, focus lied on evaluating the mean velocity and mean temperature of the cold flowfield at three distinct, yet crucial axial locations within the TVC, as denoted in Figure 3.6. The outcome of the mesh independence study can be found below:

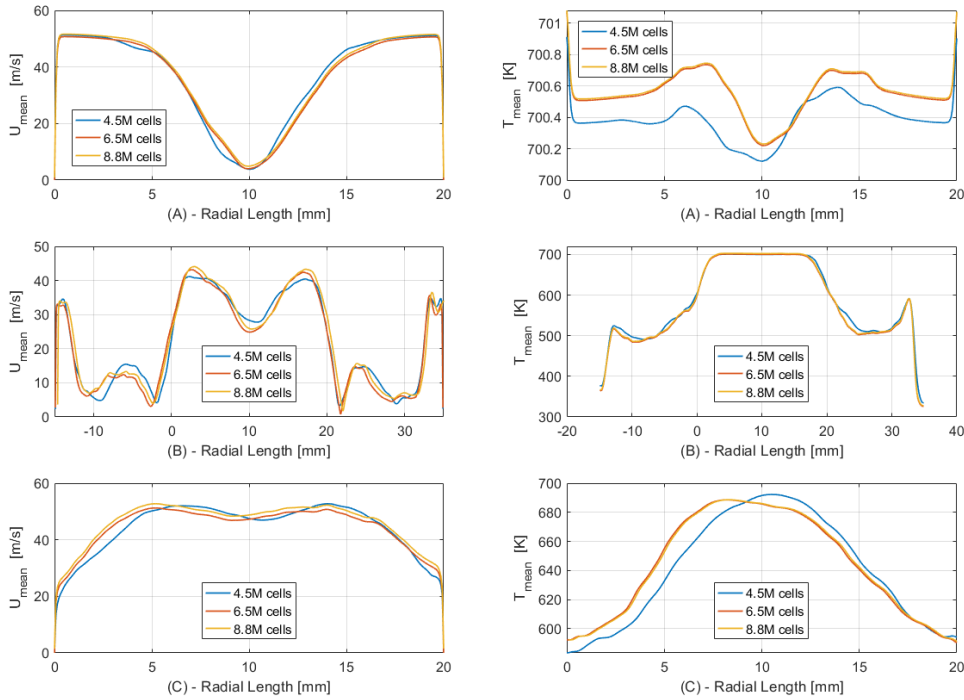


**Figure 3.5:** Results of the mesh independence study for the TVC model, comparing meshes with 4.5M, 6.5M, and 8.8M cells.

Based on the results, it was observed that the mesh with 4.5 M cells performed very well. However, for the velocity field within the cavity, indicated by symbol B, the results exhibited some additional diffusion. In contrast, the mesh with 6.5 M cells demonstrated clear mesh independence, with no significant improvement observed when additional cells were added. Consequently, the mesh with 6.5 M cells was selected for the LES simulations.

In addition to the grid size, it is equally important to assess the quality of the mesh as well, as poor mesh quality can have a significant impact on the final results. This may include a reduced convergence rate, decreased stability, and ultimately less accurate outcomes. For the selected mesh, the following quality metrics were identified and evaluated:

**Table 3.7:** Mesh quality parameters for the the selected mesh of the TVC model.

Min. Angle	Max. Skewness	Max. Cell Ratio	Max. Aspect Ratio	Max. $y^+$ Range
90°	$3.9 \times 10^{-13}$	2.12	7.03	31.75 - 96.84

Given the orthogonal nature of the physical boundaries of the TVC model, the mesh also achieved high orthogonality, as demonstrated by the minimum cell angle of 90° and a near-zero skewness value. Moreover, the maximum aspect ratio within the domain was 7.03, with a maximum volume ratio difference of 2.1 between adjacent cells. In other words, the mesh exhibited excellent quality.

Regarding the wall resolution, the maximum  $y^+$  values, which were calculated after an initial simulation, indicated that all cells were located, at most, within the logarithmic region of the boundary layer. Hence, while this positioning is reasonable near the wall, the use of wall models remained necessary in certain regions to ensure an accurate representation of the turbulent boundary layer.

Finally, the Pope criterion [51] was evaluated to ensure that a sufficient portion of the turbulent kinetic energy was resolved across the domain. Namely, this is crucial for achieving accurate results and ensuring the proper functioning of the subgrid-scale turbulence model. This is defined as follows:

$$\text{Pope Criterion: } \frac{k_{res}}{k_{res} + k_{SGS}} \geq 0.8 \quad (3.8)$$

In this equation,  $k_{res}$  denotes the resolved turbulent kinetic energy (TKE), which can be calculated from the root mean square (RMS) of the instantaneous velocity fluctuations. Similarly,  $k_{SGS}$  represents the subgrid-scale TKE, which, when using the WALE model, can be directly obtained from the turbulence model formulation, as described in the literature as follows [54]:

$$k_{SGS} = \left( \frac{\nu_{SGS}}{0.065 \cdot \Delta} \right)^2 \quad (3.9)$$

For the selected mesh, both components were computed for the cold flowfield and presented in relation to the Pope criterion, as is visualised in Figure 3.6:

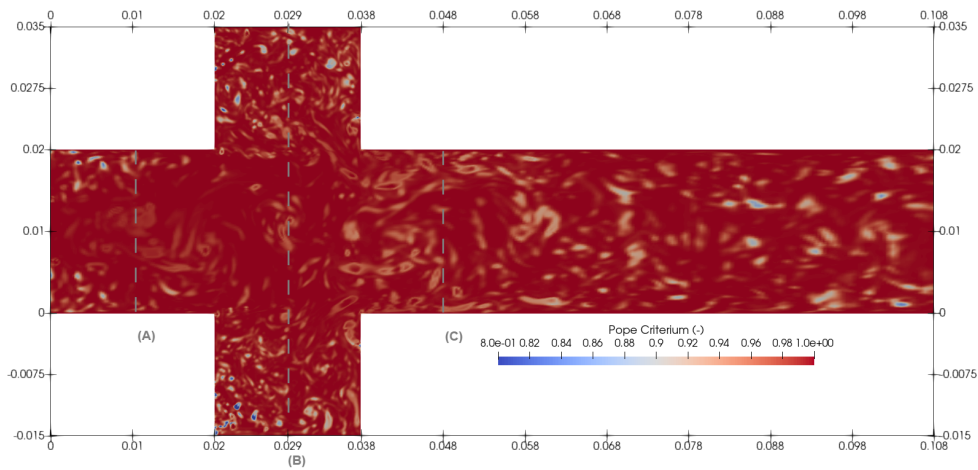


**Figure 3.6:** Pope criterion for the TVC model, including the sections considered in the mesh independence study.

As shown in the figure above, the calculated values remained consistently above 0.8 throughout the domain, with the exception of some small points close to the injection. However, this was considered not to be problematic. Thus, the adopted mesh effectively captured a sufficient range of turbulent eddies and was deemed suitable for performing the LES simulations.

### 3.3. Numerical Validation Study

Prior to the trapped vortex combustor (TVC) analysis, a validation study had to be performed to evaluate the reliability of the applied numerical method. However, due to the lack of publicly available experimental data for similar configurations, the study had to be based on existing numerical results. Namely, a quasi-DNS dataset from a prototype TVC simulation, conducted by the combustion group of the faculty of Aerospace Engineering, was chosen to perform the validation with. While this did not constitute a full validation, it allowed to benchmark the numerical method (LES) against a higher-fidelity method (DNS), and acquire a comprehensive understanding of the predictive capabilities and limitations of the custom LES solver. Nevertheless careful interpretation of the simulation results remained essential.

### 3.3.1. Validation Case

The validation model comprised a small-scale trapped vortex combustor (TVC), specifically designed to minimise computational cost. Thereby, its operation followed an ideal RQL combustion strategy, where rich premixed combustion at  $\phi_{Rich} = 1.5$  occurred in the cavity, followed by a lean premixed combustion process at  $\phi_{Lean} = 0.5$  in the downstream region. Next, in terms of configuration, a bluff-body positioned at the center of the inlet was used as flame-transfer structure. Moreover, within the cavity, besides the primary H<sub>2</sub>/air injection, a secondary air stream was introduced to enhance mixing.

A schematic diagram depicting the 2D geometry and configuration of the validation model is presented in Figure 3.7. This schematic also serves as the cross-sectional representation of the 3D model, as the geometry remained consistent along the third dimension without any variations.

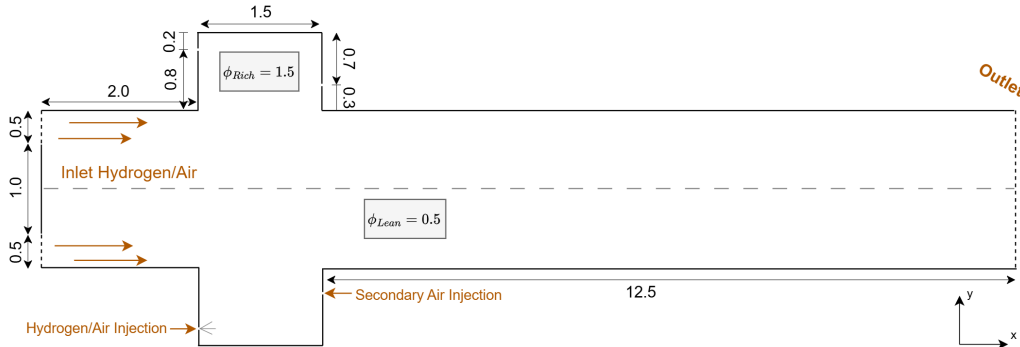


**Figure 3.7:** Schematic 2D representation of the validation model (all dimensions in mm).

The quasi-DNS results that were available for this model included instantaneous and time-averaged reactive flowfields. Thereby, these results corresponded to the simulation case in which the premixed combustible mixture entered at an uniform velocity of 150 m/s, with an inlet temperature of 850 K and a pressure of 1 atm. Hence, the case featured laminar inflow and was characterised by a Reynolds number ( $Re_D$ ) equal to 26700. Moreover, within the cavities, the streams were injected at velocities ranging from 3-16 m/s, with an uniform temperature of 300 K.

### 3.3.2. Modelling & Numerical Setup

To achieve the intended objective of the validation study, a similar LES approach as described earlier, had to be adopted when trying to replicate the flow and flame dynamics as observed in the quasi-DNS results. Therefore, the same modelling choices as detailed in subsection 3.2.4 were acquired for this simulation. Namely, this guaranteed that both simulations resolved or modelled their respective flowfields in a comparable manner.

For the discretisation of the domain, a high-quality and appropriately sized grid was carefully selected, as outlined in the following subsection. Furthermore, an initial timestep of  $1 \times 10^{-8}$  s was chosen to ensure compliance with the initial CFL condition, considering the high inlet velocity and small geometric dimensions. Moreover, timestep adjustments were dynamically applied based on a maximum CFL number of 0.5 and 0.3 for the cold and reactive flowfields, respectively.

For the other settings of the numerical setup, a similar approach as outlined in subsection 3.2.5 was adopted. However, for chemical integration, solely an implicit Euler scheme was employed instead of a Runge-Kutta scheme. This was feasible because the ignition phase could be bypassed by utilising the mean reactive flowfields of the major species obtained in the quasi-DNS data. Moreover, the similarity between configurations allowed for the use of the same boundary patches and types as in the original TVC analysis, with differences only in the numerical values. In Appendix B, an extensive overview of the numerical setup and BC's for the LES simulation of the validation model can be found.

### 3.3.3. Mesh Independence & Quality Assessment

To guarantee that all flow and flame dynamics were accurately captured and unaffected by grid-dependent effects, a mesh independence study was conducted to identify the optimal grid size for this LES simulation. For this reason, four structured meshes of respectively, 1.2 M, 2.1 M, 3.3 M, and 4.0 M cells were constructed. Subsequently, the mean velocity and mean temperature profiles of the reactive flow were analysed at three distinct axial locations, which are indicated in Figure 3.9. The final results of the independence study can be found in the figure underneath:

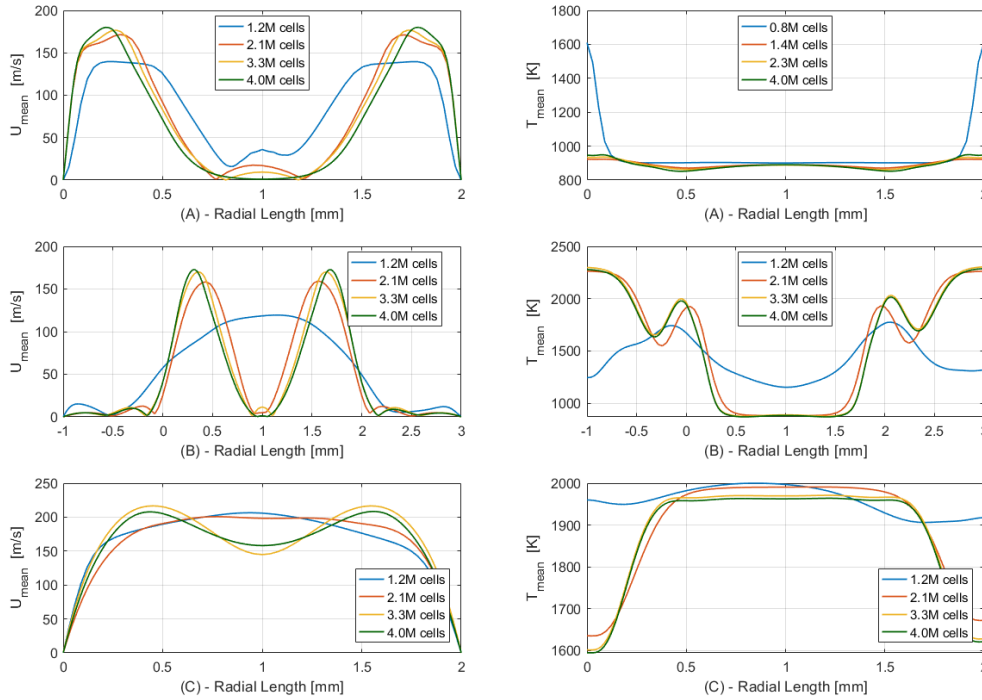


**Figure 3.8:** Results of the mesh independence study for the validation model, comparing meshes with 1.2M, 2.1M, 3.3M, and 4.0M cells.

The distinct plots clearly demonstrate that the required grid size for achieving mesh independence varied depending on both the location and the variable under consideration. However, in all cases, increasing the mesh size from 3.3 M to 4.0 M cells no longer resulted in significant improvements, indicating that mesh independence had been successfully attained. Therefore, the structured mesh with 3.3 M cells was selected for the LES simulation of the validation model.

Furthermore, to ensure a thorough and comprehensive mesh assessment, it was crucial to also evaluate the mesh quality parameters and verify compliance with the Pope criterion across the entire domain. Accordingly, the results of these assessments can be found in Table 3.8 and Figure 3.9, respectively.

**Table 3.8:** Mesh quality parameters for the the selected mesh of the validation model.

Min. Angle	Max. Skewness	Max. Cell Ratio	Max. Aspect Ratio	Max. $y^+$ Range
90°	$8.3 \times 10^{-13}$	1.94	4.15	0.86 - 1.61

As shown in Table 3.8, the mesh demonstrated excellent quality. Specifically, a very low aspect ratio was achieved, along with an uniform cell distribution, as indicated by the maximum cell ratio. Moreover, perfect orthogonality was obtained. As a consequence, numerical errors introduced by the mesh were

minimised. Furthermore, since the maximum  $y^+$ -values remained close to, or below 1, the turbulent boundary layer was properly resolved, which eliminated the need for wall functions.

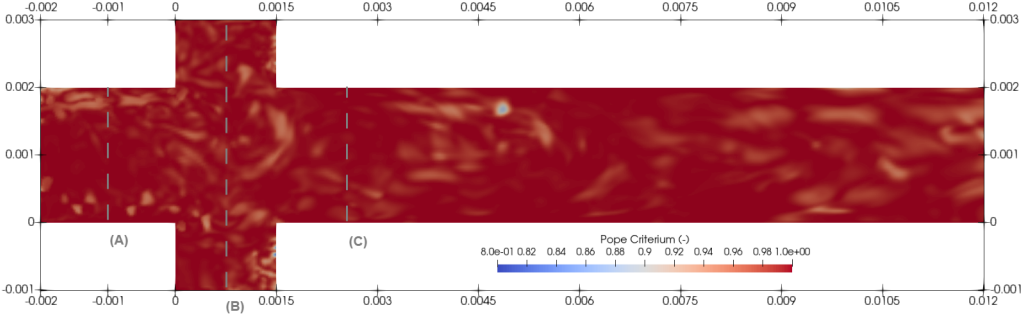


Figure 3.9: Pope criterion for the validation model, including the sections considered in the mesh independence study.

Regarding the Pope criterion of the validation model, the analysis showed that most turbulent fluctuations were resolved by the mesh rather than modelled, as illustrated by the colour map. Specifically, across a large portion of the domain, the criterion remained close to 1.0, with only the inlet and injection regions requiring more significant modelling. Consequently, the mesh was deemed suitable for conducting the LES simulation of the validation model.

# 4

## Results & Discussion

This chapter presents and discusses the results of the numerical simulations and provides the necessary insights to answer the research questions. First, in section 4.1, the hydrogen flame results obtained from the one-dimensional (1D) simulations are elaborated upon. Next, section 4.2 focuses on the validation of the applied numerical method, presenting the corresponding results and observations made. Finally, section 4.3 presents the LES results, including both the cold and reactive flowfields of the scaled-up TVC, along with the sensitivity analyses of the design variables.

### 4.1. 1D Hydrogen Flame Results

The results for the 1D simulations include an overview of the mixture temperature profiles observed in the flames studied, as a consequence of reducing hydrogen inlet temperature. Moreover, the accompanied flame characteristics are presented, and the temperature reduction effects are discussed. Finally, the impact on the reactivity itself is evaluated by determining the chemical time scales.

#### 4.1.1. Mixture Temperature

For each hydrogen flame considered — defined by its equivalence ratio — the resulting mixture temperature profile, as determined by both the initial temperatures of the reactants and the varying inlet temperature of hydrogen is uniquely defined. Since this temperature plays a crucial role in driving the combustion process, Figure 4.1 presents the results for both scenario's considered in this study.

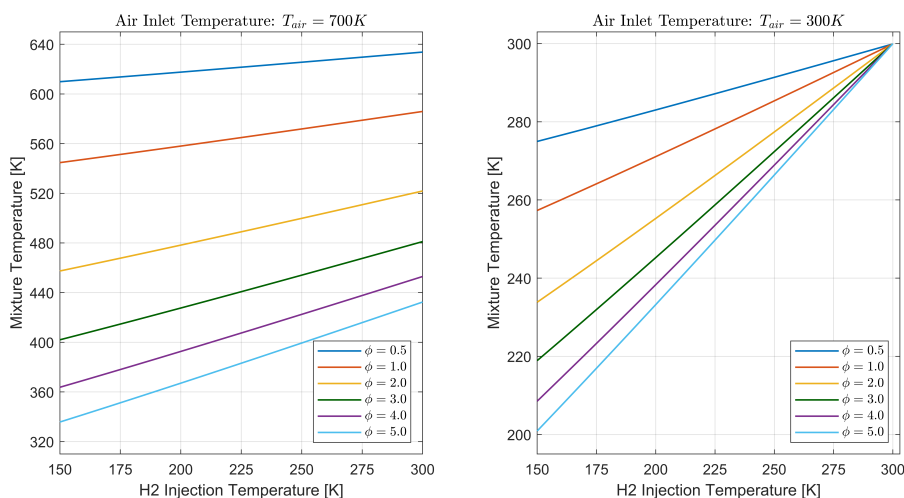


**Figure 4.1:** Mixture temperature of the reactants as a function of hydrogen's injection temperature for hydrogen flames with an equivalence ratio ranging from  $\phi = 0.5$  to 5.0.

From analysing the scenario with an air inlet temperature of 700 K, illustrated in the figure on the left, two key observations can be made. Firstly, lean and stoichiometric flames suffer from the limited amount of cold hydrogen available in the mixture. Therefore, their initial mixture temperature is significantly higher, leading to higher chemical reactivity as compared to their rich counterpart. Secondly, the temperature gradient increases with the equivalence ratio. In other words, for the same reduction in hydrogen's inlet temperature, the change in mixture temperature becomes more substantial as the equivalence ratio increases. This may suggest that the impact on chemical reactivity may be more pronounced for rich flames, as they will experience a larger mixture temperature reduction.

Moreover, it is important to recognise the challenge of achieving low mixture temperatures given a typical combustor air inlet temperature. For instance, for a high equivalence ratio of 4.0 and a hydrogen inlet temperature as low as 150 K, the resulting mixture temperature still hovers around 365 K. To address this, the air temperature can be cooled down as well, as illustrated in the second scenario on the right. In this case, the maximum mixture temperature across all flames is lowered to 300 K, which is expected to substantially slow down chemical reactivity from the start. An effect which may then be further amplified by the continued reduction of the hydrogen inlet temperature as well.

### 4.1.2. Flame Characteristics

Since the mixture composition varies within a non-premixed flame, the entire envelope of equivalence ratios must be considered when assessing the flame characteristics. Consequently, the corresponding mixture temperatures, as described above, span from 200 K to 625 K. Through selecting some representative values within this range, the complete flame behaviour can be effectively evaluated.

Given the central objective of this research — reducing chemical reactivity to mitigate the non-premixed combustion mode in the cavity, thereby ensuring low  $\text{NO}_x$  emissions — an analysis of the adiabatic flame temperature and  $\text{NO}_x$  emission index across this equivalence ratio envelope can provide additional insights. Therefore, these results are presented in Figure 4.2 and Figure 4.3, respectively.

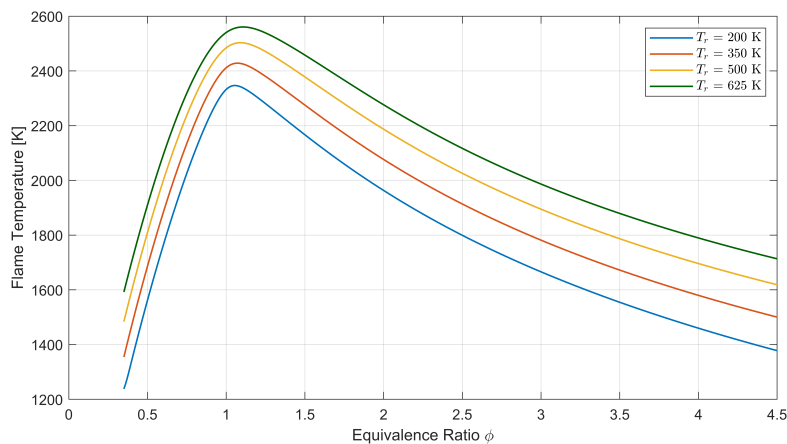


**Figure 4.2:** Adiabatic flame temperature for freely propagating hydrogen flames with an equivalence ratio ranging from  $\phi = 0.5$  to 4.5 and reactant temperatures between 200 K and 625 K.

The provided results illustrate that any decrease in reactant temperature leads to a corresponding reduction in flame temperature, which accounts for the primary diminished chemical reactivity throughout a flame. Furthermore, this figure also clearly reconfirms the rationale for mitigating non-premixed combustion in hydrogen flames. Specifically, for a wide range of conditions and equivalence ratios, from 0.5 to 2.5, the flame reaches extremely high temperatures exceeding 2000 K. This can easily lead to significant  $\text{NO}_x$  emissions, as is visualised and further quantified underneath.

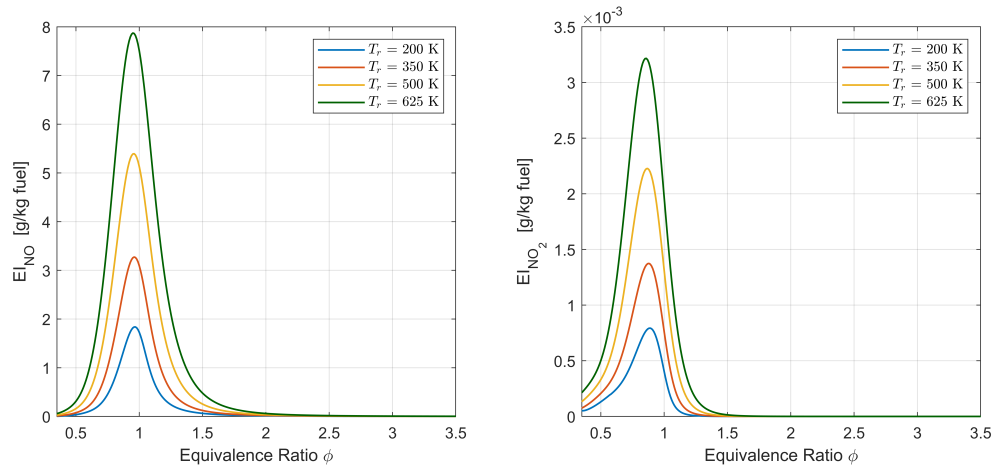


**Figure 4.3:** NO and NO<sub>2</sub> emission index for freely propagating hydrogen flames with an equivalence ratio ranging from  $\phi = 0.5$  to 3.5 and reactant temperatures between 200 K and 625 K.

The latest results present the emission index ( $EI_x$ ), defined as the amount of pollutant generated per kilogram of hydrogen consumed, for both NO and NO<sub>2</sub>. As expected, regions with high flame temperatures produce significant amounts of NO<sub>x</sub> emissions, ranging from 0.5 g to as high as 7.8 g per kg of fuel. Notably, for equivalence ratios exceeding 1.65, the emission index sharply declines to near-zero levels, despite the flame temperature remaining substantially high. This can be attributed to the limited availability of oxygen in these mixtures, which inhibit the formation of NO<sub>x</sub>.

Modifying or mitigating the non-premixed combustion mode is thus found to be the most crucial for equivalence ratio's in between 0.5 - 1.65. Namely, through significantly reducing the chemical reactivity in these regions, the mixture might move away from these conditions before the completion of the reactions, hence reducing the formation of NO<sub>x</sub>. Nevertheless, it is also important to highlight that lowering the reactant temperatures automatically leads to a substantial decrease in NO<sub>x</sub> emissions, as is illustrated in the figure. This is primarily attributed to the lower overall flame temperatures obtained, suppressing the favourable conditions.

### 4.1.3. Chemical Reactivity

In addition to the identified relationships, the precise impact of lowering hydrogen's inlet temperature on the chemical reactivity can be quantified through the calculation of the chemical time scale. In Figure 4.4 the results from the counterflow configuration under a minimal strain of  $100 \text{ s}^{-1}$  for both air inlet temperatures considered are presented. These calculations were performed using the two equations outlined in subsection 3.1.2. Although both methods reveal the same trends, a small but consistent discrepancy between the calculated values is clearly present. This is most likely due to the second method relying on the maximum reaction rate of H<sub>2</sub>O across the flame, which may overestimate the overall reaction rate, resulting in slightly shorter chemical time scales.

Independent of the mixture temperature, as illustrated in the figure on the right — where the initial mixture temperature (300 K) is constant — a large variation of reactivity is observed across the equivalence ratio's. This is primary driven by the inherent reactivity determined by the species concentrations and the corresponding flame temperature. Consequently, the chemical time scale is seen to decrease as the mixture shifts from lean to stoichiometric conditions. Furthermore, it remains on decreasing in the initial part of the rich region, owing to the high reactivity of hydrogen itself [5]. After reaching an equivalence ratio of approximately 1.5, the time scale eventually begins to increase again. In other words, the lowest chemical time scales are found in the most sensitive region towards NO<sub>x</sub> production.

When analysing the results for equivalence ratios 0.5 and 3.5, it can be seen that with an air inlet temperature of 300 K, the chemical time scale for the lean case is approximately 3–4 times longer. However, at an air inlet temperature of 700 K, both results exhibit similar time scales. This difference

arises from the varying initial temperatures when using hot inlet air. Specifically, as previously discussed, in this case the lean flame experiences a significantly higher mixture temperature (635 K) as compared to the rich flame (450 K), resulting in increased reactivity. Near stoichiometric conditions, however, this effect appears to be negligible.

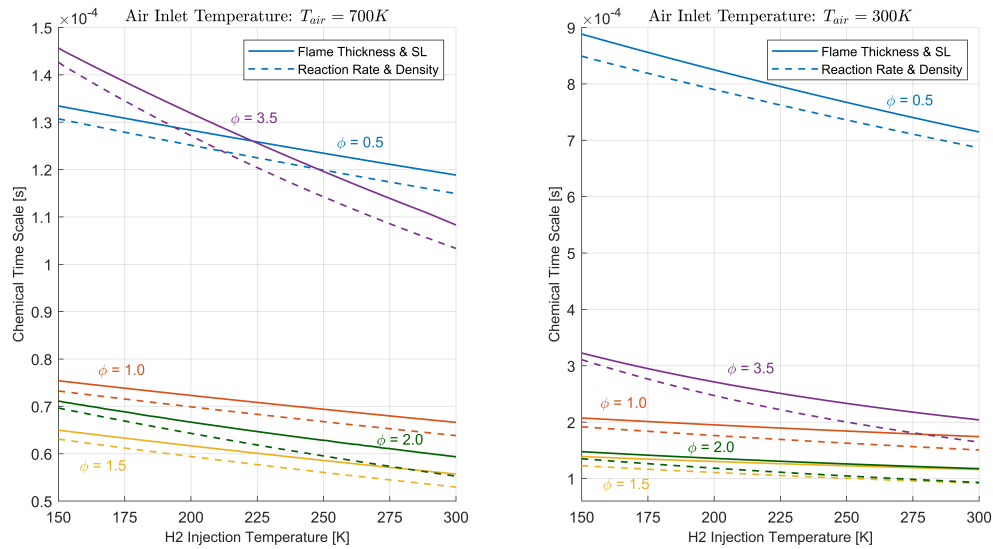


**Figure 4.4:** Variation of the chemical time scale with hydrogen's injection temperature in a reactants-to-products counterflow configuration at a strain rate of  $a = 100 \text{ s}^{-1}$ .

When analysing the numerical values, some important insights emerge as well. At first, for the common scenario where a standard combustor air inlet temperature is applied, the resulting chemical time scales are extremely short. Specifically, combustion completes within approximately 0.10 to 0.12 ms for off-stoichiometric conditions, while only 0.05 to 0.07 ms are needed when operating at or near stoichiometry, including slightly rich mixtures. Regarding the additional time that can be obtained by reducing hydrogen's inlet temperature from 300 K to 150 K, percentages vary depending on the conditions. Namely, a 13% to 19% increase is observed for equivalence ratio's close to stoichiometry. Next, a 22% time increase is found at an equivalence ratio of 2.0. Finally, closer to an equivalence ratio of 3.5, the increase rises to 35%. Thereby, this increasing trend with equivalence ratio is evident, as the mixture temperature reduction increases with higher fuel richness, as previously discussed.

In the more extreme case, where an air inlet temperature of 300 K is applied, the overall reduction in mixture temperature across all conditions leads to significantly longer chemical time scales. While the overall trends remain similar to the baseline scenario, the chemical time scales are approximately doubled in most cases, reflecting a 100% increase. The only exception is at an equivalence ratio of 0.5, where this trend does not hold due to the significant difference in initial mixture temperature, as previously discussed. Therefore, this approach can be highly effective in further extending chemical time scales when needed, particularly if lowering hydrogen's inlet temperature alone proves insufficient.

## 4.2. Results of the Numerical Validation Study

In this section, the results of the numerical validation study are presented and discussed. This is achieved by comparing the velocity contours and temperature profiles of both simulations. Next, the turbulence intensity across the combustor is plotted and evaluated. Furthermore, the turbulent flame is analysed with the use of the OH species distribution. Finally, a conclusion on the modelling capabilities and limitations of the applied numerical method is formulated.

### 4.2.1. Velocity field

In Figure 4.5, the time-averaged axial velocity component maps for both the LES results and quasi-DNS data are shown. From a qualitative perspective, both results demonstrate a quite similar flow pattern. Only in the initial part of the main flow region, a discrepancy is found. Namely, the LES results resolve a recirculation zone, as can be seen by the zero axial velocity contour line present within this figure, which is absent in the quasi-DNS data. Accordingly, slightly larger velocities are observed in this region for the latter simulation.

Further analysis into the quasi-DNS simulation revealed that this discrepancy stemmed from flaws in the bluff-body reconstruction, where the bluff body was actually not accurately modelled as a solid wall. Consequently, the recirculation bubble was absent and can thus not be considered as a validation metric. Nevertheless, it explains the presence of slightly larger velocities within this region.

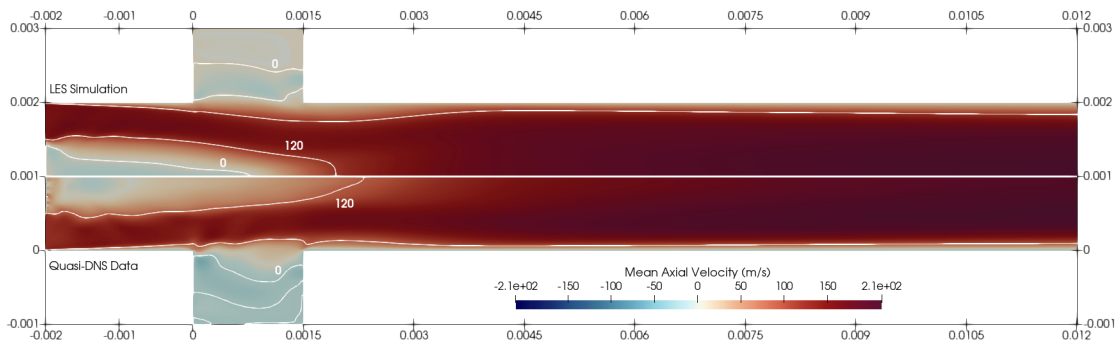


**Figure 4.5:** Time-averaged axial velocity map for the validation model, comparing LES results with quasi-DNS data.

In Figure 4.6, the velocity profiles taken at two axial locations are provided: one within the cavity at 0.75 mm and another further downstream at 2.25 mm. The results indicate similar flow behaviour within the cavity, while consistently higher velocities are observed in the main region across both profiles, likely due to the inlet flow. Nevertheless, the velocity gradients remain largely comparable, suggesting that the turbulence model adequately captures the flow dynamics.

These results also reveal a secondary discrepancy that was not immediately apparent in the velocity map. Specifically, the figure on the right shows clear differences near the main wall. This is attributed to flow spillage from the cavity, which is absent in the quasi-DNS results, leading to higher velocities in the vicinity of the wall. This phenomenon is further discussed in the following subsection

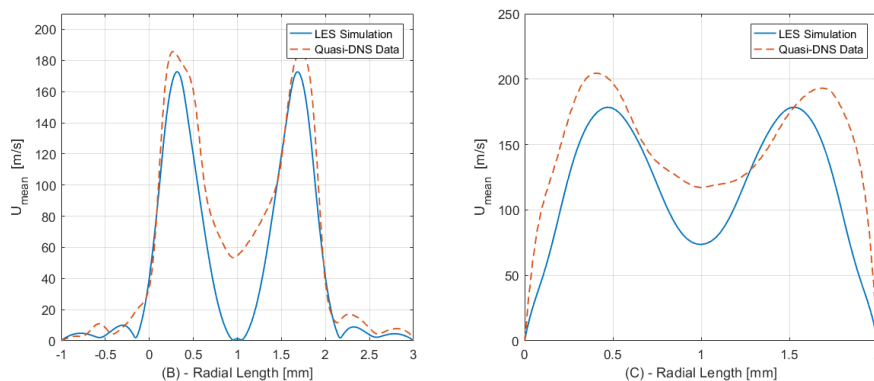


**Figure 4.6:** Comparison of time-averaged axial velocity profiles between the LES simulation and quasi-DNS data at axial locations B = 0.75 mm and C = 2.25 mm.

### 4.2.2. Temperature field

To evaluate the combined effects of flow and flame dynamics, the mean temperature field is utilised. Therefore, in Figure 4.7, the time-averaged temperature maps are presented for both the LES results and quasi-DNS data. In regions characterised by changing temperatures, both within the cavity and the main flow region, the contour lines exhibit similar lengths and shapes, indicating comparable flame development. Furthermore, while the contour lines of the quasi-DNS in the main region stretch a bit further, it is believed this to be the case because of the velocity deficit. Hence, similar overall flame behaviour is observed from a qualitative point of view.

The most notable difference observed in the LES is the cold flow spillage from the cavity, which is either absent or still developing in the quasi-DNS. Consequently, the cavity in the LES retains slightly higher temperatures. Furthermore, this observation denotes or visualises why the LES exhibit lower velocities near the main wall: it encounters a low-speed velocity originating from the cavity, rather than the high-velocity inlet flow as is the case for the quasi-DNS simulation.

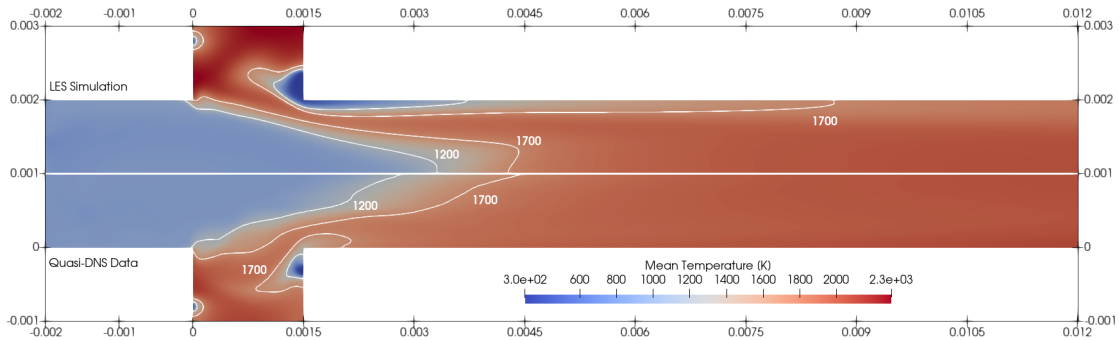


**Figure 4.7:** Time-averaged temperature field for the validation model, comparing LES simulation results with quasi-DNS data.

In Figure 4.8, the time-averaged temperature profiles at the previously introduced axial locations are presented. Specifically, one within the cavity at 0.75 mm and another further downstream at 2.25 mm. At first, the left figure shows similar temperature patterns and gradients along the radial length of the cavity, reinforcing the observation that flame dynamics are captured consistently in both simulations.

Next, the right figure confirms the absence of flow spillage in the quasi-DNS, as indicated by the higher wall temperatures. Additionally, this figure reveals an asymmetry in the quasi-DNS temperature distribution, suggesting that the flow is still developing in the region downstream of the cavity. This ongoing development introduces additional complexity in the comparison between LES and quasi-DNS.

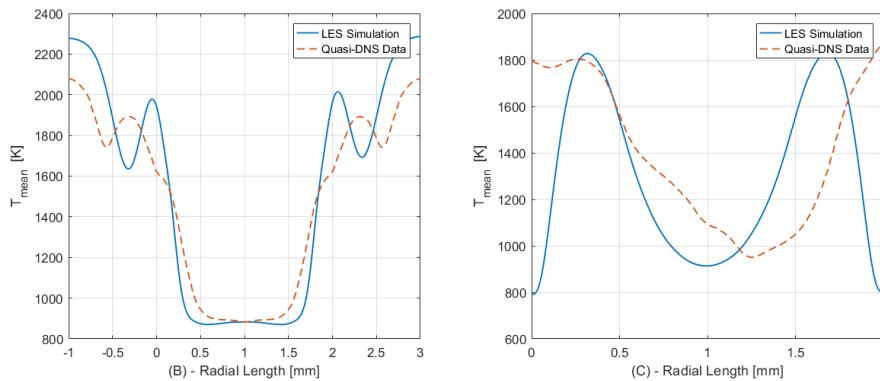


**Figure 4.8:** Comparison of time-averaged temperature profiles between the LES simulation and quasi-DNS data at axial locations B = 0.75 mm and C = 2.25 mm.

It is expected that the temperature distributions would closely align if the flow spillage around the cavity wall was resolved in a similar manner. This raises the question of whether the observed differences stem from the quasi-DNS flow not being fully developed or if they result from limitations in LES modelling capabilities or boundary layer treatment. Based on previous studies that have also reported flow spillage, the former explanation appears to be the most plausible [48] [55].

### 4.2.3. Turbulence Intensity

To assess the turbulence levels in the LES as compared to the quasi-DNS, the turbulence intensity profile is presented in Figure 4.9. This profile is obtained by normalising the turbulent fluctuations with the main inlet velocity of 150 m/s and is evaluated along the combustor's centreline.

The pronounced peak in the quasi-DNS data near the bluff-body is likely a result of the inlet flow. Next, further downstream, both profiles exhibit a similar pattern in combination with slightly lower values as for the LES. This is evident since LES models the subgrid-scale fluctuations instead of resolving them. Furthermore, the fact that both profiles exhibit similar gradients indicates that LES and quasi-DNS experience comparable levels of viscous dissipation, reinforcing the consistency between both simulations.

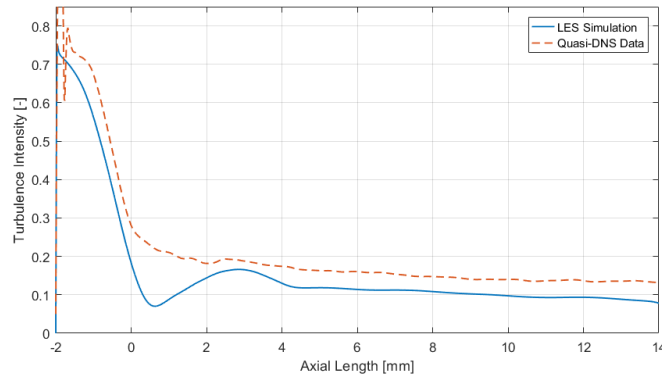


**Figure 4.9:** Turbulence intensity profile for the validation model, normalised by the main inlet velocity of 150 m/s, and taken at the centerline comparing LES simulation results with quasi-DNS data.

### 4.2.4. Turbulent Flame

When performing an LES of a combustion process, accurately capturing turbulence-chemistry interactions and modelling differential diffusion are among the most critical aspects. To validate these, it is essential to analyse both the flame front structure and detailed flame behaviour. This can be approached by first conducting a qualitative comparison of the time-averaged OH distribution from both simulations, followed by a quantitative comparison of the turbulent flame speed.

The latter element can be determined by describing the premixed flames using a progress variable based on the mass fraction of the primary combustion product,  $H_2O$ , defined as follows

$$c = \frac{\bar{Y}_{H_2O} - \bar{Y}_{H_2O,un}}{\bar{Y}_{H_2O,b} - \bar{Y}_{H_2O,un}} \quad (4.1)$$

In this equation,  $\bar{Y}_{H_2O,b}$  represents the mass fraction of water in the burned mixture, while  $\bar{Y}_{H_2O,un}$  denotes the mass fraction of water in the unburned mixture.

Using this result, a specific value for the progress variable can then be identified to quantify the flame front with. Subsequently, the turbulent flame speed can be determined along an iso-line of this progress variable by extracting the velocity component perpendicular to the flame front. Finally, the quantitative comparison between these results can be performed to evaluate the turbulence-chemistry modelling capabilities of LES as compared to the quasi-DNS.

However, the quasi-DNS flowfields which were available did not include any time-averaged species properties, rendering the intended validation strategy infeasible. As an alternative, Figure 4.10 presents the time-averaged OH distribution for the LES and the instantaneous OH distribution for the quasi-DNS, providing at least a qualitative basis for validation.

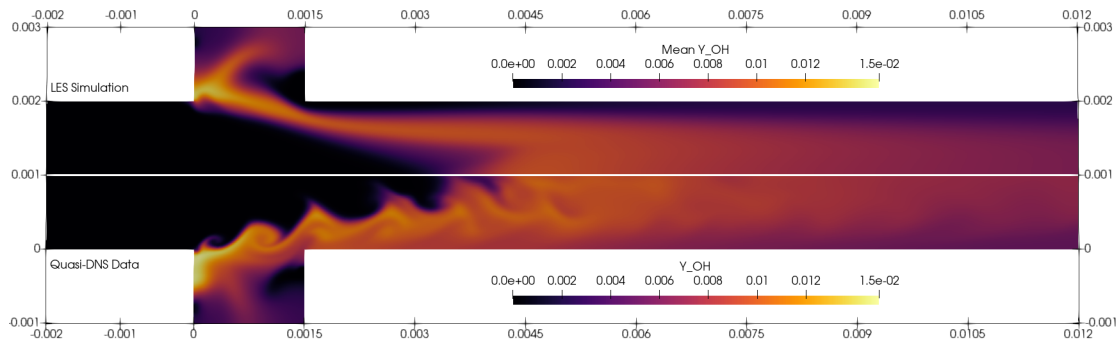


**Figure 4.10:** Time-averaged and instantaneous OH distribution for the validation model, comparing LES simulation results with quasi-DNS data.

From the simulation results provided above, two main insights can be gained into the flame dynamics. At first, both OH distributions exhibit similar peak values, indicating comparable reaction rates between LES and quasi-DNS. This suggests that the turbulence-chemistry interaction might be well captured in the LES. Secondly, the location of the OH peak aligns well between both simulations, reinforcing the idea that the flame stabilises in a similar region within the combustor.

In conclusion, the overall flow patterns between the LES results and quasi-DNS data exhibit notable similarities, with no significant differences in absolute values. Furthermore, consistent trends across the combustor are observed for both simulations. In other words, the numerical method used in the LES captures the key flow and flame dynamics within the TVC with sufficient accuracy. However, it is also important to acknowledge that a certain level of uncertainty remains with respect to the validation, given the inlet flow and the asymmetry in the results, raising concerns about the averaging period of the quasi-DNS dataset itself. Next, it is unfortunate that certain flow fields were missing further reinforcing the validation study.

## 4.3. Trapped Vortex Combustor Results

In this section, the LES results of the scaled-up TVC model are provided and evaluated. These results include, a visualisation and description of the baseline cold flow. Furthermore, the fuel-air mixing quality is evaluated and the best mixing configuration is determined. Subsequently, the corresponding reactive flow is provided and analysed in detail. Lastly, the sensitivity analysis based on the injection temperature is presented, focusing on the flame mode,  $\text{NO}_x$  emissions, and combustion efficiency, eventually enabling to assess the effect on the RQL effectiveness.

### 4.3.1. Cold Flow

The cold flow results were obtained by initialising an uniform solution within the TVC, followed by running the simulation for approximately 15 ms until a steady-state was observed, as confirmed by monitoring variables at distinct locations. Data collection then commenced, with time-averaged results obtained over the subsequent 5 ms, corresponding to about four flow-through times based on the volumetric flow rate and the volumes of the cavity and main flow region of the TVC. Consequently, the results presented below are based on these final averaged flowfields and the last simulated timestep.

To gain insight into the flow established within the trapped vortex combustor (TVC), the time-averaged velocity magnitude ( $\bar{u}$ ) colour map and streamlines are shown in Figure 4.11. Additionally, the magnitude of the velocity fluctuations ( $u'$ ) are provided in Figure 4.12, to also get a better idea of the turbulence properties. Note that the upper/lower maps represent different results as they correspond to different z-axis planes: the upper region aligns with the hydrogen injector centerline, while the lower represents the plane in between the injectors.

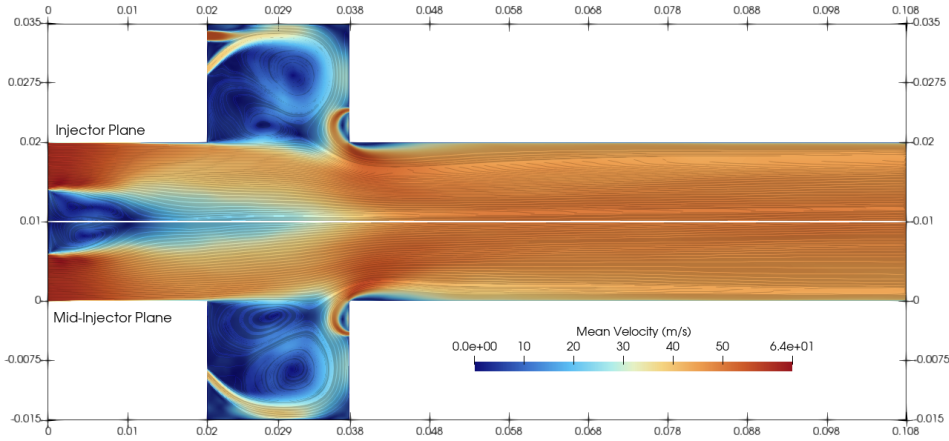


**Figure 4.11:** Time-averaged velocity magnitude ( $\bar{u}$ ) map and streamlines of the cold flow established within the baseline TVC.

The flow enters from the left at an velocity of 60 m/s and generates a recirculation zone immediately downstream of the bluff body, extending approximately  $1.2D$ . Next, further downstream, a wake is found, which retains low-velocities and persists until the flow reached about the end of the cavity. Evidently, this formation is caused by the sudden expansion and flow separation when passing the bluff-body. This, however, facilitates the entrainment of hot products into the main flow, promoting enhanced mass exchange and mixing, as desired.

Within the cavities, a dual-vortex pattern is clearly established. A large primary vortex forms deep inside the cavity, while a smaller secondary vortex develops near the interface with the main flow region. Furthermore, the airflow from the aft wall can be seen to redirect the main streamlines directly into the secondary vortex, effectively reducing flow spillage and enhancing the mixing processes within the cavity. Simultaneously, the secondary airflow itself turns into the main flow, leading to a concentrated high-velocity zone and a small recirculation zone adjacent to the cavity wall. While the cavity characteristics are discussed in more detail in the following subsection, the similarities between the streamlines of both planes already indicate that the direct presence of hydrogen does not significantly alter the overall flow structure.

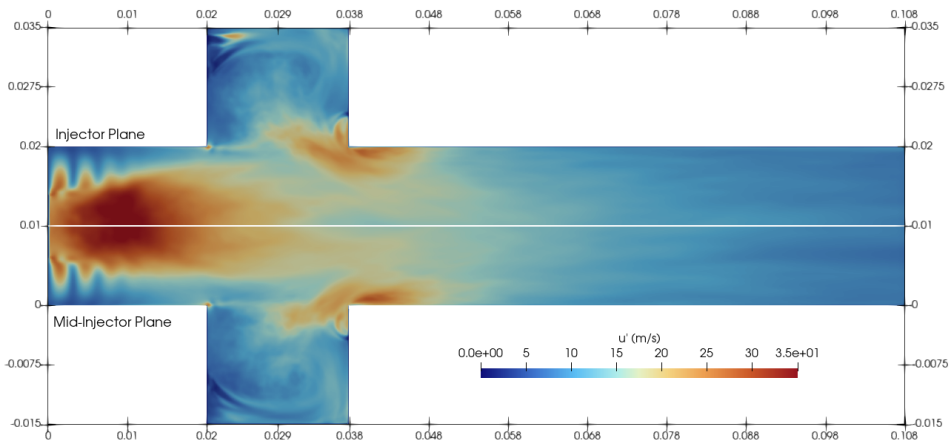


**Figure 4.12:** Turbulent velocity fluctuations (RMS) map of the cold flow established within the baseline TVC.

The velocity fluctuations, which are visualised in Figure 4.12, show a highly intense turbulence zone at the inlet of the TVC, which results from both the high inlet-velocity and unsteady flow separation. Specifically, turbulence intensities up to 60% are reached, when normalised by the main inlet velocity. Notably, a distinct undulatory turbulence pattern is observed near the main inlet, characterised by wave-like motions. This phenomenon is believed to result from the adopted turbulence generator at the inlet or another artificial effect that may have introduced this structured pattern.

As the flow progresses downstream, the turbulent region expands due to the development of shear layers between the recirculating flow and the main inlet flow, while the intensity gradually decreases due to the turbulent energy dissipation. In addition, significant turbulence is also observed at the interface between the cavities and the main flow region, particularly near the secondary air injection. This turbulence expands further downstream, enhancing the overall mixing with the main flow. Within the cavities, moderate turbulence prevails, with a localised higher-intensity zone near the reactants impingement, which is consequently absent in the mid-injector plane.

### 4.3.2. Fuel-Air Mixing Quality

To assess the fuel-air mixing quality in the cavity and identify optimal mixing for this TVC, determined by the injection angle ( $\theta_{inj}$ ), several metrics were employed to facilitate comparison and characterise the mixing process. Thereby, providing further insights into the rate and uniformity of mixing, as well as the extent to which the flow adheres to the design conditions. The results can be found below:

#### Effect on Vortical Structures:

The injection angle directly influences the vortical structures formed within the cavity, thereby impacting the overall flow and mixing properties. Therefore, the streamlines of the time-averaged velocity magnitude ( $\bar{u}$ ), taken at the injector planes are illustrated in Figure 4.13 for the injection angles considered.

While the overall impact on the dual-vortex formation remains relatively confined, some notable differences emerge. Firstly, as the injection angle increases, the streamlines are deflected further downstream, leading to greater strain. Therefore, the flow reaches the aft-wall more effectively, substantially reducing the entrapment zone, as evidenced by the smaller vortex present in the corner. Secondly, the injection angle significantly influences the position of the main vortex. Namely, while initially centered at about 47% of the cavity length, it progressively shifts up to 69% when having a  $60^\circ$  injection angle. This is also accompanied by a slight asymmetry in its overall structure. Although stability is not explicitly assessed through instantaneous field analysis, it is believed this shift to be accompanied with reduced vortex stability. Finally, the secondary vortex and flow spillage appear to be less sensitive to variations in the injection angle as the streamlines remain relatively consistent in these regions.

In this figure, it can also be noted that the primary air injection occurs at varying cavity heights. This variation arises from the decision to maintain a constant impingement location with the fuel jets while adjusting the injection angle.

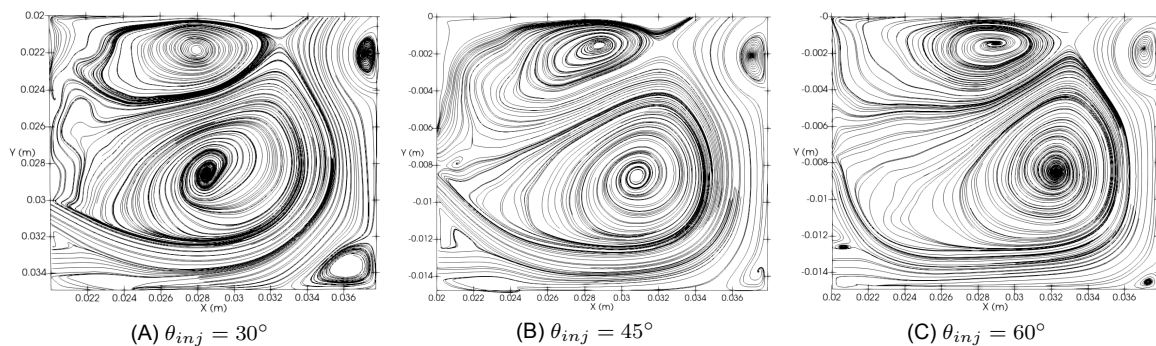


**Figure 4.13:** Streamlines and vortical structures formed within the cavity during cold flow conditions, for injection angles ranging from  $\theta_{inj} = 30^\circ$  to  $60^\circ$ .

**Turbulence & Vorticity:**

Mixing is primarily governed by turbulent fluctuations and velocity gradients in shear layers. Therefore, insights into the mixing processes can be gained by analysing results describing these phenomena. Consequently, Figure 4.14 presents the turbulence intensity, observed within the cavities for each injection angle, whereby the main inlet velocity is used as scaling variable. Additionally, to identify prominent shear layers in the flow, the vorticity distributions are visualised in Figure 4.15,

The figure below shows that turbulence and thus mixing deep within the cavity is generally present along the edges of the fuel and air jets, during impingement, and towards the aft-wall of the cavity. Furthermore, it can be seen that turbulence increases as the injection angle shifts from  $30^\circ$  to  $45^\circ$ . This is particularly noticeable at these jet boundaries and impingement region, where stronger turbulent interactions are now formed. Additionally, larger fluctuations are found further downstream and within the main recirculation zone. Hence, promoting more effective mixing in these regions. The only exception is found in the corner region, where turbulence levels remain lower, likely due to the smaller entrapped vortex. Interestingly, while an even greater increase in turbulence was expected for an injection angle of  $60^\circ$ , the results reveal a different trend. Beyond the immediate vicinity of the fuel and air inlets, turbulence levels are actually lower compared to the other two cases. This suggests that the strong impingement and compressive strain partly suppress turbulence fluctuations, leading to reduced overall turbulence. Consequently, mixing is expected to be most intense near the inlet regions, followed by a more moderate mixing process as the flow progresses.

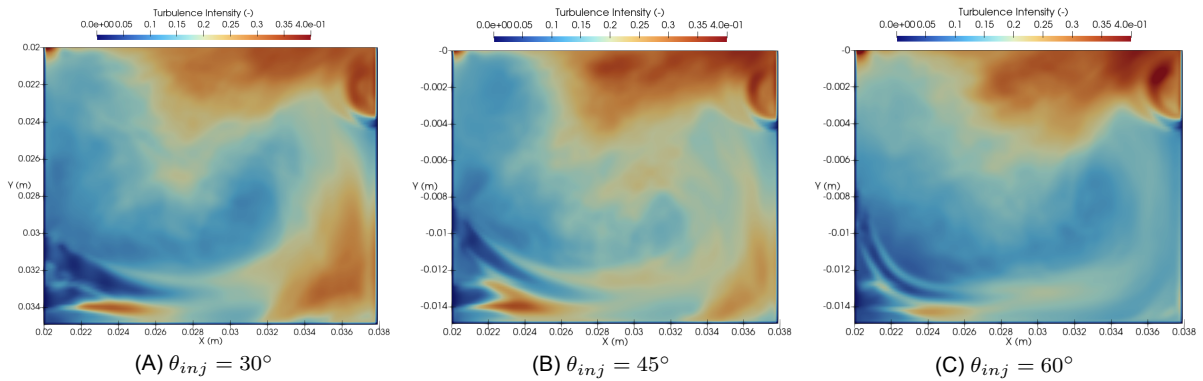


**Figure 4.14:** Turbulence intensity of the cold flow established in the cavity, for injection angles ranging from  $\theta_{inj} = 30^\circ$  to  $60^\circ$ .

With respect to the vorticity distribution, provided in the figure below, pronounced velocity gradients are evidently found at the edges of the injection jets, where shear layers are developing and fuel-air mixing occurs. Furthermore, it can be recognised that the numerical results are quite similar in all cases due to the constant injection velocities. Only for the configuration with  $60^\circ$  injection, a slightly larger concentration of vorticity is found near impingement and close to the lower wall. This aligns with expectations, given the large angle and consequently increased levels of strain.

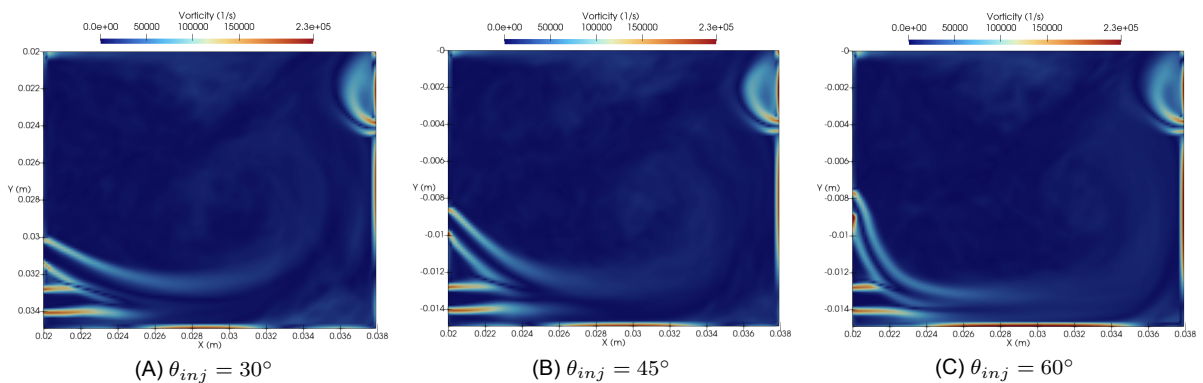


**Figure 4.15:** Vorticity of the cold flow established in the cavity, for injection angles ranging from  $\theta_{inj} = 30^\circ$  to  $60^\circ$ .

### Stoichiometric Surfaces:

Good fuel-air mixing quality requires both rapid and uniform mixing towards the design condition. Therefore, beyond analysing the factors influencing mixing, it is essential to visualise the results. This is achieved in Figure 4.16 through a colour plot of the equivalence ratio, complemented by contour lines highlighting the mixing layers and lengths.

For an injection angle of  $30^\circ$ , it can be seen that the primary reactants flow mostly parallel to each other, while observing some limited interaction as a consequence of turbulence. Therefore, the mixing rate remains low, as evidenced by the long mixing lengths. Next, although mixing continues along their interface, the streams remain largely distinguishable as they move upward in the cavity. Moreover, while the airstream is primarily entrained into the recirculation zones, hydrogen tends to spill away, complicating effective mixing. As a result, only a fraction of the flow achieves the design equivalence ratio of 3.5, while the majority exhibits significantly lower values.

Increasing the injection angle to  $45^\circ$  leads to some clear improvements. The enhanced amount of turbulence present within the flow causes the streams to mix more swiftly, which leads to shorter mixing lengths and smaller stoichiometric regions. Consequently, the mixing performance improves, and the region near the design equivalence ratio is enlarged. However, ensuring sufficient hydrogen within the recirculation zone remains challenging.

With a  $60^\circ$  injection angle, the mixing process is defined by different characteristics. Namely, while the primary airstream shows a higher mixing rate along its edges, due to strain and turbulence, the overall effect remains rather limited as indicated by mixing lengths comparable to the  $45^\circ$  case. Moreover, the fuel stream mixes less efficiently along the lower wall of the cavity, as seen in the contours at an equivalence ratio of 7.0. This is believed to be the results of the lower turbulence levels in this region. Nevertheless, the increased strain levels clearly has another effect here. The airstream is partially deflected, appearing to slide along the fuel while simultaneously pushing it downstream. As a consequence, the flow structure is unexpectedly altered in such a way that through convection and large-scale mixing, more fuel gets into the recirculation zone. Hence, the region with an equivalence ratio in between 3.0 and 3.5 is significantly enlarged, indicating improved mixing performance.

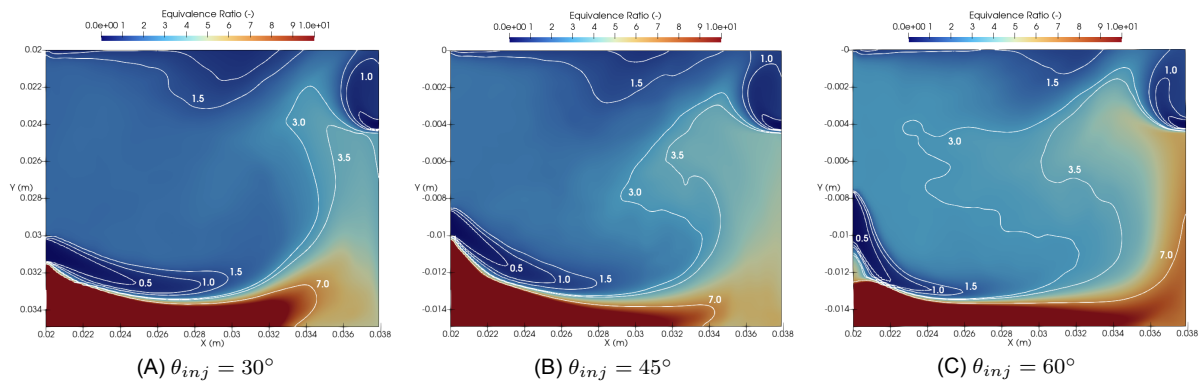


**Figure 4.16:** Time-averaged equivalence ratio, complemented with contour lines formed within the cavity during cold flow conditions, for injection angles ranging from  $\theta_{inj} = 30^\circ$  to  $60^\circ$ .

### Histogram of Equivalence Ratio:

To accurately quantify mixing uniformity and effectiveness, a histogram of the time-averaged equivalence ratio is presented in Figure 4.17 for all injection angles considered. For this calculation, the entire cavity volume is considered, excluding the streamlines of the secondary air stream that directly exits the cavity without contributing to the mixing process. Moreover, regarding the plot itself, the probabilities for equivalence ratio's higher than 7.0 are not shown in this figure to enhance plot readability.

In the plots below, it can be seen that the mean equivalence ratio remains close to the design value of 3.5, indicating proper cavity operation and design. However, for an injection angle of  $60^\circ$ , the mean value observed is slightly higher, likely due to unmixed fuel accumulating along the lower cavity wall.

Additionally, previous observations on mixing performance are reinforced here. Increasing the injection angle improves mixing effectiveness, as evidenced by the shift in the most probable equivalence ratio from 1.8 to 2.2, and eventually to 3.0. Moreover, the enhanced mixing uniformity is also reflected in the reduced value for standard deviation, as depicted above the plots, when the injection angle is increased. However, it is clear that further optimisation is absolutely necessary to achieve a more uniform and well-mixed flow within the cavity, ensuring a situation that aligns with the design conditions.

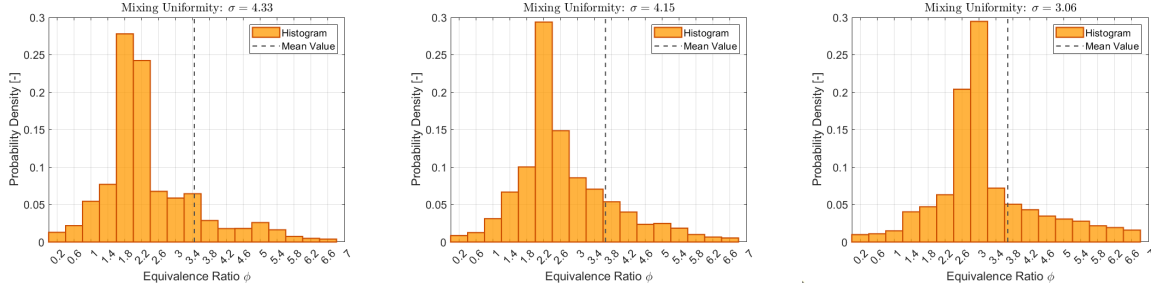


**Figure 4.17:** Histogram based on the equivalence ratios found in the cavity, for injection angles ranging from  $\theta_{inj} = 30^\circ$  to  $60^\circ$ .

### Effect on Mixing in Main Region:

Although not the primary focus of this study, the mixing conditions at the combustor outlet, represented by the equivalence ratio, are shown in Figure 4.18 for the injection angles considered in this analysis.

From the results, two observations can be made. First, while the TVC is designed to operate at an equivalence ratio of 0.4 in the lean region, a clear imbalance is established with higher equivalence ratios near the walls and lower-than-desired values at the centre. This suggests that mixing in the lean region is insufficient and should be enhanced through more advanced mixing structures. Secondly, as the injection angle influences the flow structure at the interface between the cavity and the main region, the performance in the lean region is slightly altered as well. Thereby, it can be seen that the configuration with an  $60^\circ$  injection angle demonstrated the closest match to the design target.

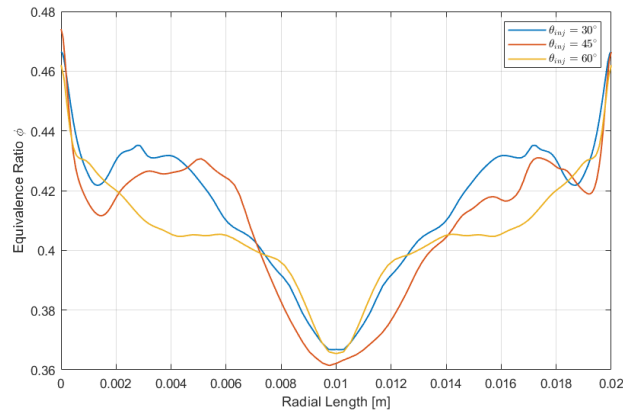


**Figure 4.18:** Equivalence ratio profiles at the outlet of the TVC, for injection angles ranging from  $\theta_{inj} = 30^\circ$  to  $60^\circ$ .

This analysis highlights the complexity of achieving effective mixing within the cavity, as it is influenced by multiple interdependent factors. In particular, for the injection angle alone, the level of turbulence, vorticity, and macroscopic mixing through convection are altered, eventually all affecting the mixing performance. Furthermore, within the scope of this study, the best fuel-air mixing quality was observed for a  $60^\circ$  injection angle, making it the most suitable configuration for evaluating the impact on temperature within the reactive flow. However, this does not necessarily represent the optimal condition, as further improvements may be possible with larger injection angles. Due to time constraints, this aspect was, however, not further investigated.

### 4.3.3. Reactive Flow

To initiate combustion within the TVC configured with a  $60^\circ$  injection angle, a heat source was applied to the cavities. The simulation then proceeded for approximately 10 ms until a steady-state condition was achieved, as confirmed by monitoring data at various locations. Following this, data collection commenced, with time-averaged results obtained over the subsequent 4 ms. This duration corresponds to roughly four flow-through times, calculated based on the volumetric flow rate and the volumes of the cavity and main flow region of the TVC. Based on these final averaged flowfields and the last simulated timestep, the reactive flow and flame dynamics can be characterised as follows:

#### Velocity Field & Streamlines:

To evaluate the impact of heat release on the overall flowfield, the time-averaged velocity magnitude ( $\bar{u}$ ) map along with the corresponding streamlines is shown in Figure 4.19. Note that the upper/lower maps represent different results as they correspond to different planes along the z-axis.

Compared to the cold flow, the vortical structures settled in the cavities are altered notably. The clear impingement of reactants is no longer observed. Instead, the main vortex is displaced upstream, primarily interacting with the incoming air stream, while a substantial portion of the hydrogen flow tends to spill away. Additionally, the secondary vortex fails to develop properly. This behaviour can most likely be attributed to the substantial flow expansion caused by combustion, moving the gases outward. On the contrary, with respect to the main flow region, the flow pattern remains largely consistent besides the significantly higher velocities, reaching up to 150 m/s due to the reduction in density.

Finally, this overall flow behaviour is observed in both the injector plane and the mid-injector plane, indicating that the presence/absence of hydrogen through the injection holes has a negligible influence on the reactive velocity field.

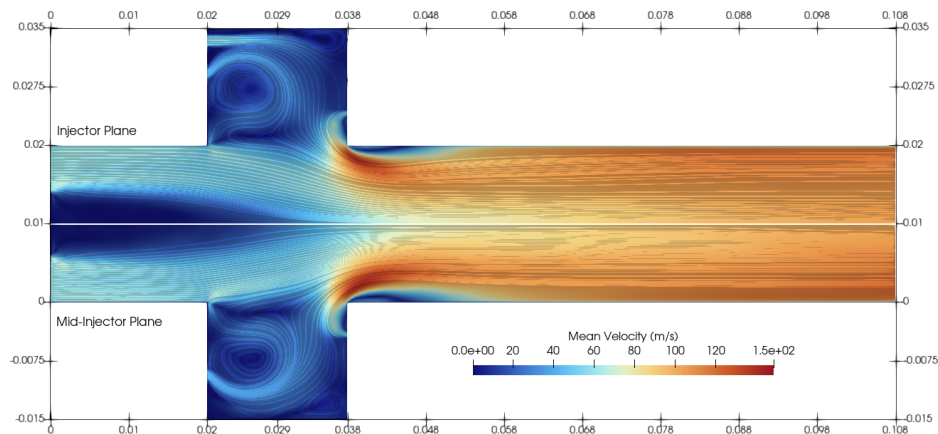


**Figure 4.19:** Time-averaged velocity magnitude ( $\bar{u}$ ) map and streamlines of the reactive flow established in the TVC.

#### Temperature Field:

To get a better understanding of the overall combustion process going on within the TVC, the time-averaged temperature ( $\bar{T}$ ) map along with selected mixture fraction iso-lines is presented in Figure 4.20. Specifically, the stoichiometric mixture fraction contour line,  $Z = 0.028$  is highlighted in white. In addition contour lines representing mixture fractions near the lean flammability limit ( $Z = 0.0042$ ) and the rich flammability limit ( $Z = 0.168$ ) are highlighted in black.

Based on the results shown below, it is inherent that the black contour lines, which indicate the region in which a combustible mixture is present, also largely coincide or denote the boundaries between the cold and the hot (reactive) flow present within the TVC, as evidenced in the temperature map. Furthermore, throughout both the cavity and the first half of the main flow region, a stoichiometric mixture line is clearly present, suggesting a non-premixed combustion mode. Only from the second half of the main flow region, the combustible mixture progressively transitions into a fully fuel-lean regime.

Furthermore, three characteristic regions can be identified based on these results. First, (1) combustion initiates at the interface between the injection streams, where the reacting flow begins to develop. Thereby, a portion of the hot products becomes entrapped into the main vortex, acting as a continuous ignition source and contributing to flame stabilisation. Second, (2) this stream of hot products interacts further downstream with hydrogen that is able to reach the aft-wall, near the secondary airstream. This interaction leads to the formation of a secondary high-temperature region, where additional combustion occurs. Finally, (3) along the walls of the main combustor region, a third notable region emerges, where combustion continues alongside mixing with the incoming airflow. However, as previously observed in the cold flow, insufficient mixing is evident in the main region, as indicated by the significant non-uniformity in the temperature profile at the TVC outlet.

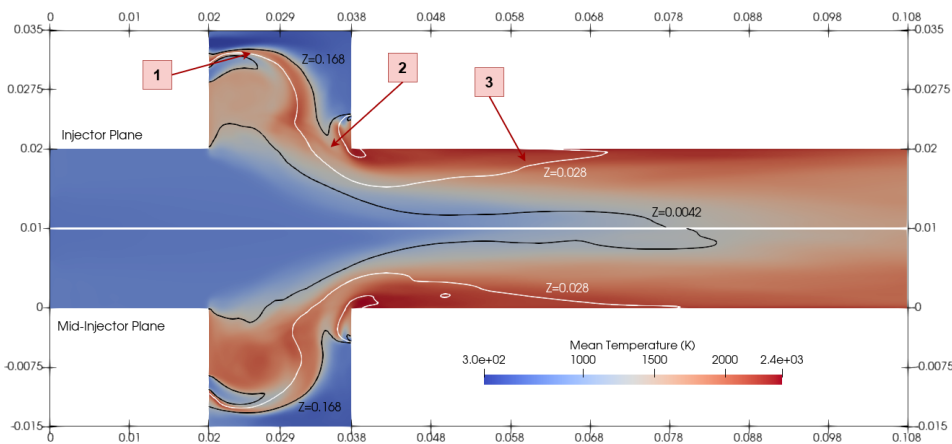


**Figure 4.20:** Time-averaged temperature ( $\bar{T}$ ) of the reactive flow established in the baseline TVC. The stoichiometric contour ( $Z = 0.028$ ) is highlighted in white, while contours near the lean ( $Z = 0.0042$ ) and rich ( $Z = 0.168$ ) flammability limits are shown in red. Zones 1–3 indicate characteristic regions used to describe the combustion process.

### Species Distribution:

The composition of the reacting mixture can be characterised using the time-averaged distributions of the major species ( $\bar{Y}_c$ ). Figure 4.21 illustrates the distribution of the fuel ( $H_2$ ), while Figure 4.22 depicts the oxidiser ( $O_2$ ). Lastly, the primary combustion product,  $H_2O$ , is shown in Figure 4.23.

The distributions presented below provide a complementary view of the combustion process. Within the cavities,  $H_2$  and  $O_2$  are consumed at the interface or mixing layer between the two streams. However, a significant amount of hydrogen persists near the aft-wall of the cavity, while oxygen is still clearly present within the main vortex. This aligns with expectations from the velocity field, confirming that mixing remains significantly limited in the reactive flow. Next, further downstream but before exiting the cavity (zone 2), the hydrogen fully consumes the available oxygen from the secondary airstream, creating a zero  $O_2$  concentration region. Beyond this point, the remaining hydrogen and hot combustion products enter the main flow region, where gradual diffusion with  $O_2$  occurs. Hence, since this region is predominantly characterised by species diffusion, it suggests slow mixing combined with mixing-limited, non-premixed combustion. Therefore, even within the fully fuel-lean region introduced earlier, the combustion process seems to be governed by non-premixed behaviour.

Note that quantifying this remaining amount of hydrogen that enters the main combustor region is challenging when based solely on the  $H_2$  distribution. Specifically, as the amount of combustion products increases continuously, the relative contribution of hydrogen is reduced, which complicates this assessment. However, as determined earlier, the stoichiometric mixture fraction contour line is only observed halfway downstream of the main region, which confirms that a significant amount of hydrogen is indeed still present within the mixture.

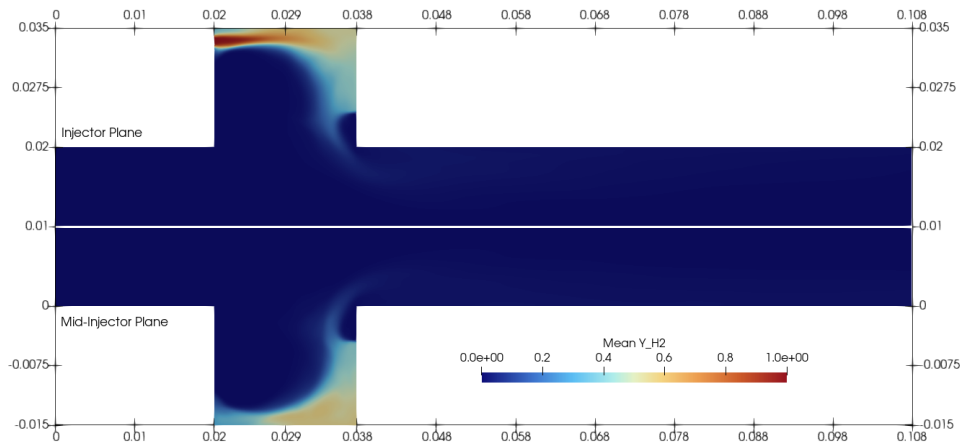


**Figure 4.21:** Time-averaged distribution of  $H_2$  of the reactive flow established in the TVC.

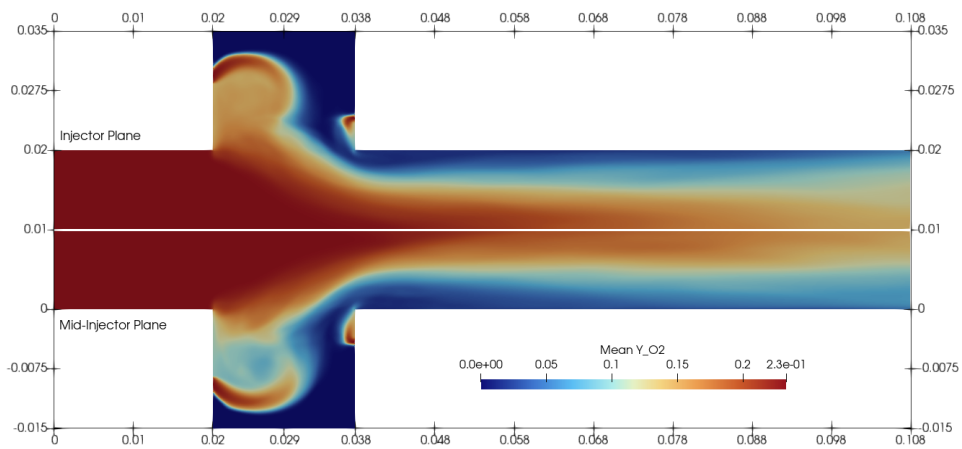


**Figure 4.22:** Time-averaged distribution of  $O_2$  of the reactive flow established in the baseline TVC.

The results for  $H_2O$ , presented in Figure 4.23, further reinforce the previous observations.  $H_2O$  is primarily produced at the interface between the main injectors and near the secondary injection zone before being convected out of the cavity. In the main combustion region, the  $H_2O$  distribution is predominantly shaped by diffusion towards the combustor's centerline, suggesting ongoing but mixing-limited combustion, characteristic of non-premixed combustion behaviour.

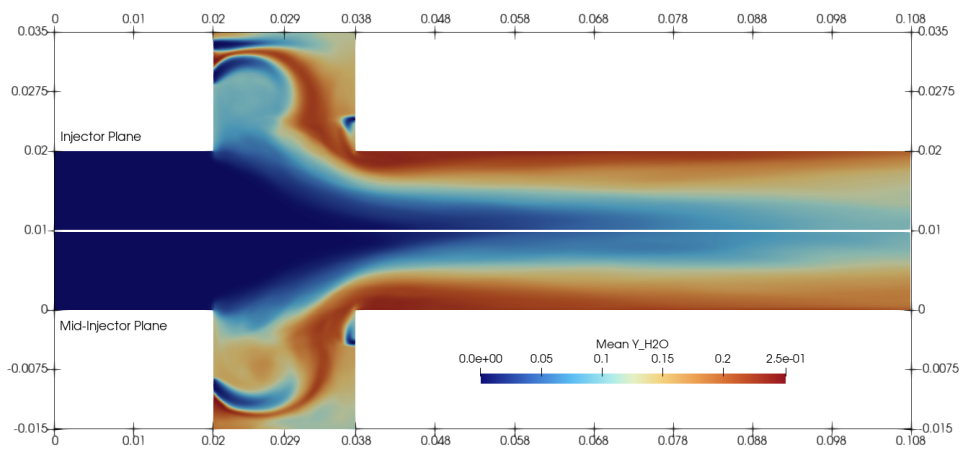


**Figure 4.23:** Time-averaged distribution of  $H_2O$  of the reactive flow established in the TVC.

### Flame Front & Flame Index:

In addition to the major species, distributions of minor species, with in particular OH are crucial for accurately defining the flame dynamics and locating the flame front. Namely, OH predominantly forms within the reaction zones, where it reaches its maximum concentration and acts as a key intermediate species in  $H_2$ /air combustion. Additionally, the flame index can be employed to quantify the predominant combustion mode present within the TVC, distinguishing between non-premixed and premixed regimes. According to Yamashita et al. [56] (1996), this flame index is defined as follows:

$$G_{FI} = \frac{\nabla Y_{H_2} \cdot \nabla Y_{O_2}}{|\nabla Y_{H_2}| |\nabla Y_{O_2}|} \quad (4.2)$$

In other words, the Flame Index ( $G_{FI}$ ) is determined by the inner product of the fuel and oxidizer gradients, normalised by their respective magnitudes. When both gradients point in the same direction and are aligned, the mixture is considered well-mixed, indicating premixed combustion, with a corresponding value of 1. Conversely, if the gradients are aligned but point in opposing directions, this suggests non-premixed combustion, corresponding to a value of -1. Values close to zero may indicate either a mixed combustion mode or that at least one of the gradients considered is negligible.

The time-averaged distribution of the OH species is presented in Figure 4.24 with the contour line of the stoichiometric mixture fraction ( $Z = 0.028$ ) included as further reference. The result confirm earlier observations, showing that the primary reaction zone within the cavity is located at the interface or mixing layer between the injection streams, where a stable C-shaped flame is clearly distinguishable. Further downstream this flame then starts to expand in the axial direction as it approaches the interface with the main region. Additionally, the presence of OH within the main vortex indicates ongoing combustion in this region, which was not immediately apparent from previous results. This specifies that, alongside combustion products, hydrogen is entrapped within the main vortex due to convection or preferential diffusion, leading to sustained combustion and acting as a continuous ignition source. Finally, a smaller flame also forms at the aft-wall of the cavity in the vicinity of the secondary air injection before merging with the main flame.

The OH distribution further specifies the combustion process within the main region. A long, continuous reaction zone or flame front is observed, which expands gradually towards the combustor's centerline. While the high flow velocity rapidly convects species downstream, this alone does not fully explain the observed flame behaviour. Instead, it suggests a mixing-limited but continuous combustion process, driven by the rate at which reactants and hot products mix with the incoming airflow. Notably, OH is also present very close to the wall, describing the presence of a flame attached to the wall. This is possible because the simulation assumes perfectly insulated, adiabatic walls, preventing heat loss and allowing the flame to persist. However, in reality, significant heat transfer towards the walls would lead to flame quenching in these near-wall regions.

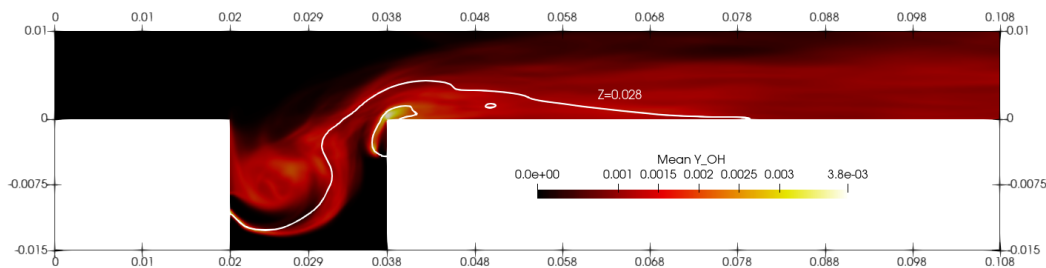


**Figure 4.24:** Time-averaged distribution of OH of the reactive flow established in the TVC, , with the stoichiometric mixture fraction ( $\bar{Z} = 0.028$ ) highlighted in white.

In Figure 4.25 the flame index can be found, with the contour line of the stoichiometric mixture fraction ( $Z = 0.028$ ) included as further reference. The results align well with the OH distribution and further indicate that combustion in the cavity is predominantly non-premixed, as evidenced by the prevalence of

flame index values of -1. This should not be a surprise given that the stoichiometric line coincides with the c-shaped flame. However, within the main vortex, both non-premixed and premixed combustion seems to occur, indicating that the main vortex induces intense mixing within this region. Furthermore, for the secondary smaller flame near the aft-wall of the cavity, the combustion characteristics differ as well. Here, mixing is significantly more intense, leading to a transition toward premixed combustion, as reflected in the flame index.

While flow separation around the corner of the cavity induces some additional premixed combustion, the other part of the main combustion region remains predominantly non-premixed. Furthermore, the fact that most of this region exhibits flame index values significantly different from zero reinforces the presence of a continuous mixing-limited combustion process.

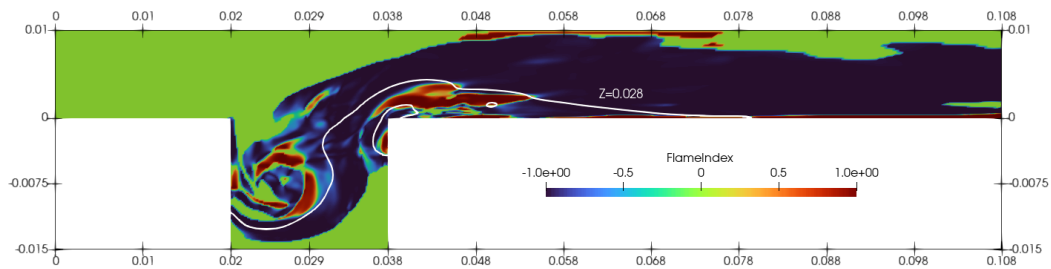


**Figure 4.25:** Time-averaged Flame Index of the reactive flow established in the TVC, with the stoichiometric mixture fraction ( $Z = 0.028$ ) highlighted in white.

This analysis clearly demonstrates that the reactive flow differs significantly from the previously identified ideal cold flow. The combustion process and associated heat release have a substantial impact on the flow dynamics. Additionally, the high reactivity results in a primarily non-premixed combustion mode, with some exceptions observed in both the cavity and main flow region. Therefore, improvements are necessary in both regions, with a strategy for the cavity already being discussed in the following subsection. To overcome limitations in the main flow region, it is evident that a more complex mixing structure, such as incorporating radial struts or multi-orifice plates is required to enhance mixing and mitigate the current slow, mixing-limited combustion process.

#### 4.3.4. Sensitivity Analysis of $H_2$ Injection Temperature

To address the non-premixed combustion performance within the cavity, and by extension within the TVC, this study identified hydrogen's injection temperature ( $T_{H_2}$ ) as a potentially key variable for improvement. Therefore, this subsection examines the impact of reducing  $T_{H_2}$  from 300 K to 150 K on the reactive flowfields and evaluates the resulting trends with respect to the effectiveness of the RQL combustion process. Below, the results of this sensitivity analysis can be found:

##### **Flame Intensity:**

As was established in the 1D simulations, outlined in section 4.1, reducing the reactant temperature notably lowered chemical reactivity. Extending this analysis to the cavity of the detailed simulations (LES), the impact of temperature on flame intensity or thus reactivity can be assessed by comparing the time-averaged heat release maps and the time-averaged OH species distributions. However, since heat release (averaged) was not directly computed in these simulations, Figure 4.26 presents only the OH species distribution maps for both injection temperatures.

The results provided below show that both flames maintain a similar overall contour, although the flame at the lower injection temperature appears slightly more dispersed. Furthermore, instead of forming a coherent reaction zone, this flame develops more into multiple thin, closely packed layers. This suggests that ignition or combustion is delayed, and the flame becomes more sensitive to local flow conditions. Finally and most importantly, under all circumstances the OH intensity, providing a qualitative indication of the reactivity is consistently reduced throughout the entire cavity when the injection temperature is reduced, confirming what was found earlier.

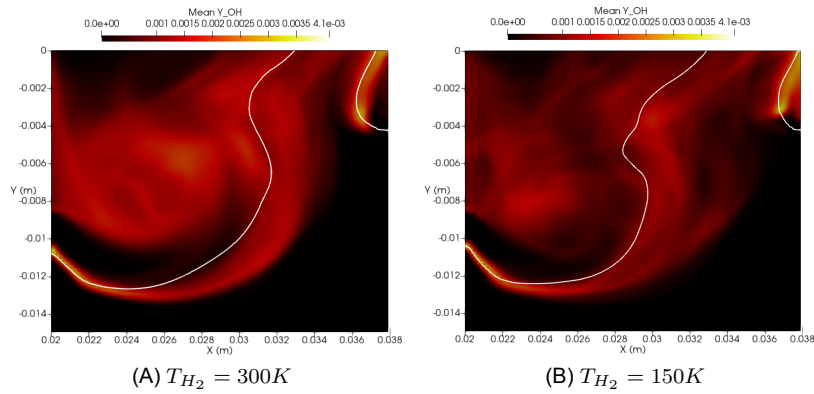


**Figure 4.26:** Time-averaged distribution of OH within the cavity of the reactive flow, comparing results with hydrogen injection at 300 K and 150 K. The stoichiometric mixture fraction ( $Z = 0.028$ ) is highlighted in white.

### Scatter Plot of Temperature:

To assess whether the reduced reactivity significantly impacts the combustion regime, a scatter plot of instantaneous temperature as a function of mixture fraction ( $Z$ ) is presented in Figure 4.27, using data from the final simulated timestep. With respect to the temperature values on the y-axis, a normalisation based on the maximum temperature found within the cavity is applied to filter out variations resulting from the lowered injection temperature itself, enabling a direct comparison between the two scenarios. Moreover, the blue line denotes the conditional mean across selected mixture fractions

While both scatter plots display the characteristic triangular shape, an irregularity can be observed. Namely, the highest temperatures occur at a mixture fraction of approximately 0.017, which is significantly leaner than the calculated stoichiometric mixture fraction where peak temperatures were expected. This deviation is most likely due to the presence of hot products within the recirculation zone of the cavity, which dilute the mixture and lead to an apparent shift or oddly calculated stoichiometric point. Furthermore, a notable number of data points show temperatures exceeding the adiabatic flame temperature. This can be attributed to the preferential diffusion of hydrogen, resulting in locally enriched regions with elevated temperatures.

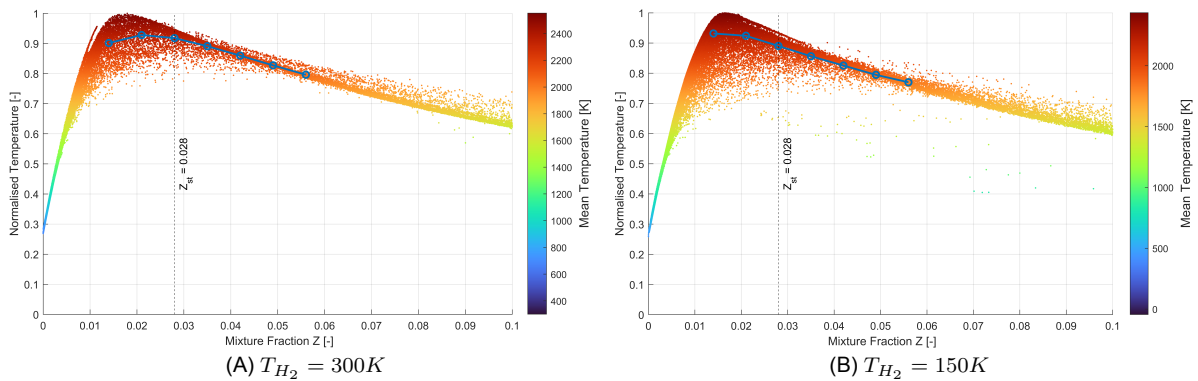


**Figure 4.27:** Scatter plot of temperature in the cavity at the latest timestep for injection temperatures of 300 K and 150 K. The stoichiometric mixture fraction ( $Z = 0.028$ ) is shown as a dotted line, while the blue line represents the conditional mean.

Apart from this, these plots also offer valuable insights into the combustion regimes observed within the cavity for both scenario's. Specifically, in both cases, combustion is observed across the entire range of mixture fractions, with most data points clustered together near the adiabatic flame temperature. This indicates complete combustion across the complete mixture spectrum and reconfirms the presence of primarily non-premixed combustion regimes. Thus, reducing hydrogen's injection temperature from 300 K to 150 K is found to be insufficient to completely resolve or eliminate non-premixed combustion. However, this does not imply that the flame mode is unaffected by the temperature reduction. To better

understand these changes, attention must be given to data points falling below the adiabatic flame temperature curve, as they suggest regions of partially premixed combustion or incomplete combustion, where mixing limitations or local quenching may be influencing the reaction process.

Moving away from non-premixed conditions typically manifests as data points shifting downstream, away from the characteristic flame temperature, thereby resulting in a lower conditional mean temperature. Moreover, points would move away from stoichiometric conditions toward the intended design conditions. When comparing the two scatter plots, it is evident that, near the maximum temperature conditions and stoichiometric conditions, data points exhibit a wider spread and attain lower temperatures when the hydrogen injection temperature is reduced to 150 K. Accordingly, the conditional mean line also shows slight changes, for example at the stoichiometric mixture fraction, the mean temperature decreases by approximately 4%. This demonstrates that the reduced reactivity allows more time for mixing, leading to a slight reduction in non-premixed combustion behaviour. However, considering an absolute injection temperature reduction of 150 K, the overall influence on the combustion mode remains limited. In other words, the injection temperature shows a present but low sensitivity towards altering the established combustion mode performance.

### NO<sub>x</sub> Emissions:

The primary motivation for mitigating non-premixed combustion behaviour is to reduce the formation of high-temperature regions, which are susceptible to intense NO<sub>x</sub> production. With respect to the injection temperature, the minor reduction in non-premixed combustion, as determined above will result in a slight decrease in the reaction rate of these pollutants. Nevertheless, a more significant reduction in NO<sub>x</sub> production is anticipated due to the overall lower flame temperatures within the cavity, regardless of the combustion mode. To illustrate and quantify this, the time-averaged distributions of the species N<sub>2</sub>O and NO are presented in Figure 4.28 and Figure 4.29, respectively.

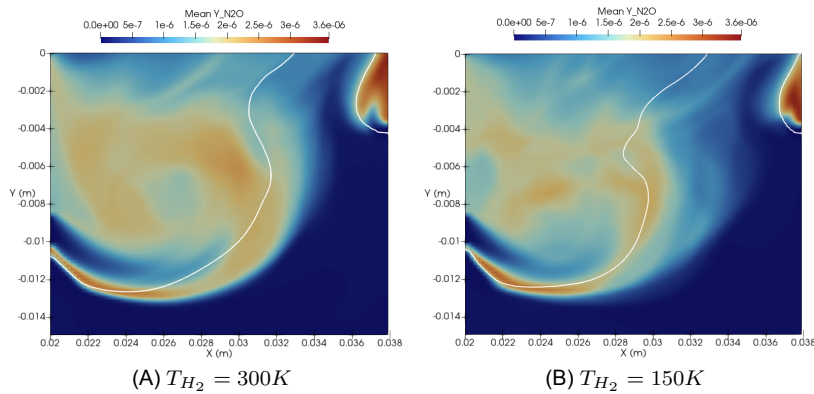


**Figure 4.28:** Time-averaged N<sub>2</sub>O distribution within the cavity of the reactive flow, comparing results with hydrogen injection at 300 K and 150 K. The stoichiometric mixture fraction ( $Z = 0.028$ ) is highlighted in white.

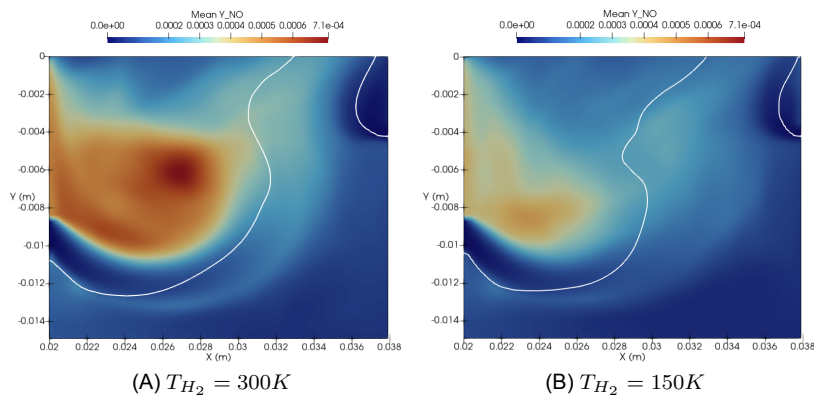


**Figure 4.29:** Time-averaged NO distribution within the cavity of the reactive flow, comparing results with hydrogen injection at 300 K and 150 K. The stoichiometric mixture fraction ( $Z = 0.028$ ) is highlighted in white.

Firstly, it is important to note that  $N_2O$  is not a primary pollutant but rather an intermediate species or precursor to the formation of pollutants such as  $NO$  and  $NO_2$ . This distinction is reflected in the presented distributions. Specifically, the  $N_2O$  concentration exhibits a broader spatial spread and reaches its peak intensity earlier in the flow, originating from the injection streams, in contrast to the more delayed distribution observed for  $NO$ . Furthermore, regarding  $NO$  itself, it can be observed that the distribution pattern closely resembles that of the  $OH$  species. This is evident, given that the flame front corresponds to the reactive zone, which is characterised by high flame temperatures and thus high production rates of  $NO_x$ . Additionally, a notable accumulation of  $NO$  is observed within the main vortex, where it appears to be entrapped more significantly than in other regions of the cavity. This might suggest that the vortex dynamics play a role in the retention of  $NO$  concentrations.

Furthermore, reducing hydrogen's injection temperature leads to a notable decrease in  $NO_x$  emissions, as evidenced by the reduced intensity in the colour plots, thereby confirming the earlier speculations. However, these visual results do not provide insight into the absolute reduction in  $NO$  mass, which is expected to be lowered progressively downstream. To quantify this, the emission index of  $NO$  ( $EI_{NO}$ ), defined as the amount of  $NO$  produced per kilogram of hydrogen consumed is calculated at the interface between the cavity and the main flow region as well as at the combustor outlet. Thereby, to ensure consistency and allow for a comparison, a 15% oxygen normalisation is applied to account for air dilution. The corresponding results can be found below:

**Table 4.1:** Emission index of  $NO$  (normalised to 15%  $O_2$ ) for the reactive flow, comparing injection temperatures of 300 K and 150 K. Results are presented in units of g  $NO$  per kg of  $H_2$  consumed.

$EI_{NO}$	Case 1: 300K	Case 2: 150 K	Difference %
Cavity Interface	0.889	0.589	-33.75%
Combustor Outlet	2.338	1.748	-25.23%

To establish a reference, modern gas engines operating on kerosene typically emit around 9–12 g of  $NO$  per kilogram of kerosene consumed [8]. In comparison, the  $NO$  values observed within the TVC and presented in the table above appear overly optimistic, particularly considering the dominance of non-premixed combustion and the presence of very high flame temperatures. However, several factors may explain these relatively low emission values. Firstly, accurately modelling  $NO$  emissions is inherently complex, and the current simulation may have underestimated  $NO$  production. Secondly, the residence time within the TVC, which is estimated at approximately 1 ms based on the volumetric flow rate and the volume of the TVC may limit significant  $NO$  formation. This is because  $NO$  production, particularly thermal  $NO$ , occurs on a longer timescale, and the short residence time likely restricts its accumulation, especially in high-temperature regions. In contrast, kerosene-fueled engines typically require longer residence times to ensure complete combustion, thereby allowing more time for  $NO$  formation. Nonetheless, it is also important to highlight that previous TVC studies using hydrogen as fuel have reported similar pollutant levels as to those obtained here [31]. Hence, providing a conclusive statement about the accuracy of these results is challenging and would require further investigation, including refined modelling and experimental validation, to confirm these findings.

Beyond the absolute values presented above, two key conclusions can be drawn when comparing the results for both injection temperatures. First, the increase in  $NO$  emissions from the cavity interface to the TVC outlet remains consistent across both cases. More specifically, the  $NO$  emission index at the outlet is approximately three times higher than at the cavity interface. Secondly, a significant reduction of about 25% in  $NO$  emissions is observed at the outlet when the hydrogen injection temperature is reduced from 300 K to 150 K. This clearly highlights a strong sensitivity of  $NO_x$  emissions to the injection temperature.

# 5

## Conclusion & Recommendations

Trapped vortex combustors in the context of RQL combustion represent an innovative solution for integrating hydrogen's challenging flame dynamics while maintaining efficiency and stability. This makes them a highly promising technology for advancing the energy transition towards a cleaner and a more sustainable aviation industry, in which pollutants are minimised. However, several challenges, including limited mixing and the establishment of a diffusion flame within the cavity, still persist, preventing the design from achieving its intended performance. Therefore this research is conducted, aimed at addressing these challenges and thus improving the RQL effectiveness by investigating hydrogen's inlet temperature as the potential solution towards this problem. To achieve this, various numerical simulations were conducted, providing the basis for the following conclusions.

Initially, 1D simulations were conducted to assess the effect of lowering hydrogen's inlet temperature on chemical reactivity. The results showed that reducing hydrogen's temperature increased the chemical time scale by approximately 15% to 35%, depending on the mixture composition. Additionally, a further 100% increase was achieved by also lowering the air inlet temperature. Consequently, the findings demonstrated that a notable reduction in reactivity can be obtained by controlling the temperature.

Next, large-eddy simulations were required to obtain more accurate and detailed results. Therefore, a full-scale TVC model was first designed, whereby the design approach was mainly guided by the framework of the Triathlon project, along with various insights and conclusions from previous studies. In addition, a numerical modelling approach was established, of which its performance was assessed through a numerical validation study. The results revealed notable similarities between both simulations, and consistent trends across the combustors. Hence, the numerical method was able to capture the key flow and flame dynamics within the TVC with sufficient accuracy. However, it is also important to note that a small level of uncertainty remained, given the limitations of the validation data.

The results of the cold flow simulations confirmed that a well-defined flow structure was established within the adopted TVC, featuring the desired dual-vortex formation. Furthermore, with respect to mixing within the cavity, the injection angle was found to play a crucial role in determining the mixing performance. Specifically, increasing the injection angle from  $30^\circ$  to  $60^\circ$  significantly enhanced mixing effectiveness. Although further improvements may be possible with larger angles, this was beyond the scope of the study. Consequently, the best achievable fuel-air mixing quality was identified for an injection angle of  $60^\circ$ , making it the most appropriate configuration for evaluating temperature effects with in the reactive flow simulations.

The results of the reactive flow simulations revealed that combustion-induced flow expansion significantly altered the cavity's flow structure. Moreover, the reactive flow was predominantly characterised by non-premixed combustion, both within the cavity and the main combustion region, with insufficient mixing also identified in the latter. Furthermore, the sensitivity analysis demonstrated that reducing the hydrogen injection temperature led to lower reactivity. However, this reduction was insufficient to

significantly mitigate or suppress non-premixed combustion, resulting in only minor improvement to the RQL effectiveness. Nevertheless, the results also indicated that regardless of the combustion mode, a notable reduction of approximately 25% in  $\text{NO}_x$  emissions could be achieved. This reduction was primarily attributed to lower flame temperatures throughout the TVC, thereby contributing to improved performance.

## 5.1. Recommendations:

Throughout this research project, several recommendations were identified to improve and enhance the numerical simulations. Additionally, based on the obtained results, various directions for future studies emerged. Therefore, a concise overview of these recommendations are provided below:

### Numerical Methodology:

- Implement more advanced models for differential diffusion in the LES solver, such as the mixture-averaged approach, to improve the accuracy of the simulation results.
- Incorporate conjugate heat transfer (CHT) or apply realistic wall heat flux boundary conditions to evaluate the impact of heat losses to the walls on the flow and flame behaviour.
- Detail the chemical mechanism, with in particular the chemical reactions including  $\text{NO}_x$  emissions, to identify the influence or sensitivity on the the emission calculations.

### Trapped Vortex Combustor Performance:

- Continue the analysis on injection angle to identify the configuration which provides the maximised mixing performance within the cold and/or reactive flow.
- Perform various analyses with enhanced injection velocities, both for the primary and secondary air injection to identify the improvements in mixing and reduction in flow spillage.
- Evaluate whether increasing the cavity dimensions enhances the formation of the vortical structures within the reactive flow as compared to the cold flow, particularly in response to the significant gas expansion.
- In order to reduce the chemical reactivity even more and improve the RQL combustion strategy, introduce water droplets into the cavity and evaluate their effects on flow behaviour and flame dynamics.
- Add more sophisticated flame-transfer structures at the inlet such as radial struts and multi-orifices plates to identify its influence on the mixing performance and combustion behaviour within the main flow region.

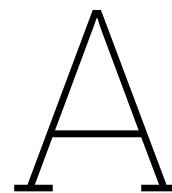
# References

- [1] International Renewable Energy Agency (IRENA). *Hydrogen Technology*. Accessed: August 22, 2024. n.d. URL: <https://www.irena.org/Energy-Transition/Technology/Hydrogen>.
- [2] R. Kortlever. *Introduction The role of Hydrogen*. PowerPoint presentation. SET3085: Hydrogen Technology, Technological University of Delft. 2024.
- [3] IEA. *The Future of Hydrogen, Paris*. Tech. rep. International Energy Agency, Jan. 2019.
- [4] R. Kortlever. *Hydrogen Compression Storage*. PowerPoint presentation. SET3085: Hydrogen Technology, Technological University of Delft. 2024.
- [5] F. De Domenico et al. *Hydrogen Combustion*. PowerPoint presentation. AE4262: Combustion for Propulsion and Power Systems, Technological University of Delft. 2023.
- [6] Stefan Kazula, Martin Staggat, and Stefanie Graaf. "Functional and Safety Challenges of Hydrogen Fuel Cell Systems for Application in Electrified Regional Aircraft". In: *Journal of Physics: Conference Series* 2526 (June 2023), p. 012063. DOI: 10.1088/1742-6596/2526/1/012063.
- [7] Ahmad Baroutaji et al. "Comprehensive investigation on hydrogen and fuel cell technology in the aviation and aerospace sectors". In: *Renewable and Sustainable Energy Reviews* 106 (2019). ISSN: 1364-0321. DOI: <https://doi.org/10.1016/j.rser.2019.02.022>. URL: <https://www.sciencedirect.com/science/article/pii/S1364032119301157>.
- [8] Miguel Ángel Sáez Ortuño et al. "Climate Assessment of Hydrogen Combustion Aircraft: Towards a Green Aviation Sector". In: *AIAA SCITECH 2023 Forum*. AIAA, 2023. URL: <https://arc.aiaa.org/doi/abs/10.2514/6.2023-2513>.
- [9] International Air Transport Association. *Aviation contrails and their climate effect, tackling uncertainties and enabling solutions*. Tech. rep. IATA, 2024.
- [10] T. Capurso et al. "NOx pathways in lean partially premixed swirling H<sub>2</sub>-air turbulent flame". In: *Combustion and Flame* 248 (2023). ISSN: 0010-2180. DOI: <https://doi.org/10.1016/j.combustflame.2022.112581>. URL: <https://www.sciencedirect.com/science/article/pii/S0010218022005892>.
- [11] Thirupathi Boningari and Panagiotis G. Smirniotis. "Impact of nitrogen oxides on the environment and human health: Mn-based materials for the NOx abatement". In: *Current Opinion in Chemical Engineering* 13 (2016), pp. 133–141. ISSN: 2211-3398. DOI: <https://doi.org/10.1016/j.coche.2016.09.004>. URL: <https://www.sciencedirect.com/science/article/pii/S2211339816300661>.
- [12] A. G. Rao. *Lecture 6: Engine Emissions and Global Warming*. PowerPoint presentation. AE4238: Aero Engine Technology, Technological University of Delft. 2021.
- [13] Vincent van and Martijn Van essen. "Fundamental limits of NO formation in fuel-rich premixed methane-air flames". PhD thesis. Rijksuniversiteit Groningen, 2007.
- [14] F. De Domenico et al. *Turbulent Combustion Modeling*. PowerPoint presentation. AE4262: Combustion for Propulsion and Power Systems, Technological University of Delft. 2023.
- [15] S. Menon. "A Numerical Investigation of Aerodynamically Trapped Vortex Combustor for Premixed Hydrogen Combustion in Gas Turbines Using Detailed Chemistry". Additional Information. MA thesis. Faculty of Aerospace Engineering: Technological University of Delft, 2019.
- [16] Denis Veynante and Luc Vervisch. "Turbulent combustion modeling". In: *Progress in Energy and Combustion Science* 28.3 (2002), pp. 193–266.
- [17] Markus Bösenhofer, C. Jordan, and Michael Harasek. "Difficulties in the characterization of gas phase combustion regimes". In: *Chemical and Process Engineering* (Mar. 2017).

- [18] Mohamed Hafid et al. "Simulating of non-premixed turbulent combustion using a presumed probability density function method". In: *Heat and Mass Transfer* 59.1 (Jan. 2023), pp. 81–93.
- [19] Lorenz Boeck. "Deflagration-to-Detonation Transition and Detonation Propagation in H<sub>2</sub>-Air Mixtures with Transverse Concentration Gradients". PhD thesis. Technische Universität München, June 2015.
- [20] A. G. Rao. *Aero Engine Combustor-2*. PowerPoint presentation. AE4238: Aero Engine Technology, Technological University of Delft. 2021.
- [21] Ying Huang and Vigor Yang. "Dynamics and stability of lean-premixed swirl-stabilized combustion". In: *Progress in Energy and Combustion Science* 35.4 (2009), pp. 293–364. ISSN: 0360-1285. DOI: <https://doi.org/10.1016/j.pecs.2009.01.002>. URL: <https://www.sciencedirect.com/science/article/pii/S0360128509000094>.
- [22] Robert W. Dibble Jürgen Warnatz Ulrich Maas. *Physical and Chemical Fundamentals, Modeling and Simulation, Experiments, Pollutant Formation*. Springer Berlin, Heidelberg, 2006.
- [23] A. G. Rao. *Practical Combustion Systems*. PowerPoint presentation. AE4262: Combustion for Propulsion and Power Systems, Technological University of Delft. 2023.
- [24] Noureddine Guellouh, Zoltán Szamosi, and Zoltán Siménfalvi. "Combustors with Low Emission Levels for Aero Gas Turbine Engines". In: *International Journal of Engineering and Management Sciences* 4 (Mar. 2019), pp. 503–514. DOI: 10.21791/IJEMS.2019.1.62..
- [25] Pavlos G. Aleiferis and Martino F. Rosati. "Controlled autoignition of hydrogen in a direct-injection optical engine". In: *Combustion and Flame* 159.7 (2012), pp. 2500–2515.
- [26] Thoralf G. Reichel, Steffen Terhaar, and Christian Oliver Paschereit. "Flashback Resistance and Fuel–Air Mixing in Lean Premixed Hydrogen Combustion". In: *Journal of Propulsion and Power* 34.3 (2018), pp. 690–701.
- [27] Harald H W Funke, K. Kusterer, and J. Keinz. "Improvement study for the dry-low-NO<sub>x</sub> hydrogen micromix combustion technology". In: *Propulsion and Power Research* 4.3 (2015), pp. 132–140.
- [28] E. Gutmark and P. de Goeij. "A review of cavity-based trapped vortex, ultra-compact, high-g, inter-turbine combustors". In: *Progress in Energy and Combustion Science* 66 (2018). Publisher: Elsevier Ltd.
- [29] K.-Y. Hsu, L. P. Goss, and W. M. Roquemore. "Characteristics of a Trapped-Vortex Combustor". In: *Journal of Propulsion and Power* 14.1 (1998). \_eprint: <https://doi.org/10.2514/2.5266>, pp. 57–65. DOI: 10.2514/2.5266. URL: <https://doi.org/10.2514/2.5266>.
- [30] Wensheng Zhao, Weijun Fan, and Rongchun Zhang. "Study on the effect of fuel injection on combustion performance and NO<sub>x</sub> emission of RQL trapped-vortex combustor". In: *Energy Reports* 9 (2023). ISSN: 2352-4847. DOI: <https://doi.org/10.1016/j.egyrs.2023.04.028>. URL: <https://www.sciencedirect.com/science/article/pii/S235248472300389X>.
- [31] Reza Sharifzadeh and Asghar Afshari. "Assessment of a hydrogen-fueled swirling trapped-vortex combustor using large-eddy simulation". In: *Fuel* 357 (2024). ISSN: 0016-2361. DOI: <https://doi.org/10.1016/j.fuel.2023.129847>. URL: <https://www.sciencedirect.com/science/article/pii/S0016236123024614>.
- [32] S. Samuelsen. "Rich Burn, Quick-Mix, Lean Burn (RQL) Combustor". In: *National Energy Technology Laboratory (NETL)* (2011).
- [33] Yuxuan Zhang et al. "Influence of incoming flow parameters on the flow field in a trapped vortex cavity with radial bluff-body". In: *Aerospace Science and Technology* 132 (2023).
- [34] Douglas Straub et al. "Assessment of Rich-Burn, Quick-Mix, Lean-Burn Trapped Vortex Combustor for Stationary Gas Turbines". In: *Journal of Engineering for Gas Turbines and Power-Transactions of The Asme - J ENG GAS TURB POWER-T ASME* 127 (2005). DOI: 10.1115/1.1789152.
- [35] Maximilian Hansinger et al. "The Eulerian Stochastic Fields Method Applied to Large Eddy Simulations of a Piloted Flame with Inhomogeneous Inlet". In: *Flow, Turbulence and Combustion* (2020). DOI: 10.1007/s10494-020-00159-5.

- [36] Vladislav Eftos. "Large Eddy Simulation of Channel Flow using Wall Functions". PhD thesis. Goteborg, Sweden: Chalmers University of Technology, 2006.
- [37] Denis Veynante and Luc Vervisch. "Turbulent combustion modeling". In: *Progress in Energy and Combustion Science* 28.3 (2002), pp. 193–266. ISSN: 0360-1285. DOI: [https://doi.org/10.1016/S0360-1285\(01\)00017-X](https://doi.org/10.1016/S0360-1285(01)00017-X).
- [38] Andrew Cook and James Riley. "A Subgrid Model for Equilibrium Chemistry in Turbulent Flows". In: *Physics of Fluids - PHYS FLUIDS* 6 (Aug. 1994), pp. 2868–2870. DOI: 10.1063/1.868111.
- [39] W. J. S. Ramaekers. "The Application of Flamelet Generated Manifolds in Modelling of Turbulent Partially-Premixed Flames". English. MA thesis. Eindhoven University of Technology, Aug. 2005.
- [40] Paola Breda et al. "Validation of an Eulerian Stochastic Fields Solver Coupled with Reaction–Diffusion Manifolds on LES of Methane/Air Non-premixed Flames". In: *Flow, Turbulence and Combustion* 107.2 (2021), pp. 441–477. ISSN: 1573-1987. DOI: 10.1007/s10494-020-00235-w. URL: <https://doi.org/10.1007/s10494-020-00235-w>.
- [41] Daniel Werner. "On the Modeling of Molecular Mixing in Turbulent Flows". PhD thesis. Zurich, Switzerland: ETH Zurich, 2008. URL: <https://www.research-collection.ethz.ch/bitstream/handle/20.500.11850/44871/eth-30503-02.pdf>.
- [42] Alexander Avdonin, Alireza Javareshkian, and Wolfgang Polifke. *Prediction of Premixed Flame Dynamics Using LES With Tabulated Chemistry and Eulerian Stochastic Fields*. June 2019. DOI: 10.1115/GT2019-90140.
- [43] Alessandro Porcarelli, Boris Kruljević, and Ivan Langella. "Suppression of NO<sub>x</sub> emissions by intensive strain in lean premixed hydrogen flamelets". In: *International Journal of Hydrogen Energy* 49 (2024), pp. 413–431. ISSN: 0360-3199. DOI: <https://doi.org/10.1016/j.ijhydene.2023.08.110>. URL: <https://www.sciencedirect.com/science/article/pii/S0360319923041125>.
- [44] Alexander A. Konnov. "Yet another kinetic mechanism for hydrogen combustion". In: *Combustion and Flame* 203 (2019), pp. 14–22. ISSN: 0010-2180. DOI: <https://doi.org/10.1016/j.combustflame.2019.01.032>.
- [45] Marcus Ó Conaire et al. "A Comprehensive Modeling Study of Hydrogen Oxidation". In: *International Journal of Chemical Kinetics* 36.10 (2004), pp. 603–622. DOI: 10.1002/kin.20036.
- [46] United Turbine. *PT6 Descriptive course and Guide to troubleshooting*. Last accessed 25 July 2014. 2017. URL: <https://www.peter-ftp.co.uk/aviation/misc-euroga/PT6%20Training%20Manual.pdf>.
- [47] Saurav Tiwari, Michael J. Pekris, and John J. Doherty. "A review of liquid hydrogen aircraft and propulsion technologies". In: *International Journal of Hydrogen Energy* 57 (2024), pp. 1174–1196. ISSN: 0360-3199. DOI: <https://doi.org/10.1016/j.ijhydene.2023.12.263>.
- [48] S. Krishna and R. V. Ravikrishna. "Optical diagnostics of fuel–air mixing and vortex formation in a cavity combustor". In: *Experimental Thermal and Fluid Science* 61 (2015). ISSN: 0894-1777. DOI: <https://doi.org/10.1016/j.expthermflusci.2014.10.012>. URL: <https://www.sciencedirect.com/science/article/pii/S0894177714002544>.
- [49] Cindy Merlin, Pascale Domingo, and Luc Vervisch. "Large Eddy Simulation of turbulent flames in a Trapped Vortex Combustor (TVC) – A flamelet presumed-pdf closure preserving laminar flame speed". In: *Comptes Rendus Mécanique* 340.11 (2012). ISSN: 1631-0721. DOI: <https://doi.org/10.1016/j.crme.2012.10.039>. URL: <https://www.sciencedirect.com/science/article/pii/S1631072112002033>.
- [50] A.S. Doost et al. "Residence time calculations for complex swirling flow in a combustion chamber using large-eddy simulations". In: *Chemical Engineering Science* 156 (2016), pp. 97–114. ISSN: 0009-2509. DOI: <https://doi.org/10.1016/j.ces.2016.09.001>.
- [51] Stephen B. Pope. *Turbulent Flows*. Cambridge, UK: Cambridge University Press, 2000. ISBN: 978-0521591256. DOI: 10.1017/CB09780511840531. URL: <https://www.cambridge.org/core/books/turbulent-flows/13C964F3EBD013401BC9911585EBA3A2>.
- [52] T. Capurso et al. "NO<sub>x</sub> pathways in lean partially premixed swirling H<sub>2</sub>/air turbulent flame". In: *Combustion and Flame* 248 (2023), p. 112581. ISSN: 0010-2180. DOI: <https://doi.org/10.1016/j.combustflame.2022.112581>.

- [53] Fangqing Liu. "A Thorough Description of How Wall Functions Are Implemented in OpenFOAM". In: *Proceedings of CFD with OpenSource Software*. Ed. by Håkan Nilsson. 2016.
- [54] A. Samim Doost et al. "Residence time calculations for complex swirling flow in a combustion chamber using large-eddy simulations". In: *Chemical Engineering Science* 156 (Sept. 2016). DOI: 10.1016/j.ces.2016.09.001.
- [55] Douglas Straub et al. "Assessment of Rich-Burn, Quick-Mix, Lean-Burn Trapped Vortex Combustor for Stationary Gas Turbines". In: *Journal of Engineering for Gas Turbines and Power-Transactions of The Asme - J ENG GAS TURB POWER-T ASME* 127 (Jan. 2005). DOI: 10.1115/1.1789152.
- [56] H. Yamashita, M. Shimada, and T. Takeno. "A numerical study on flame stability at the transition point of jet diffusion flames". In: *Symposium (International) on Combustion* 26.1 (1996), pp. 27–34. ISSN: 0082-0784. DOI: [https://doi.org/10.1016/S0082-0784\(96\)80196-2](https://doi.org/10.1016/S0082-0784(96)80196-2).



# ESF\_fBilgerFoam Solver

This appendix provides an overview of the modifications that were made to the *ESF\_fBilgerFoam* solver to implement differential diffusion based on the Lewis analogy. Thereby, section A.1, outlines the computational method and approach adopted, while section A.2 presents the specific code modifications.

## A.1. Description of the Computational Method

An analysis of the thermophysical libraries linked to the original solver revealed that the laminar diffusion coefficient is initialised and stored as a volScalarField, named **Df\_** within **BasicThermo.H**. Thereby, at each timestep, this field is accessed and recalculated by the solver based on the updated thermal diffusivity, while assuming a fixed Lewis number equal to 1.0

To overcome this limitation in a straightforward, yet effective manner, three key modifications were made to the main solver:

1. **Thermo file:** A location was required in which the Lewis number would be specified for the given species. To ensure flexibility when modifying the chemical mechanism and species involved, the Lewis number was incorporated into the transportDict within the .thermo file of the simulation.
2. **Createfields.H:** The solver needed the ability to access and store the list of Lewis numbers within its working environment. This was achieved by modifying createFields.H, where the solver reads the necessary system and constant files and initialises the various models.
3. **SFEqn.H:** The diffusion coefficient had to be computed for all species, and subsequently applied correctly within the species transport equations. To accommodate this, the existing computational method was replaced with the updated formulation in the SFEqn.H file.

Finally, the solver was recompiled to integrate the modifications and verify that all changes had been correctly implemented without errors.

## A.2. Code Modifications

### Thermo File:

```
1 OH
2 {
3   transport
4   {
5     As      1.67212e-06;
6     Ts      170.672;
7     Le      0.876;
8   }
}
```

**Createfields.H:**

```

1 ifstream thermoFileStream
2 (
3     fileName(thermo.lookup("foamChemistryThermoFile")).expand()
4 );
5
6 // Create an IOdictionary for the contents read from the file stream
7 dictionary thermoDataDict(thermoFileStream);
8
9 Foam::HashTable<scalar> lewisNumbers;
10
11 forAll(Y, specieIndex)
12 {
13     const word& speciesName = Y[specieIndex].name(); // Get species name
14
15     // Access the 'transport' sub-dictionary for the current species
16     const dictionary& transportDict = thermoDataDict.subDict(specieName).subDict("transport");
17
18     // Check if the 'Le' entry exists in the 'transport' sub-dictionary
19     if (transportDict.found("Le"))
20     {
21         scalar Le = Foam::readScalar(transportDict.lookup("Le"));
22         lewisNumbers.insert(specieName, Le);
23         Info << "Species:" << speciesName << ",Le=" << Le << nl;
24     }
25     else
26     {
27         // Use default Lewis number and print an Info statement
28         Info << "No-Lewis-number-specified-for-Species:" << specieName << ",Le=1.0" << nl;
29         lewisNumbers.insert(specieName, 1.0);
30     }
31 }

```

**SFEqn.H:**

```

1 forAll(Y, j)
2 {
3     if (Y[j].name() != inertSpecie)
4     {
5         volScalarField& scalarFieldi = scalarFields[j][i];
6         volScalarField& lRRYSpeciesjFieldi = lRRY[j][i];
7
8         // Determine Effective species diffusion
9         scalar Le = lewisNumbers[Y[j].name()];
10
11         volScalarField alphaField = thermo.alpha();
12         volScalarField DftField = turbulence->Dft();
13
14         volScalarField DfEffField = ((1.0 / Le) * (1.0 / rho) * alphaField) +
15             DftField;
16
17         fvScalarMatrix scalarFieldiEqn
18         (
19             fvm::ddt(rho, scalarFieldi)
20             + mvConvection->fvmDiv(phi, scalarFieldi)
21             - fvm::laplacian('DfEffField*rho', scalarFieldi)
22             ==
23             reaction->RESF(scalarFieldi)
24             + lRRYSpeciesjFieldi
25             + fvOptions(rho, scalarFieldi)
26         );
27         ...
28     }

```

# B

## Setup of the Validation Study

In this appendix, an overview of the boundary conditions and the numerical setup, specified for the large-Eddy simulation of the validation model is presented. In section B.1, the boundary conditions are specified. Next, in section B.2, the setting of the numerical setup are provided.

### B.1. Boundary Conditions

**Table B.1:** Boundary conditions for the mass fractions involved in the validation model simulations

<b>Boundary Patch:</b>	<b><math>Y_{H_2}</math></b>	<b><math>Y_{N_2}</math></b>	<b><math>Y_{O_2}</math></b>
Inlet	0.01446	0.75599	0.22955
Outlet	zeroGradient	zeroGradient	zeroGradient
Fuel/Air	0.04216	0.73474	0.22310
Secondary Air	0.0	0.767	0.233
Wall	zeroGradient	zeroGradient	zeroGradient

**Table B.2:** Boundary conditions for velocity, pressure, and temperature involved in the validation model simulations

<b>Boundary Patch:</b>	<b>Velocity</b>	<b>Pressure</b>	<b>Temperature</b>
Inlet	150 m/s	zeroGradient	850 K
Outlet	zeroGradient	waveTransmissive, 1 atm	zeroGradient
Fuel/air	3 m/s	zeroGradient	300 K
Secondary air	16 m/s	zeroGradient	300 K
Wall	0 m/s	zeroGradient	zeroGradient

## B.2. Numerical Setup

**Table B.3:** Summary of the numerical setup for the validation model simulations.

<b>Numerical Schemes/ Setup:</b>	<b>Cold Flow</b>	<b>Reactive Flow</b>
Temporal Scheme	Implicit Euler, 1st-Order	Implicit Euler, 1st-Order
Momentum Divergence	2nd-Order, limited	2nd-Order, limited
Species Divergence	2nd-Order, limited	2nd-Order, limited
Enthalpy Divergence	2nd-Order, limited	2nd-Order, limited
Chemistry Integration	-	Implicit Euler, 1st-Order
Pressure-Velocity Coupling	PIMPLE	PIMPLE
Convergence Rate	$10^{-10}$	$10^{-10}$